Die approbierte Originalversion dieser Dissertation ist an der Hauptbibliothek der Technischen Universität Wien aufgestellt (http://www.ub.tuwien.ac.at).

The approved original version of this thesis is available at the main library of the Vienna University of Technology (http://www.ub.tuwien.ac.at/englweb/).

Dissertation

Electronic and magnetic properties of nanostructures

ausgeführt zum Zwecke der Erlangung des akademischen Grades eines
Doktors der technischen Wissenschaften
unter der Leitung von

Univ.-Prof. Dr. Peter Weinberger
Institutsnummer: E 134
Institut für Allgemeine Physik

eingereicht an der Technischen Universität Wien
Technisch-Naturwissenschaftliche Fakultät

von

Bence Lazarovits
Matrikelnummer: 0027103
A-1040 Wien, Schlüsselgasse 11/46

Wien, am 25. Mai. 2003

Bence Lazarovits

Kurzfassung

In der vorliegenden Dissertation werden die magnetische Momente und die magnetokristalline Anisotropie von magnetischen Nanostrukturen auf metallischen Filmen diskutiert. Ich habe Adatome und kleine Nanostrukturen von Fe, Co und Ni auf einer Ag(OOl) Oberfläche, von endlichen Co Ketten auf einer Pt(lll) Obefläche, und von endlichen Fe Ketten auf Cu(OOl) und Cu(lll) Oberflächen und in den entsprechenden Substraten in Betracht gezogen. Die verwendete theoretische Methode ist die "Embedding" Technik innerhalb der voll-relativistischen Korringa-Kohn-Rostoker Methode. Die magnetische Anisotropie, das Hauptziel in der vorliegenden Dissertation, wird mit Hilfe des sogenannten "Force Theorems" berechnet.

Abstract

In the present work systematic studies of the magnetic moments and the magneto-crystalline anisotropy of magnetic clusters on metallic surfaces are presented. In particular, I investigated adatoms and small clusters of Fe. Co and Ni on Ag(OOl) surface, finite Co chains on Pt(lll) surface and finite Fe chains at Cu(OOl) and Cu(111) surfaces as well as embedded into a perfect bulk host. The calculations are performed fully relativistically using the embedding technique within the Korringa–Kohn–Rostoker method. The magnetic anisotropy energies the main goal of the present study are calculated by means of the magnetic force theorem.

Contents

Kurzfassung 2

Abstract 3

Contents 4

1 Introduction 7

I Theoretical method 12

2 Density Functional Theory 13

2.1 The Hohenberg-Kohn Theorems . . . 13

2.2 The Kohn-Sham Equations . . . 15

2.3 The Kohn-Sham-Dirac Equation . . . 18

3 The Multiple Scattering Theory 20

3.1 The Formal Scattering Theory . . . 20

3.2 Calculation of Observables . . . 22

3.3 The Dirac Hamiltonian . . . 24

3.4 The Single-Site Scattering . . . 26

3.5 Transformation of the Single-site t-matrix . . . 28

3.6 Multiple Scattering Theory . . . 30

4 Generalized KKR 35

5 The Screened KKR Method for Layered Systems 38

5.1 Layered Systems . . . 38

5.2 The Surface Brillouin Zone Integration . . . 45

6 The Embedding Technique 47
6.1 The τ-matrix of a Single Embedded Atom . . . 47
6.2 The r-matrix for N Embedded Atoms . . . 49
6.3 Self-consistent Calculation for a Cluster . . . 52
6.4 Approximations of the Inversion of the τ-matrix . . . 53

7 Electrostatic potential for an embedded cluster 55
7.1 Basic Definitions . . . 55
7.2 Electrostatic Potential of a Lattice . . . 56
7.3 Electrostatic Potential in a Layered System . . . 58
7.4 Electrostatic Potential in a Cluster . . . 61

8 The Magnetic Anisotropy Energy 64
8.1 The Magnetic Force Theorem . . . 65

II Results 70

9 Fe, Co and Ni adclusters on Ag(OOl) 71
9.1 Introduction . . . 71
9.2 Results . . . 73
9.2.1 Spin and Orbital Moments . . . 73
9.2.2 Magnetic Anisotropy . . . 78
9.2.3 Magnetic Interaction between Adatoms . . . 80

10 Finite Co chains on Pt(lll) 88
10.1 Introduction . . . 88
10.1.1 Growth of Atomic-Scale Structures on Pt . . . 89
10.1.2 Aspects of Magnetism . . . 90
10.2 Results . . . 91
10.2.1 Spin and Orbital Moments . . . 91
10.2.2 Magnetic Anisotropy . . . 94

11 Finite Fe chains at fcc Cu(OOl) and Cu(lll) surfaces 102
11.1 Introduction . . . 102
11.1.1 Aspects of Growth . . . 102
11.1.2 Aspects of Magnetism . . . 103
11.2 Results . . . 104
11.2.1 Spin and Orbital Moments . . . 104
11.2.2 Magnetic Anisotropy . . . 110

12 Conclusions 125

A The Single-site Scattering with Spin Polarization 128
A.1 Scaling of the Spin-orbit Coupling . . . 130

B The Godfrin method 132

C Rotational Properties of the Structure Constants 133

D Computational details 136
D.1 Contour integration . . . 136
D.2 BZ integration . . . 136
D.3 Multipole expansion . . . 137

References 138

Publications 147

Acknowledgments 149

Curriculum Vitae 150

Chapter 1

Introduction

The fast development of manufacturing and observation techniques made available a large number of different geometrical arrangements of magnetic impurities on metallic surfaces like dots, wires, stripes or corrals. Due to their sensitivity on the local environment, the magnetic properties of transition metal structures can be greatly modulated, exploring a wide spectrum of magnetic phenomena, e.g., increased spin and orbital magnetization, strong magnetic anisotropies, non-collinear magnetism, as well as a temperature and time dependence of the magnetization. These low-dimensional structures are intensively studied both experimentally [Beckmann and Bergmann, 1996; Ohresser et al., 2001; Lau et al., 2002a,b; Eimers et al., 1994; Crommie et al., 1995; Shen et al., 1997b; Hauschild et al., 1998; York and Leibsle, 2001; Gambardella et al., 2000a,b, 2002) and theoretically [Wildberger et al., 1995; Stepanyuk et al., 1996b; Družinić and Hübner, 1997; Dorantes-Dävila and Pastor, 1998; Robles et al., 2000; Bellini et al., 2001; Spišák and Hafner, 2002; Eisenbach et al., 2002; Komelj et al., 2002] mainly because of their possible application as magnetic nano-devices and high-density magnetic recording media. Nowadays, nanolithography based fabrication technologies [Chou et al., 1996] and the scanning tunneling microscope [Crommie et al., 1995] give the opportunity for engineering artifical nanostructures, e.g., high density arrays or quantum corrals.

Beckmann and Bergmann studied *3d* impurities on a Au surface and found that V, Cr, Mn, Fe, and Co adatoms posses a magnetic moment while Sc and Ni were reported to be nonmagnetic [Beckmann and Bergmann, 1996]. Recently, by using x-ray magnetic circular dichroism (XMCD) the magnetic properties of small Fe clusters on a reconstructed Au(lll) surface [Ohresser et al., 2001] and on a Ni|Cu(100)

surface [Lau et al., 2002a,b| were investigated. In these experiments it was found that the orbital moment changes dramatically with the size of the clusters while the spin moment remains nearly constant. The attention to the unique features of 1D magnetic systems was drawn by experiments on self-organized Fe nanostripes on a W(110) surface [Elmers et al., 1994; Hauschild et al., 1998]. For Fe stripes on Cu(lll) Shen *et al.* [Shen et al., 1997b] observed an easy axis perpendicular to the surface and found that the magnetization was temperature- and time-dependent. For the same system Boeglin *et al.* [Boeglin et al., 2002] reported an in-plane magneto-crystalline anisotropy energy favoring an orientation perpendicular to the chain. Recently, York and Leibsle [York and Leibsle, 2001| demonstrated that at definite growth conditions, Co can form self-organized arrays of nanowires on a Cu(110) surface. Monoatomic rows of Ag, Cu and Co can be grown on a periodically stepped surface of Pt as step decoration [Gambardella et al., 2000a,b]. Co wires on Pt exhibit exorbitant magnetic properties like unusually large orbital moments and strong magnetic anisotropies if compared to a monolayer or the bulk case [Gambardella et al., 2002). In these experiments the estimated average length of a continuous Co chain was 80 atoms; at a temperature of 45 K the ferromagnetic order was, however, found to extend over about 15 Co atoms only.

Concomitantly with these experiments, quite some theoretical effort was devoted to study magnetism in zero- and one-dimensional arrangements of atoms deposited on surfaces. Effects of interatomic electronic interactions on the formation of magnetic moments were discussed in details for finite [Wildberger et al., 1995] and infinite [Bellini et al., 2001] 4*d* rows on vicinal Ag surfaces, leaving however, questions about the oscillatory behavior of the moments open. The structure and magnetism of monoatomic Fe wires grown on different stepped Cu($11n$) (n = 3 — 11) surfaces were investigated by Spišák and Hafner [Spišák and Hafner, 2002]. Eisenbach *et al.* [Eisenbach et al., 2002| demonstrated by using the real space Korringa–Kohn–Rostoker (KKR) method that changing the crystallographic orientation of infinite Fe wires embedded into Cu bulk results in a change of the easy axis. Because of the lack of translational symmetry tight-binding (TB) methods have been an efficient tool to study larger clusters. A great advantage of these methods seems to be that they can easily be combined with molecular dynamics calculations enabling thus investigations of relaxation effects which proved to be important in determining the

magnetic moments [Piveteau et al., 1996; Rodriguez-López et al., 1999; Guirado-López et al., 2000] and the magnetic anisotropy energy [Guirado-López, 2001] of transition metal clusters. The inclusion of structural relaxations into the KKR Green's function method is much more difficult, however, the so-called quasi-ab initio molecular-dynamics method can be a solution for this problem [Izquierdo et al., 2001]. By using a TB Hubbard Hamiltonian in the unrestricted Hartree-Fock approximation, Pastor and co-workers revealed the size and structural dependence of magnetic properties of free Cr_n, Fe_n and Ni_n ($n < 15$) clusters [Pastor et al., 1989], and also the exchange interaction and local environments effects in freestanding Fe clusters [Dorantes-Dävila et al., 1992]. By including a spin-orbit coupling term into the Hamiltonian, they also investigated various effects on the magnetic anisotropy energy of small unsupported Fe clusters [Pastor et al., 1995], of selected Co clusters on Pd(lll) [Felix-Medina et al., 2000] and, recently, finite-length Co wires on Pd(llO) [Felix-Medina et al., 2002]. Finite temperature magnetism of small clusters, remarkably different from that of the bulk systems, has also been studied in terms of a similar approach by taking into account both electronic and structural excitations [López-Urias et al., 2000]. Druzinic and Hübner calculated the magnetic anisotropy energy for freestanding Fe wires and rings [Družinić and Hübner, 1997]. Dorantes-Dävila and Pastor [Dorantes-Dävila and Pastor, 1998] revealed that oscillations of the magnetic anisotropy energy corresponding to a preferred orientation along short Fe and Co wires are stabilized over a length of about 20 atoms. They found that when deposited on Pd(110) the magnetization of the Co wires turned to an out-of-plane direction. Very recently Komelj *et. al.* [Komelj et al., 2002] established a clear trend for an enhancement of the spin- and orbital magnetism of Co as bulk (3D), monolayer (2D) and wire (1D), respectively.

Starting from the mid-nineties our group carried out systematic investigations of magnetic properties, in particular, of the magnetic anisotropy energy of transition metal multilayer systems by using the fully relativistic spin-polarized screened Korringa-Kohn-Rostoker (SKKR) method [Szunyogh et al., 1994b; Zeller et al., 1995]. The anomalous perpendicular magnetic anisotropy [Üjfalussy et al., 1996a,b], the magnetic properties of surface alloys [Szunyogh et al., 1997], the magnetic reorientation due to the lattice relaxations [Uiberacker et al., 1999], the Bloch walls in ferromagnetic systems [Schwitalla et al., 2001] and the effects of the chemical order-

ing on the magnetic anisotropy [Szunyogh et al., 2001] were systematically studied. A summary of the calculations for perpendicular anisotropy in magnetic multilayers can be found in Ref. [Weinberger and Szunyogh, 2000].

The purpose of the present work is to extend these studies in order to perform realistic investigations for magnetic clusters on metallic surfaces by including self-consistent effects (electronic relaxations) of the host atoms. For this very reason I extended the SKKR program package making use of the real-space embedding technique based on the KKR method in the local spin-density approximation and also treated the Poisson equation with appropriate boundary conditions. It should be noted that a similar embedding technique has been applied to transition metal adatoms and small clusters embedded into a bulk host [Podloucky et al., 1980; Zeller et al., 1980] or deposited on surfaces [Lang et al., 1994; Wildberger et al., 1995; Stepanyuk et al., 1996a,b, 1997a,b]. By using the SKKR method describing the semi-infinite host, the electronic structure of the surfaces supporting the magnetic clusters can be taken into account in a much more accurate way than calculations using slab or supercell geometry. The fully relativistic description of the scattering mechanism I used enables one to calculate the magneto-crystalline anisotropy in a non-perturbative way. The scaling technique of the spin-orbit coupling [Ebert et al., 1996] can also be used serving as a qualitative explanation for the reorientation of the easy magnetization axis in the framework of the perturbation theory. Focusing on the dependence of the magnetic moments on the local environment one can study the effects of the impurity-impurity and the impurity-host interactions. The magnetic interactions between adatoms or small islands which is of particular importance from a technological point of view can also be addressed. Calculating the atom-like resolution of the spin- and orbital moments and of the magneto-crystalline anisotropy helps to understand the evolution of the magnetic properties when the clusters size is increased. Investigating the spatial distribution of the magnetic moments can serve as a reasonable explanation for the experimental results which in several cases showed a non-monotonous magnetic behavior for clusters with increasing size. Studying clusters of different size and shape the crossover between systems with different dimensions (OD $\longrightarrow$ 1D or OD $\longrightarrow$ 2D) can be described.

The thesis which aims to give a comprehensive summary of the research I've done during the past three years is organized as follows: in the first part the theoretical

methods used in here, namely, the density functional theory (chapter 2), the Multiple Scattering Theory (chapter 3), the generalized KKR method (chapter 4), the embedding technique of the KKR method (chapter 6), the solution of the Poisson equation for surfaces and embedded clusters (chapter 7) and the determination of the magnetic anisotropy energy (chapter 8) are described in detail. In the second part the results of the dissertation are presented. In chapter 9 the magnetic properties of small Fe, Co and Ni adclusters on Ag(OOl) are discussed. It is concluded there that according to the experiments [Ohresser et al., 2001; Lau et al., 2002b] the orbital moments are more sensitive to the cluster size (the local environment) than the spin moments. In chapter 10 I discuss the magnetic behavior of finite Co_n (n = 1 — 10) chains deposited on Pt(lll) surface along the $(1\bar{1}0)$ direction. For these wires the orbital moments and the magnetic anisotropy energies show a distinctly different character as compared to the corresponding overlayer. For finite Fe_n (n — 1 — 9) chains at fcc Cu(OOl) and Cu(lll) surfaces a strong dependence of the magnetic properties of the Fe chains on the distance from the surface was also observed as is presented in chapter 11. In chapter 12 I summarize the results and outline some possible directions of research for the future. In the Appendix some important theoretical details are described in a larger extent.

Part I

Theoretical method

Chapter 2

Density Functional Theory

Studying ground (and excited) state properties of a solid is a complex problem that involves a system of interacting electrons. The exact treatment of an N-electron system to determine the corresponding wave-function $\Psi(\mathbf{r}_1, \mathbf{r}_2, \ldots, \mathbf{r}_N)$ is impossible due to the high dimensionality of the problem. Instead of this, Hohenberg and Kohn proposed a method [Hohenberg and Kohn, 1964] in which the *one-electron density* plays a central role eliminating thus the degrees of freedom related to the large number of electrons. As was shown by Kohn and Sham [Kohn and Sham, 1965] using the fact that the energy is a unique functional of the ground-state charge-density that a variational principle leads to an effective one-electron Schrödinger equation. These self-consistent equations, the *Kohn-Sham equations*, are analogous to the Hartree-Fock equations. Restricting the discussions to the most important points, in the following sections a short description of both the non-relativistic and the relativistic density functional theory will be given.

2.1 The Hohenberg-Kohn Theorems

Within the Born-Oppenheimer approximation, for a fixed number, N, of electrons, the Hamiltonian can be written as the sum of the kinetic energy, $\hat{\mathrm{T}}$, the external potential, $\hat{V}$, which contains, e.g., the electrostatic interactions between the electrons and the nuclei in a solid, as well as the Coulomb repulsion of the electrons, $\hat{W}$,

$$\hat{H} = \hat{T} + \hat{V} + \hat{W} = -\sum_{i=1}^{N} \nabla_i^2 + \sum_{i=1}^{N} v(\mathbf{r}_i) + \frac{1}{2} \sum_{i \neq j}^{N} \qquad (2.1)$$

where Rydberg units ($\hbar = 1, m_e = 1/2, e^2 = 1$) are used. If, in coordinate representation, an antisymmetric N-electron state is labeled by $\Psi(\mathbf{r}_1, \mathbf{r}_2, \ldots, \mathbf{r}_N)$, the corresponding density is uniquely defined as

$$n(\mathbf{r}) \equiv \int d^3r_2 d^3r_3 \ldots d^3r_N \left(\Psi^\dagger(\mathbf{r}, \mathbf{r}_2, \mathbf{r}_3, \ldots, \mathbf{r}_N)\Psi(\mathbf{r}, \mathbf{r}_2, \mathbf{r}_3, \ldots, \mathbf{r}_N)\right) \quad . \tag{2.2}$$

Fixing the form of the interaction operator, $\hat{W}$, the Hamiltonian can be regarded as a function of v, $\hat{H} = \hat{H}[v]$. In the *density functional theory* (DFT) one looks for the ground-state properties of an interacting system. The lowest expectation value of the Hamiltonian is defined by

$$E_0[v] = \inf_{\Psi} \langle \Psi | \hat{H}[v] | \Psi \rangle \quad , \tag{2.3}$$

where the $|\Psi\rangle$ are N-electron states with finite kinetic energy. Two potentials, $v_1(\mathbf{r})$ and $v_2(\mathbf{r})$, are physically different if $v_1(\mathbf{r}) - v_2(\mathbf{r}) \neq$ *constant,* since otherwise the corresponding ground-states are the same. Let $|\Psi_0[v]\rangle$ denote the ground-state of a Hamiltonian with $v(\mathbf{r})$ then

$$\hat{H}[v]|\Psi_0[v]\rangle = E_0[v]|\Psi_0[v]\rangle \quad . \tag{2.4}$$

The *Hohenberg-Kohn Theorem* [Hohenberg and Kohn, 1964] states that $v(\mathbf{r})$ is a unique function of the ground-state density $n_0(\mathbf{r})$. In other words, for a given $n(\mathbf{r})$ there is only one $v(\mathbf{r})$ for which $n(\mathbf{r})$ is the ground-state density. This theorem is valid only for so-called v-representable densities, which are ground-state densities of systems with a real potential, $v(\mathbf{r})$. Using this theorem, any dependence of ground-state properties on the potential can be transformed into a functional dependence of the ground-state density.

One can, therefore, define the *Hohenberg-Kohn density functional,* $F_{HK}[n]$, as the functional Legendre transformation of the ground-state energy in Eq. (2.3),

$$F_{HK}[n] = E_0[v[n]] - \int d^3r v[n(\mathbf{r})]n(\mathbf{r}) \quad , \tag{2.5}$$

where $n(\mathbf{r})$ is a v-representable density. Using the Hohenberg-Kohn functional, the ground-state energy can be expressed as

$$E_0[v] = \min_n \left\{ F_{HK}[n] + \int d^3r n(\mathbf{r})v(\mathbf{r}) \right\} \tag{2.6}$$

which, together with the Hohenberg-Kohn theorem, implies that instead of the external potential, the ground-state energy can be written as a functional of the ground-state density. The problem with this functional is that neither the explicit form of $F_{HK}[n]$ nor the class of v-representable densities are known.

2.2 The Kohn-Sham Equations

The basic idea of the Kohn-Sham (KS) formulation [Kohn and Sham, 1965] of density functional theory is that the ground-state density of an interacting system can be identified as the ground-state density of a non-interacting system with an effective one-particle potential, V^s(r). If one can find this potential only a one-particle problem has to be solved.

In the KS theory the ground-state of a fermion system is taken to be a Slater determinant of the lowest N one-particle solutions, $\phi_i(\mathbf{r})$, of the Schrödinger equation with the total potential, $v^s(\mathbf{r})$,

$$\Psi_0^s(\mathbf{r}_1, \mathbf{r}_1, \ldots, \mathbf{r}_N) = \frac{1}{\sqrt{N!}} \det\{\phi_i(\mathbf{r}_k)\} \quad . \tag{2.7}$$

The corresponding density and the kinetic energy of this determinantal state can be written as

$$n^s(\mathbf{r}) = \sum_{i=1}^{N} \phi_i^*(\mathbf{r})\phi_i(\mathbf{r}) \quad , \tag{2.8}$$

and

$$T^s = -\sum_{i=1}^{N} \langle \phi_i | \nabla^2 | \phi_i \rangle \quad , \tag{2.9}$$

respectively.

The Hohenberg-Kohn functional of a non-interacting system ($w(\mathbf{r}_i - \mathbf{r}_j) = 0$, $\forall i, j$) is just the kinetic energy in the ground-state which is, consequently, a functional of the ground-state density

$$T^s[n] = E_0^s[v^s[n]] - \int d^3r v^s[n(\mathbf{r})]n(\mathbf{r}) \quad . \tag{2.10}$$

Clearly, because of Eq. (2.8), the variation of any functional of n with respect to ϕ_i^* can be written according to

$$\frac{\delta}{\delta\phi_i^*(\mathbf{r})} = \int d^3r' \frac{\delta n(\mathbf{r}')}{\delta\phi_i^*(\mathbf{r})} \frac{\delta}{\delta n(\mathbf{r}')} = \phi_i(\mathbf{r}) \frac{\delta}{\delta n(\mathbf{r})} \quad . \tag{2.11}$$

Therefore, the variation of Eq. (2.9) with respect to e.g., ϕ_i^* yields

$$-\nabla^2\phi_i(\mathbf{r}) = \frac{\delta T^s[n]}{\delta\phi_i^*(\mathbf{r})} = \frac{\delta T^s[n]}{\delta n(\mathbf{r})}\phi_i(\mathbf{r}) \tag{2.12}$$

From the variation of (2.6) in the non-interacting case, that is, F_{HK} replaced by T^s, with respect to ϕ_i^* one then obtains

$$\frac{\delta}{\delta n(\mathbf{r})}\left[T^s[n] + \int d\mathbf{r}'' n(\mathbf{r}'')v(\mathbf{r}'') - \epsilon_i \left(\int d\mathbf{r}'' n(\mathbf{r}'') - N\right)\right]\phi_i(\mathbf{r}) =$$
$$\left(-\nabla^2 + v(\mathbf{r}) - \epsilon_i\right)\phi_i(\mathbf{r}) = 0 \tag{2.13}$$

where the Lagrange multiplier, ε_i has been introduced to account for a fixed number of particles, N. Multiplying this equation by ϕ_i^* from the left and integrating over r, and, summing over the lowest N eigenvalues including degeneracies, one obtains the ground-state energy of the non-interacting system,

$$E_0^s[v] = \sum_i^N \varepsilon_i \quad . \tag{2-14}$$

In the interacting case ($w \neq 0$) the Hohenberg-Kohn functional can be decomposed as

$$F_{HK}[n] = T^s[n] + E_H[n] + E_{xc}[n] \quad , \tag{2.15}$$

with the Hartree energy,

$$E_H[n] \equiv \frac{1}{2}\int d\mathbf{r}\int d\mathbf{r}' \frac{n(\mathbf{r})n(\mathbf{r}')}{|\mathbf{r}-\mathbf{r}'|} \quad , \tag{2.16}$$

and the *exchange-correlation energy*, E_{xc}, defined by

$$E_{xc}[n] = F_{HK}[n] - T^s[n] - E_H[n] \quad . \tag{2.17}$$

Obviously, $E_{xc}[n]$ is a functional of $n(\mathbf{r})$ since all the terms on the right hand side of Eq. (2.17) are functionals of the density, too.

Inserting Eq. (2.15) into (2.6) and, similar to the non-interacting case, taking a variation with respect to ϕ_i^*, the *Kohn-Sham equations* take the form,

$$\left(-\nabla^2 + v_{ext}(\mathbf{r}) + v_H(\mathbf{r}) + v_{xc}(\mathbf{r})\right)\phi_i(\mathbf{r}) = \varepsilon_i\phi_i(\mathbf{r}) \quad , \tag{2.18}$$

where the Hartree potential is given by

$$v_H(\mathbf{r}) = \frac{\delta E_H[n]}{\delta n(\mathbf{r})} = \int d\mathbf{r}' \frac{n(\mathbf{r}')}{|\mathbf{r}-\mathbf{r}'|}, \tag{2.19}$$

and the *exchange-correlation potential* is defined as

$$v_{xc}(\mathbf{r}) \equiv \frac{\delta E_{xc}[n]}{\delta n(\mathbf{r})} \quad . \tag{2.20}$$

The exact form of E_{xc} is unknown, therefore one has to use approximations. The most common approximations are taken from the uniform electron gas problem. In the so-called *local density approximation* (LDA), $E_{xc}[n]$ can be written as

$$E_{xc}[n] \approx \int d\mathbf{r}\varepsilon_{xc}(n(\mathbf{r}))n(\mathbf{r}) \quad , \tag{2.21}$$

where $\varepsilon_{xc}[n(\mathbf{r})]$ is the density of the exchange correlation energy at position r of a uniform electron gas of density $n(\mathbf{r})$. This approximation is exact only for uniform densities but it works surprisingly well also for ground-state properties of molecules and solids. Many properties of the exchange-correlation potential of the uniform electron gas are known to high precision from different theoretical approaches as well as computer simulations. One of the mostly used approximation is the fit of Gunnarson and Lundqvist [Gunnarsson and Lundqvist, 1976]. The exchange correlation potential is given within the LDA by

$$v_{xc}(\mathbf{r}) \equiv \varepsilon_{xc}[n(\mathbf{r})] + \frac{d\varepsilon_{xc}[n(\mathbf{r})]}{dn(\mathbf{r})}n(\mathbf{r}) \quad . \tag{2.22}$$

With an assumption on the form of $v_{xc}[n]$ (or ε_{xc}), the KS equation has to be solved, then from the wave functions $n(\mathbf{r})$, and subsequently, $v_H(\mathbf{r})$ and $v_{xc}(\mathbf{r})$ can be recalculated. Repeating these two steps successively, one obtains a self-consistent solution of the ground-state of the system.

2.3 The Kohn-Sham-Dirac Equation

In order to treat magnetic systems in a non-perturbative way, one needs a relativistic generalization of the DFT, that takes into account spin-polarization, spin-orbit coupling and other relativistic effects on the same footing. In the presence of a magnetic field, the Dirac Hamiltonian reads

$$\hat{H} = -ic\vec{\alpha}\nabla + \beta mc^2 - ec\beta\gamma^{\mu}A_{\mu} \quad , \tag{2.23}$$

where A_{μ} ($\mu = 0, 1, 2, 3$) is the vector potential, $\vec{\alpha}$, ß, γ^{μ} are the standard Dirac matrices and *c* is the light velocity. It is important to mention that when establishing a relativistic density functional theory in a variational manner as before, the possible states of particles have to be confined to *electron states* only, i.e., to the positive part of the spectrum of the Dirac Hamiltonian (2.23).

A relativistic *current density-functional theory* (CDFT), has been developed by Vignale and Rasolt [Vignale and Rasolt, 1987, 1988). In order to calculate the ground-state energy one can perform the functional Legendre transformation in quite an analogous way as in the non-relativistic theory. Note, that in CDFT the new variables are the four-current $J^{\mu} = \psi(\mathbf{r})\gamma^{\mu}\psi(\mathbf{r})$ ($\bar{\psi}$ denotes $\psi^{\dagger}\beta$)or the density and the magnetization density $(n(\mathbf{r}), \mathbf{M}(\mathbf{r}))$, the latter one is defined by

$$-\mathrm{eJ(r)} = \mathrm{V} \times \mathbf{M(r)} \quad , \tag{2.24}$$

where J(r) is the three-current density. In stationary states, J(r) can be written as

$$-\mathrm{eJ(r)} = -\frac{e}{2m}\nabla \times (\mathbf{L(r)} + 2\mathbf{S(r)}) \quad , \tag{2.25}$$

where L(r) is the so-called *angular momentum density*, defining the orbital current density as

$$\frac{1}{2i\hbar}\nabla \times \mathbf{L(r)} = \frac{1}{2m}\bar{\psi}(\mathbf{r})(-i\overleftarrow{\nabla} + i\vec{\nabla} + 2e\mathbf{A(r)})\psi(\mathbf{r}) \quad , \tag{2.26}$$

and $\mathbf{S}$(r) is the *spin density*

$$\mathbf{S(r)} = \frac{1}{2}\bar{\psi}(\mathbf{r})\vec{\Sigma}\psi(\mathbf{r}) \quad , \tag{2.27}$$

with

$$\vec{\Sigma} = \begin{pmatrix} \vec{\sigma} & 0 \\ 0 & \vec{\sigma} \end{pmatrix} \quad . \tag{2.28}$$

and $\vec{\sigma}$ denoting the usual Pauli matrices. One can obtain the *Kohn-Sham-Dirac equation* by varying the total energy functional with respect to $\bar{\psi}$. As mentioned in the previous section, within the LDA, ε_{xc} stems from the homogeneous electron gas where the angular momentum density is zero. Therefore, LDA totally neglects the inter-orbital current-current interactions. In this case, one gets a simple form of the Kohn-Sham-Dirac equation,

$$\left(-ic\vec{\alpha}\nabla + \beta mc^2 + v_{ext}(\mathbf{r}) + v_{xc}(\mathbf{r}) + \frac{e\mu_0}{2m}\mathbf{B}_{eff}(\mathbf{r})\right)\psi_k(\mathbf{r}) = \epsilon_k\psi_k(\mathbf{r}) \quad , \tag{2.29}$$

where the effective magnetic field $\mathbf{B}_{eff}(\mathbf{r})$ is defined as

$$\mathbf{B}_{eff}(\mathbf{r}) = \mathbf{B}_{xc}(\mathbf{r}) + \mathbf{B}_{ext}(\mathbf{r}) \quad , \tag{2.30}$$

i.e., as a sum of the external magnetic field and the so-called *exchange correlation field* as given by

$$\mu_0\mathbf{B}_{xc}(\mathbf{r}) \equiv \frac{\delta E_{xc}}{\delta \mathbf{S}(\mathbf{r})} \quad . \tag{2.31}$$

Using the so-called *local spin (-polarized) density functional approximation* (LSDA) for collinear spin-structures with a spin-quantization axis pointing along the z-axis, $\mathbf{B}_{xc}$ can be expressed as

$$\frac{e\mu_0}{m}\mathbf{B}_{xc}(n_\uparrow(\mathbf{r}), n_\downarrow(\mathbf{r})) = [v_{xc,\uparrow}(n_\uparrow(\mathbf{r}), n_\downarrow(\mathbf{r})) - v_{xc,\downarrow}(n_\uparrow(\mathbf{r}), n_\downarrow(\mathbf{r}))]\, z \quad , \tag{2.32}$$

where $n_\uparrow$ and $n_\downarrow$ are the spin-projected densities, $n(\mathbf{r}) = n_\uparrow(\mathbf{r}) + n_\downarrow(\mathbf{r})$ and 5(r) = $n_\uparrow(\mathbf{r}) - n_\downarrow(\mathbf{r})$. In this approach, the independent variables of the theory are $n_\uparrow$ and $n_\downarrow$. One of the most frequently used local density functional is that of MacDonald *et al.* [MacDonald et al., 1982|.

Chapter 3

The Multiple Scattering Theory

3.1 The Formal Scattering Theory

The time-independent Schrödinger equation for a generalized complex energy eigenvalue *(z)* reads as

$$(z\hat{I} - \hat{H})|\psi\rangle = 0 \quad . \tag{3.1}$$

For later purposes the Hamiltonian, $\hat{H}$ is split into a reference (potential-free) part, $\hat{H}_0$ and a perturbation (potential) operator, $\hat{V}$,

$$\hat{H} = \hat{H}_0 + \hat{V} \quad . \tag{3.2}$$

The *resolvent (Green) operator* is defined by

$$G(z) \equiv (z - \hat{H})^{-1} \quad , \tag{3.3}$$

and, similarly, for the reference system by

$$\hat{G}_0(z) = (z - \hat{H}_0)^{-1} \quad . \tag{3.4}$$

The general solution of Eq. (3.1) can be obtained as the sum of the general solution of the homogeneous $(z - \hat{H}_0)|\phi\rangle = 0$ and a particular solution of the inhomogeneous differential equation $(z - \hat{H}_0)|\psi\rangle = \hat{V}|\psi\rangle$

$$|\psi\rangle = |\phi\rangle + (z - \hat{H}_0)^{-1}\hat{V}|\psi\rangle = |\phi\rangle + \hat{G}_0(z)\hat{V}|\psi\rangle \quad , \tag{3.5}$$

which is usually referred to as the *Lippmann-Schwinger equation* [Lippmann and Schwinger, 1950].

In the basis set of the eigenstates of $\hat{H}$, $\{|n\rangle\}$, $\hat{H}|n\rangle = E_n|n\rangle$, the spectral resolution of the resolvent $\hat{G}(z)$ can be written as

$$\hat{G}(z) = \sum_n \frac{|n\rangle\langle n|}{z - E_n} \quad . \tag{3.6}$$

The coordinate representation of the resolvent operator is called the *Green function,*

$$G(z, \mathbf{r}, \mathbf{r}') = \sum_n \frac{\psi_n(\mathbf{r})\psi_n^*(\mathbf{r}')}{z - E_n} \quad , \tag{3.7}$$

where $\psi_n(\mathbf{r}) = \langle \mathbf{r}|n\rangle$.

One can define two different resolvents (side-limits) at real energies, E,

$$\hat{G}^{\pm}(E) = \lim_{\varepsilon \to 0^+} \hat{G}(E \pm i\varepsilon) = \sum_n \left(\frac{1}{E - E_n} \mp i\pi\delta(E - E_n) \right) |n\rangle\langle n| \quad , \tag{3.8}$$

where P is the principal value integral. $\hat{G}^+$ and $\hat{G}$ are called the *retarded* and the *advanced* Green operators, respectively. With these operators the *density of states* function (DOS) can be expressed as

$$n(E) = \mathrm{Tr}\left\{ \sum_n \delta(E - E_n)|n\rangle\langle n| \right\} = \mp \frac{1}{\pi} \mathrm{Im}\left\{ \mathrm{Tr}\hat{G}^{\pm}(E) \right\} \quad , \tag{3.9}$$

where Tr denotes the trace of an operator. In coordinate representation, the trace of an operator A is defined as

$$\mathrm{Tr}\mathcal{A} = \int \mathrm{d}^3 r \mathcal{A}(\mathbf{r}, \mathbf{r}) \quad . \tag{3.10}$$

The *Dyson equation* for $\hat{G}(z)$ can be obtained from Eqs. (3.2)–(3.4),

$$G(z) = \left(\hat{G}_0^{-1}(z) - \hat{V} \right)^{-1} = G_0(z) + G_0(z) V G(z) \quad . \tag{3.11}$$

As a generalization of Eq. (3.2), the Hamiltonian can be separated in different ways,

$$\hat{H} = \left(\hat{H}_0 + \hat{V}_r \right) + \hat{V} - \hat{V}_r = \hat{H}_r + \hat{} \tag{3.12}$$

where

$$\hat{H}_r = \hat{H}_0 + \hat{V}_r \quad , \tag{3.13}$$

$$\hat{U} = \hat{V} - \hat{V}_r \quad , \tag{3.14}$$

and the resolvent corresponding to $\hat{H}_r$ can be written as

$$\hat{G}_r(z) = (z - \hat{H}_r)^{-1} \quad . \tag{3.15}$$

Eq. (3.12) provides thus a possibility to express the resolvent (3.3) in terms of $\hat{G}_r$,

$$G(z) = G_r(z) + \hat{G}_r(z)\hat{U}\hat{G}(z) \quad , \tag{3.16}$$

an equation frequently called the scaling transformation of the resolvent $\hat{G}(z)$. Solving Eqs. (3.5) and (3.11) by successive iterations one gets the *Born series* for the solution of Eq. (3.1) with Eq. (3.4)

$$|\psi\rangle = |\phi\rangle + \hat{G}_0(z)\hat{V}|\phi\rangle + \hat{G}_0(z)\hat{V}\hat{G}_0(z)\hat{V}|\phi\rangle + \ldots \quad , \tag{3.17}$$

and for the resolvent,

$$\hat{G}(z) = \hat{G}_0(z) + \hat{G}_0(z)\hat{V}\hat{G}_0(z) + \hat{G}_0(z)\hat{V}\hat{G}_0(z)\hat{V}\hat{G}_0(z) + \ldots \quad . \tag{3.18}$$

In terms of the so-called *transition operator*, $\hat{T}(z)$, defined as

$$\begin{aligned} T(z) &= V + VG_0(z)V + VG_0(z)VG_0(z)V + \ldots \\ &= \hat{V} + \hat{V}\hat{G}(z)\hat{V} = \hat{V} + \hat{V}\hat{G}_0(z)\hat{T}(z) \quad , \end{aligned} \tag{3.19}$$

Eq. (3.17) can be rewritten into the form,

$$|\psi\rangle = |\phi\rangle + \hat{G}_0(z)\hat{T}(z)|\phi\rangle \quad , \tag{3.20}$$

and also Eq. (3.18) as

$$G(z) = G_0(z) + \hat{G}_0(z)\hat{T}(z)\hat{G}_0(z) \quad . \tag{3.21}$$

3.2 Calculation of Observables

The quantum-mechanical expectation value of a one-particle operator, $\hat{A}$, restricted to a given energy range (E_a, E_b) can be expressed as

$$A_{ab} = \int_{E_a}^{E_b} \mathrm{d}E \sum_n \delta(E - E_n)\langle n|A|n\rangle \quad . \tag{3.22}$$

By comparing Eq. (3.22) to the expression in Eq. (3.8), one immediately can see that

$$A_{ab} = \mp\frac{1}{\pi}\int_{E_a}^{E_b} dE\, \mathrm{Im}\{\mathrm{Tr}(\hat{A}\hat{G}^{\pm}(E))\} \quad . \tag{3.23}$$

In here some important examples are given, such as the particle density and the total charge contained within a finite volume, Ω,

$$n(\mathbf{r}) = \mp\frac{1}{\pi}\int_{E_a}^{E_b} dE\, \mathrm{Im}\, G^{\pm}(\mathbf{r},\mathbf{r},E) \quad , \tag{3.24}$$

$$q = \mp\frac{1}{\pi}\int_{\Omega} d^3r \int_{E_a}^{E_b} dE\, \mathrm{Im}\, G^{\pm}(\mathbf{r},\mathbf{r},E) \quad , \tag{3.25}$$

the spin magnetization density and the spin magnetic moment

$$\mathbf{m}(\mathbf{r}) = \mp\frac{1}{\pi}\int_{Ea}^{E_b} dE\, \mathrm{Im}\left(\beta\vec{S}\, G^{\pm}(\mathbf{r},\mathbf{r},E)\right) \quad , \tag{3.26}$$

$$\mathbf{M} = \mp\frac{1}{\pi}\int_{\Omega} d^3r \int_{Ea}^{E_b} dE\, \mathrm{Im}\left(\beta\vec{S}\, G^{\pm}(\mathbf{r},\mathbf{r},E)\right) \quad , \tag{3.27}$$

as well as the orbital moment

$$\mathrm{L} = \mp\frac{1}{\pi}\int_{\Omega} d^3r \int_{E_a}^{E_b} dE\, \mathrm{Im}(\beta\vec{L}\, G^{\pm}\, \mathbf{r},\mathbf{r},E)), \tag{3.28}$$

where the notation $\vec{S}$ and $\vec{L}$ stands for the irreducible vector operators of the spin and orbital moments. The expectation value (3.23) can also be calculated in terms of the following contour integral,

$$A_{ab} = -\frac{1}{\pi}\int_{\curvearrowright} \mathrm{Im}\,\mathrm{Tr}(\hat{A}\hat{G}(z)) \tag{3.29}$$

where $\curvearrowright$ denotes the path of integration in the upper complex semi-plane with the lower- and the upper limits at E_a and E_b, respectively. In practice, semi-circular contours are mostly used.

3.3 The Dirac Hamiltonian

For a spherically symmetric potential, with no effective fields, the Kohn-Sham-Dirac equation in Eq. (2.29) takes the form [Rose, 1961],

$$\hat{H}\psi = \begin{pmatrix} (V(r) + mc^2)\mathrm{I}_2 & c\sigma_r\left(\frac{\partial}{\partial r} + \frac{1}{r} - \frac{1}{r}\beta\hat{K}\right) \\ c\sigma_r\left(\frac{\partial}{\partial r} + \frac{1}{r} - \frac{1}{r}\beta\hat{K}\right) & (V(r) - mc^2)\mathrm{I}_2 \end{pmatrix}\psi = W\psi \tag{3.30}$$

where $\sigma_r = \hat{r}\,\vec{\sigma}$ $(\hat{r} = \mathbf{r}/|\mathbf{r}|)$ and

$$K = \vec{\sigma}\vec{\mathrm{T}} + \mathbf{I}\hbar \quad . \tag{3.31}$$

The total angular momentum can be written as

$$\vec{J} = \vec{S} + \vec{L} \quad , \tag{3.32}$$

and H commutes with the operators $J^2, \hat{J}_z$ and K. An eigenstate of the three latter operator can be characterized by the following eigenvalue equations,

$$\hat{J}^2|\chi_{\kappa\mu}\rangle = \hbar^2 j(j+1)|\chi_{\kappa\mu}\rangle \qquad j = l \pm 1/2 \quad , \tag{3.33}$$

$$\hat{J}_z|\chi_{\kappa\mu}\rangle = \hbar\mu|\chi_{\kappa\mu}\rangle \qquad \mu = -j, \ldots, j \quad , \tag{3.34}$$

$$\hat{K}|\chi_{\kappa\mu}\rangle = -\hbar\kappa|\chi_{\kappa\mu}\rangle \qquad \kappa = \begin{cases} l & \text{if } j = l - 1/2 \\ -l-1 & \text{if } j = l + 1/2 \end{cases} \quad , \tag{3.35}$$

where the $\chi_{\kappa\mu}(\hat{r})$ are the so-called *spinor spherical harmonics.* In the two dimensional spinor-space for a fix j these are given by

$$\chi_{\kappa=l,\mu}(\hat{r}) = \begin{bmatrix} \sqrt{\frac{j+\mu}{2j}}Y_{l,\mu-\frac{1}{2}}(\hat{r}) \\ -\sqrt{\frac{j-\mu}{2j}}Y_{l,\mu+\frac{1}{2}}(\hat{r}) \end{bmatrix}, \quad \chi_{\kappa=-l-1,\mu}(\hat{r}) = \begin{bmatrix} \sqrt{\frac{j-\mu+1}{2j+2}}Y_{l,\mu-\frac{1}{2}}(\hat{r}) \\ \sqrt{\frac{j+\mu+1}{2j+2}}Y_{l,\mu+\frac{1}{2}}(\hat{r}) \end{bmatrix} \quad , \tag{3.36}$$

or, in brief,

$$\chi_{\kappa\mu}(\hat{r}) = \sum_{s\,=\,\pm 1/2} C(l,\kappa,1/2|\mu-s,s)Y_{l,\mu-s}(\hat{r})\Phi_s \quad , \tag{3.37}$$

where $Y_{l,m}(\hat{r})$ are the ordinary complex spherical harmonics, $C(l, \kappa, 1/2|\mu - s, s)$ are the Clebsh-Gordan coefficients and the spinor basis functions are defined as

$$\Phi_{1/2} \equiv \begin{bmatrix} 1 \\ 0 \end{bmatrix}, \qquad \Phi_{-1/2} \equiv \begin{bmatrix} 0 \\ 1 \end{bmatrix}. \tag{3.38}$$

The solutions of the free Dirac equation, Eq. (3.30), for $V(r) = 0$ in angular momentum representation are given by [Rose, 1961],

$$F_{\kappa\mu}(W, \mathbf{r}) = \begin{bmatrix} f_l\left(\frac{pr}{\hbar}\right)\chi_{\kappa\mu}(\hat{r}) \\ \frac{iS_\kappa pc\hbar}{W+mc^2} f_{\bar{l}}\left(\frac{pr}{\hbar}\right)\chi_{-\kappa\mu}(\hat{r}) \end{bmatrix}, \tag{3.39}$$

with conjugated counterparts,

$$F^{\dagger}_{\kappa\mu}(W, \mathbf{r}) = \left[f_l\left(\frac{pr}{\hbar}\right)\chi^{+}_{\kappa\mu}(\hat{r}), \quad \frac{-iS_\kappa pc\hbar}{W+mc^2} f_{\bar{l}}\left(\frac{pr}{\hbar}\right)\chi^{+}_{-\kappa\mu}(\hat{r})\right], \tag{3.40}$$

where $S_\kappa = \frac{\kappa}{|\kappa|}$, $F_{\kappa\mu} = J_{\kappa\mu}, N_{\kappa\mu}$, and $H^{\pm}_{\kappa\mu}$ with $f_l = j_l, n_l$, and $h^{\pm}_l (\equiv j_l \pm i n_l)$, the spherical Bessel, Neumann, and Hankel functions, respectively, $\bar{l} = l - S_\kappa$ and p can be obtained from the relativistic energy expression $W = \sqrt{c^2p^2 + m^2c^4}$. In the following for the sake of simplicity the shortcut $H_{\kappa\mu} = H^{+}_{\kappa\mu}$ is used.

In the non-relativistic case, $G^{nr}_0(z, \mathbf{r}, \mathrm{r}')$ can be expressed in a plane-wave representation as [Gonis, 1992]

$$G^{nr}_0(z, \mathbf{r}, \mathbf{r}') = \frac{1}{(2\pi)^3}\int \mathrm{d}^3k \frac{e^{i\mathbf{k}(\mathbf{r}-\mathbf{r}')}}{z - k^2}, \tag{3.41}$$

or, in angular momentum representation as

$$G^{nr}_0(z, \mathbf{r}, \mathbf{r}') = -ip\sum_{L} j_l(pr_<)h^{+}_l(pr_>)Y_L(\hat{r})Y^{*}_L(\hat{r}'). \tag{3-42}$$

where $p^2 - 2mz$ (Im (p) > 0), $L = (l, m)$, $r_< = \min(\mathrm{r}, r')$, $r_> = \max(\mathrm{r}, r')$.

The Green function, $G^{r}_0(W, \mathrm{r}, \mathbf{r}')$ corresponding to the free Dirac equation is defined by

$$(WI_4 - \hat{H})G^{r}_0(W; \mathbf{r}, \mathbf{r}') = \delta(\mathbf{r} - \mathbf{r}')I_4, \tag{3.43}$$

where $\hat{H} = \beta mc^2 + \vec{\alpha}\vec{p}$. Eq. (3.43) can be formally transformed into

$$G^{r}_0(W; \mathbf{r}, \mathbf{r}') = (W - \hat{H})^{-1}\delta(\mathbf{r} - \mathbf{r}')I_4. \tag{3.44}$$

Multiplying Eq. (3.44) from the left with $(W + \hat{H})(W + \hat{H})^{-1} = I_4$ one obtains

$$G_0^r(W;\mathbf{r},\mathbf{r}') = (W + \hat{H})(W + \hat{H})^{-1}(W - \hat{H})^{-1}\delta(\mathbf{r} - \mathbf{r}')I_4 \quad . \tag{3.45}$$

Using the relativistic expression of the energy, $W = \sqrt{c^2p^2 + m^2c^4}$, and also $\hat{H}^2 = \hbar^2c^2\nabla^2 + \mathrm{mV}$

$$(W - \hat{H})^{-1}(W + \hat{H})^{-1} = (W^2 - \hat{H}^2)^{-1} = c^2\left(p^2 - \vec{p}^2\right)^{-1} I_4 \quad , \tag{3.46}$$

where $\vec{p} - \frac{\hbar}{i}$ V is the non-relativistic momentum operator. Consequently,

$$G_0^r(W;\mathbf{r},\mathbf{r}') = \frac{1}{2mc^2}(W + \hat{H})\left[\frac{p^2}{2m} - \frac{\vec{p}^2}{2m}\right]^{-1}\delta(\mathbf{r} - \mathbf{r}')I_4 \quad ! \tag{3.47}$$

which in terms of the non-relativistic free Green function can be expressed as

$$G_0^r(W;\mathrm{r},\mathbf{r}') = \frac{1}{2mc^2}(W + \hat{H})G_0^{nr}(p^2/2m\mathrm{r},\mathbf{r}') \quad . \tag{3.48}$$

Using the functions defined in Eqs. (3.39) and (3.40), G_0^r can then be written as

$$G_0^r(W,\mathrm{r},\mathbf{r}') = -ip\frac{W + mc^2}{2mc^2}\sum_{\kappa,\mu} J_{\kappa\mu}(W,\mathbf{r})H_{\mu}^{\dagger}(W,\mathbf{r}')\theta(r' - \mathrm{r}) +$$
$$H_{\kappa\mu}(W,\mathbf{r})J_{\kappa\mu}^{\dagger}(W,\mathbf{r}')\theta(r - r') \quad . \tag{3.49}$$

Frequently, the approach $(W + mc^2)/2mc^2 - 1$ is used.

3.4 The Single-Site Scattering

A solid can be described as an ensemble of individual scatterers characterized by non-overlapping spatially bounded potentials, *Vi,* centered at lattice positions $\mathbf{R}_i$,

$$V(\mathbf{r}) = \sum_i V_i(\mathbf{r}_i) \qquad (\mathbf{r}_i = \mathbf{r} - \mathbf{R}_i) \tag{3.50}$$

$$V_i(\mathbf{r}_i) = \begin{cases} V_i(r_i) & \text{if } r_i < S_i \\ 0 & \text{elsewhere} \end{cases} \quad . \tag{3.51}$$

In Eq. (3.51) the shape of the potentials are restricted to be spherical symmetric and *Si* are the radii of the bounding spheres. If the spheres do not overlap, one

speaks about the *muffin-tin approach* (MT) and *Si* is called the *muffin-tin radius.* In the region between the spheres the potential is constant which is usually set to zero. In the present calculations the so-called *atomic sphere approximation* (ASA) is used in which the volume of the spheres equal the corresponding Wigner-Seitz cells. Within the ASA, the overlap of the spheres is usually neglected, therefore, the present formalism can be applied with a good accuracy. It should be noted that the Multiple Scattering Theory (MST) is valid for arbitrary shapes of the (regular) potentials [Zabloudil, 2000].

In order to solve the Dirac equation for a potential described in Eq. (3.50) within the MST one first has to solve the *single-site scattering problem* corresponding to the individual potential spheres. In a general case, one can look for a solution of the Dirac equation using the ansatz

$$R(z,\mathbf{r}) = \sum_{Q} R_Q(z,\mathbf{r}) = \sum_{Q} \begin{pmatrix} g_Q(z,r)\chi_Q(\hat{r}) \\ if_Q(z,r)\chi_{\bar{Q}}(\hat{r}) \end{pmatrix} \quad , \tag{3.52}$$

where z denotes the complex extension of the energy ε, defined now as $z = W - mc^2$, $Q = (\kappa, \mu)$ and $\bar{Q} = (-\kappa, \mu)$. Using the real-space representation of Eq. (3.20) with the free solution of the Dirac equation, $J_Q(z,\mathbf{r})$, and the form of the relativistic Green function, Eq. (3.49), one finds that the solution outside the MT sphere is given by

$$R_Q(z,\mathbf{r}) = J_Q(z,\mathbf{r}) - ip \sum_{Q'} H_{Q'}(z,\mathbf{r}) t_{Q'Q}(z) \quad , \tag{3.53}$$

where $t_{Q'Q}(z)$ stands for the matrix element of the $\hat{T}$ operator of the single-site problem, called usually the *single-site t-matrix*,

$$t_{Q'Q}(z) = \int_{r'<S} \mathrm{d}^3 r \int_{r<S} \mathrm{d}^3 r' J^{\times}_{Q'}(z,\mathbf{r}') t(z;\mathbf{r}',\mathbf{r}) J_Q(z,\mathbf{r}) \ . \tag{3.54}$$

One can define another scattering solution as

$$Z_Q(z,\mathbf{r}) = \sum_{Q'} R_{Q'}(z,\mathbf{r}) t^{-1}_{Q'Q}(z) \quad , \tag{3.55}$$

which is normalized outside the MT sphere as

$$Z_Q(z,\mathbf{r}) = \sum_{Q'} J_{Q'}(z,\mathbf{r}') K^{-1}_{Q'Q}(z) + pN_Q(z,\mathbf{r}) \quad , \tag{3.56}$$

where $K_{Q'Q}(z)$ is the so-called reactance matrix given by

$$K^{-1}_{QQ'}(z) = t^{-1}_{QQ'}(z) - ip\delta_{QQ'} \quad . \tag{3.57}$$

In spherically symmetric cases, without magnetic field, $K_{QQ'}(z)$ becomes diagonal and independent from the quantum number μ,

$$K^{-1}_{\kappa}(z) = -p^{-1}\tan\delta_{\kappa}(z) \quad , \tag{3.58}$$

where $\delta_{\kappa}(z)$ is the well-known *phase-shift.* In this case the single-site t-matrix is also diagonal

$$t_{QQ'}(z) = t_{\kappa}(z)\delta_{QQ'}, \quad t_{\kappa}(z) = -p^{-1}\sin\delta_{\kappa}(z)\exp[i\delta_{\kappa}(z)] \; . \tag{3.59}$$

The matching of the solution at the boundary yields the phase-shift,

$$\tan\delta_{\kappa}(z) = -\frac{Q_{\kappa}(z,r)j_l(pr) - pS_{\kappa}j_l(pr)}{Q_{\kappa}(z,r)n_l(pr) - pS_{\kappa}n_l(pr)}, \tag{3.60}$$

where

$$Q_{\kappa}(z,r) = \frac{cf_{\kappa}(z,r)}{g_{\kappa}(z,r)} \quad . \tag{3.61}$$

In a general case, the t-matrix can be obtained by matching the numerical solution of the Dirac equation at the MT radius to (3.56). Note, that the scattering solution, $Z_Q(z,\mathbf{r})$ is regular at the origin, whereas the irregular scattering solution, $I_Q(z,\mathbf{r})$, has to satisfy the following boundary condition at the MT radius,

$$I_Q(z,\mathbf{r})\Big|_{|r|=S} = J_Q(z,\mathbf{r})\Big|_{|r|=S} \quad . \tag{3.62}$$

3.5 Transformation of the Single-site t-matrix

For an arbitrary rotation, $\hat{R}$ acting on the real-space vectors as r' = $\hat{R}\mathbf{r}$ a transformed spinor spherical harmonics can be defined as

$$\hat{R}\chi_Q(\hat{r}) = \chi_Q(\hat{R}^{-1}\hat{r}), \quad \hat{R}\chi^{+}_Q(\hat{r}) = \chi^{+}_Q(\hat{R}^{-1}\hat{r}) \; . \tag{3.63}$$

which can be expressed by

$$\chi_Q(\hat{R}^{-1}\hat{r}) = \sum_{Q'}\chi_{Q'}(\hat{r})D_{Q'Q}(\hat{R}) \quad ,$$
$$\chi^{+}_Q(\hat{R}^{-1}\hat{r}) = \sum_{Q'}D_{QQ'}(\hat{R})^{*}\chi_{Q'}(\hat{r}) \quad , \tag{3.64}$$

where $\underline{D}(R) = \{D_{Q'Q}(R)\}$ is a matrix containing blockwise irreducible spinor representations [Altmann and Herzig, 1994] of R, $\underline{D}^{(\kappa)}(\hat{R})$. Since $\chi_{\kappa\mu}$ and $\chi_{-\kappa\mu}$ correspond to the same quantum number j, their transformations are determined by $\underline{D}^{(\kappa)}(\hat{R}) = \underline{D}^{(-\kappa)}(\hat{R})$ and, therefore, the bispinors (3.39, 3.40) are transformed by the direct product matrices, $\underline{D}(\hat{R}) \otimes I_2$ where I_2 stands for the 2×2 unitary matrix. For the sake of simplicity in the following the notation $\underline{D}(\hat{R})$ is used also for the bispinor representations. As what follows, the underlined quantities stand for matrices in angular momentum indices,

$$\mathcal{A} \equiv \{\mathcal{A}_{LL'}\} \quad \text{in non-relativistic case} \quad , \tag{3.65}$$

$$\mathcal{A} \equiv \{\mathcal{A}_{QQ'}\} \quad \text{in relativistic case} \quad . \tag{3.66}$$

Defining the transformed t-operator, $t'(z; \mathbf{r}', \mathbf{r})$ as

$$t'(z;\mathbf{r}', \mathrm{r}) = \hat{R}t(z;\mathrm{r}', \mathrm{r}) = t(z;\hat{R}^{-1}\mathbf{r}', \hat{R}^{-1}\mathbf{r}) \quad , \tag{3.67}$$

the corresponding matrix elements (3.54) can be obtained as

$$t'_{Q'Q}(z) = \sum_{r'<S}^{J} \mathrm{d}^3r \int_{r<S}^{J} \mathrm{d}^3r' J^{\dagger}_{Q'}(z, \mathbf{r}')t(z; \hat{R}^{-1}\mathbf{r}', \hat{R}^{-1}\mathbf{r})J_Q(z, \mathbf{r}) \quad . \tag{3.68}$$

Changing the variables $\mathrm{r} \to \hat{R}^{-1}\mathbf{r}$ and $\mathbf{r}' \to \hat{R}^{-1}\mathbf{r}'$ yields,

$$t'_{Q'Q}(z) = \int_{r'<S}^{J} \mathrm{d}^3r \int_{r<S}^{J} \mathrm{d}^3r' J^{\dagger}_{Q'}(z, \hat{R}\mathbf{r}')t(z; \mathbf{r}', \mathbf{r})J_Q(z, \hat{R}\mathbf{r}) \quad , \tag{3.69}$$

which can be expressed by using Eq. (3.64),

$$t'_{Q'Q}(z) = \sum_{Q'',Q'''} D_{Q'Q''}(\hat{R}^{-1})^* \int_{r'<S}^{J} \mathrm{d}^3r \int_{r<S}^{J} \mathrm{d}^3r' J^{\dagger}_{Q''}(z, \mathbf{r}')t(z; \mathbf{r}', \mathbf{r}) \times$$
$$J_{Q'''}(z, \mathbf{r})D_{Q'''Q}(\hat{R}^{-1}) \quad , \tag{3.70}$$

or, compactly as,

$$\underline{t}'(z) = \underline{D}^{\dagger}(\hat{R}^{-1})\underline{t}(z)\underline{D}(\hat{R}^{-1}) \quad , \tag{3.71}$$

where $\underline{D}^{\dagger}(\hat{R})$ is the adjungate matrix of $\underline{D}(R)$.

A particular application of Eq. (3.71) can be found in presence of effective field, $\mathbf{B}_{eff}$ such that it can point along an arbitrary direction. In this case, the t-matrix depends on $\mathbf{B}_{eff}$,

$$t(z;\mathbf{r}',\mathbf{r}) = t(z;\mathbf{r}',\mathbf{r},\mathbf{B}_{eff}) \quad . \tag{3.72}$$

The numerical solution of the Dirac equation and thus the determination of the t-matrix is highly simplified when the effective field points along the z-axis (quantization axis) (see chapter A). One can specify a transformation which rotates $\mathbf{B}_{eff}$ to be parallel to the z-axis as,

$$\hat{R}^{-1}\mathbf{B}_{eff} = B_{eff}\hat{z} \quad , \tag{3.73}$$

where z is the unitary vector pointing along the z-axis and $B_{eff} = |\mathbf{B}_{eff}|$. Exploiting the relation,

$$t(z;\mathbf{r}',\mathbf{r},\mathbf{B}_{eff}) = t(z;\hat{R}^{-1}\mathbf{r}',\hat{R}^{-1}\mathbf{r},B_{eff}\hat{z}) \quad , \tag{3.74}$$

one can determine the t-matrix by using (3.71),

$$\underline{t}(z,\mathbf{B}_{eff}) = \underline{D}^{\dagger}(\hat{R}^{-1})\underline{t}^{loc}(z,B_{eff}\hat{z})\underline{D}(\hat{R}^{-1}) \quad . \tag{3.75}$$

where $\underline{t}^{loc}(z,B_{eff}\hat{z})$ is the t-matrix corresponding to the operator $t(z;\mathrm{r}',\mathbf{r},B_{eff}\hat{z})$ which can be calculated by solving the Dirac equation as described in appendix A.

3.6 Multiple Scattering Theory

In this section an expression of the Green function for an ensemble of scatterers described by Eqs. (3.50) and (3.51) will be given. Inserting Eq. (3.50) into Eq. (3.18) one gets

$$\hat{G}(z) = \hat{G}_0(z) + \hat{G}_0(z)\sum_i V_i\hat{G}_0(z) + \hat{G}_0(z)\sum_i V_i\hat{G}_0(z)\sum_j V_j\hat{G}_0(z) + \ldots \quad , \tag{3.76}$$

where the indices $(i,j,\ldots)$ stand for the positions of the scatterers. Similarly to Eq. (3.19) the transition operator can be obtained as

$$T(z) = \sum_i V_i + \sum_{i,j} V_iG_0(z)V_j + \sum_{i,j,k} V_iG_0(z)V_jG_0(z)V_k \ldots \quad . \tag{3.77}$$

Introducing $\hat{Q}^i(z)$ operators as

$$\hat{Q}^i(z) \equiv V_i + V_i\hat{G}_0(z)\sum_j V_j + V_iG_0(z)\sum_{j,k} V_jG_0(z)V_k + \ldots$$
$$= V_i + V_i\hat{G}_0(z)\sum_j \hat{Q}^j(z) \quad , \tag{3.78}$$

one can find for $\hat{T}(z)$ that

$$\hat{T}(z) = \sum_i \hat{Q}^i(z) \quad . \tag{3.79}$$

By making use of the t-operator corresponding to an individual spatially bounded scattering potential corresponding to cell i (3.19),

$$\hat{t}^i(z) = V_i + V_i\hat{G}_0(z)V_i + V_i\hat{G}_0(z)V_i\hat{G}_0(z)V_i + \ldots \quad , \tag{3.80}$$

it can be shown that the $\hat{Q}^i(z)$ can be expressed in terms of $\hat{t}(z)$'s as

$$\hat{Q}^i(z) = \hat{t}^i(z) + \hat{t}^i(z)\hat{G}_0(z)\sum_{j(\neq i)} \hat{Q}^j(z) \quad , \tag{3.81}$$

and, using successive approximation, one finds that

$$\hat{T}(z) = \sum_i \hat{t}^i(z) + \sum_{i\neq j} \hat{t}^i(z)\hat{G}_0(z)\hat{t}^j(z) +$$
$$\sum_{i\neq j\neq k} \hat{t}^i(z)\hat{G}_0(z)\hat{t}^j(z)\hat{G}_0(z)\hat{t}^k(z) + \ldots \quad . \tag{3.82}$$

Introducing the *scattering path operator* (SPO) [Györffy and Stott, 1972] as

$$\hat{\tau}^{ij}(z) = \hat{t}^i(z)\delta_{ij} + \hat{t}^i(z)\hat{G}_0(z)\hat{t}^j(z)(1-\delta_{ij}) + \sum_k^{(k\neq i,j)} \hat{t}^i(z)\hat{G}_0(z)\hat{t}^k(z)\hat{G}_0(z)\hat{t}^j(z) + \ldots$$
$$= \hat{t}^i(z)\delta_{ij} + \hat{t}^i(z)\hat{G}_0(z)\sum_{k(\neq i)} \hat{\tau}^{kj}(z) \quad . \tag{3.83}$$

the transition operator, $\hat{T}(z)$ can be expressed as

$$\hat{T}(z) = \sum_{i,j} \hat{\tau}^{ij}(z) \quad , \tag{3.84}$$

and the resolvent operator $\hat{G}(z)$ as

$$\hat{G}(z) = \hat{G}_0(z) + \hat{G}_0(z) \sum_{i,j} \hat{\tau}^{ij}(z) \hat{G}_0(z) \quad . \tag{3.85}$$

By employing the addition theorem of the Bessel functions ("Kasterin expansion") [Farkas, 1964] in Eq. (3.42) one obtains

$$-ip h_L^*(p^2, \mathbf{r}'_j + \mathbf{R}_j - \mathbf{R}_i) = \sum_{L'} G^{ij}_{0,LL'}(p^2) j^*_{L'}(p^2, \mathbf{r}_j) \quad , \tag{3.86}$$

where

$$G^{ij}_{0,LL'}(p^2) = -4\pi p i^{(l-l'+1)} \sum_{L''} g^L_{L'L''} i^{-l''} h_{L''}(p^2, \mathbf{R}_j - \mathbf{R}_i) \quad , \tag{3.87}$$

and

$$g^L_{L'L''} = \int \mathrm{d}\hat{r} Y^*_L(\hat{r}) Y_{L'}(\hat{r}) Y_{L''}(\hat{r}) \tag{3.88}$$

are Gaunt coefficients, $j_L(p^2, \mathbf{r}) = j_l(pr) Y_L(\hat{r})$ and $j^*_L(p^2, \mathbf{r}) = j_l(pr) Y^*_L(\hat{r})$ while $h_L(p^2, \mathbf{r})$ is defined in a similar manner. Therefore, $G_0^{nr}(z, \mathrm{r}, \mathrm{r}')$ (3.42) can be expanded in terms of Bessel functions centered around the ith and jth site $(i \neq j)$ as follows,

$$G_0^{nr}(z, \mathbf{r}_i + \mathbf{R}_i, \mathbf{r}_j + \mathbf{R}_j) = \sum_{L,L'} j_L(p^2, \mathbf{r}_i) G^{ij}_{0,LL'}(p^2) j^*_{L'}(p\hat{\mathbf{r}}_j) \quad . \tag{3.89}$$

In here the $G^{ij}_{0,LL'}(p^2)$ are called the *non-relativistic bare structure constants.* As can be seen in Eq. (3.87) $G^{ij}_{0,LL'}$ is determined exclusively by the geometrical structure of the system and depends only on the difference $\mathbf{R}_j - \mathbf{R}_i$. For the structure constant one can use the notations such as

$$\underline{G}_0(p^2; \mathbf{R}_i, \mathbf{R}_j) \equiv \underline{G}^{ij}_0(p^2) \quad , \tag{3.90}$$

and as implied by Eq. (3.87),

$$\underline{G}_0(p^2; \mathbf{R}_j - \mathbf{R}_i) \equiv \underline{G}_0(p^2; 0, \mathbf{R}_j - \mathbf{R}_i) \quad . \tag{3.91}$$

Using the relationship between the relativistic and non-relativistic Green function in Eq. (3.48), a corresponding expression for the relativistic Green function can easily be found,

$$G_0^r(z, \mathbf{r}_i + \mathbf{R}_i, \mathbf{r}_j + \mathbf{R}_j) = \sum_{\kappa\mu,\kappa'\mu'} J_{\kappa\mu}(z, \mathbf{r}_i) G^{ij}_{0,\kappa\mu,\kappa'\mu'}(z) J^{\dagger}_{\kappa'\mu'}(z, \mathbf{r}_j) \quad , \tag{3.92}$$

with

$$G^{ij}_{0,\kappa\mu,\kappa'\mu'}(z) = \frac{W + mc^2}{2mc^2} \sum_s C(l, \kappa, 1/2|\mu - s, \mu) G^{ij}_{0,lm,l'm'}(z) C(l', \kappa', 1/2|\mu' - s, s) \quad . \tag{3.93}$$

Inserting Eq. (3.92) into Eq. (3.83) leads to [Gonis, 1992]

$$\tau^{ij}_{QQ'}(z) = t^i_{QQ'}(z)\delta_{ij} + \sum_{k \neq i} \sum_{Q_1 Q_2} t^i_{QQ_1}(z) G^{ik}_{0,Q_1Q_2}(z) \tau^{kj}_{Q_2Q'}(z) \tag{3.94}$$

where the matrix-elements of SPO has been introduced similar to Eq. (3.54). In a suitable matrix formalism [Weinberger, 1990] it can be written as

$$\boldsymbol{\tau}(z) = \left(\mathbf{t}^{-1}(z) - \mathbf{G}_0(z)\right)^{-1} \tag{3.95}$$

where

$$t(z) = \left\{\underline{t}^i(z)\delta_{ij}\right\}, \quad \boldsymbol{\tau}(z) = \left\{\underline{\tau}^{ij}(z)\right\}, \quad \mathbf{G}_0(z) = \left\{\underline{G}^{ij}_0(z)\right\} \quad . \tag{3.96}$$

The frequently used *KKR matrix* can be introduced as

$$\mathbf{M}(z) = \boldsymbol{\tau}(z)^{-1} \quad . \tag{3.97}$$

It should be noted that in Eq. (3.95) the geometrical information on the lattice contained by $\mathbf{G}_0$ and the atomic (scattering) properties of the individual scatterers described by the *t*-matrix are conveniently separated. Starting from Eq. (3.85), after quite lengthy but straightforward manipulations one can derive the Green function [Faulkner and Stocks, 1980] as

$$G(z, \mathbf{r}_i, \mathbf{r}'_j) = \sum_{Q,Q'} \Big[Z^i_Q(z, \mathbf{r}_i) \tau^{ij}_{QQ'}(z) Z^{j\dagger}_{Q'}(z, \mathbf{r}'_j) - \\ - \delta_{ij}\delta_{QQ'} \left(\theta(r_i - r'_i) Z^i_Q(z, \mathbf{r}'_i) I^{i\dagger}_{Q'}(z, \mathbf{r}_i) + \theta(r'_i - r_i) I^i_Q(z, \mathbf{r}'_i) Z^{i\dagger}_{Q'}(z, \mathbf{r}_i) \right) \Big] \quad , \tag{3.98}$$

where the regular and irregular scattering solutions, $Z_Q^i(z,\mathbf{r}_i)$ and $I_Q^i(z,\mathbf{r}_i)$ have been introduced in the previous section, see Eqs. (3.55) and (3.62), respectively; the indices i and j label cells from which r and r' are originating.

Recalling the form of the Green function in Eq. (3.98) it is obvious that when inserted into Eq. (3.29), the expectation value of a one-particle operator can naturally be split into contributions with respect to cells indexed by i. Furthermore, since the scattering solutions and the r-matrix can be transformed from the (AC,μ) basis to the (l,m,s) basis via the Clebsh-Gordan coefficients, $C(l,K,1/2|\mu\text{-}\,\mathrm{s},\mathrm{s})$, projections of these expectation values associated with a given l and s quantum-number can also be defined. However, it is important to underline that these projections merely serve as interpretations of the results, since neither l nor s is a good quantum-number in a relativistic description of the electronic structure of solids.

Chapter 4

Generalized KKR

The range of possible applications of the conventional KKR method using the free space as the reference system is limited. In order to extend this range, multiple-scattering theory can be generalized simply by changing the *reference system.* The freedom of choice of an arbitrary reference potential provides a universal theoretical framework [Braspenning and Lodder, 1994; Lodder and Braspenning, 1994; Lodder and Dekker, 1994] for applications such as the coherent potential approximation (CPA) [Soven, 1967; Györffy, 1972] for describing metallic alloys, the screening transformation of the structure constant (SKKR) [Szunyogh et al., 1994a,b| as well as the embedding technique of the MST [Podloucky et al., 1980; Weinberger et al., 1988|.

Using the potential construction introduced in Eq. (3.51), one can describe the chosen reference system as

$$V_r(\mathbf{r}) = \sum_i V_{r,i}(\mathbf{r}_i) \qquad (\mathbf{r}_i = \mathbf{r} - \mathbf{R}_i) \quad . \tag{4.1}$$

The SPO matrix , $\tau_r\,(z)$, corresponding to $V_r(\mathbf{r})$ reads as

$$\tau_r\,(z) = \left[\mathbf{t}_r\,(z)^{-1} - \mathbf{G}_0\,(z)\right]^{-1} \tag{4.2}$$

where $\mathbf{t}_r\,(z) = \{\underline{t}_r^i\,(z)\,\delta_{ij}\}$s the site diagonal super-matrix containing $\underline{t}_r^i$ (z), the single-site scattering matrices corresponding to $V_{r,i}(\mathbf{r}_i)$. In order to relate the *T*-matrix of the reference system to that of the system of interest, the KKR matrix (3.97) can be manipulated as

$$\begin{aligned} \mathbf{M}\,(z) &= \mathbf{t}_r\,(z)^{-1} - \Delta\mathbf{t}\,(z)^{-1} - \mathbf{G}_0\,(z) \\ &= \left[\mathbf{I} - \mathrm{At}\,(z)^{-1}\left(\mathbf{t}_r\,(z)^{-1} - \mathrm{Go}\,(z)\right)^{-1}\right]\left(\mathbf{t}_r\,(z)^{-1} - \mathrm{Go}\,(z)\right) \end{aligned} \tag{4.3}$$

which gives,

$$\tau(z) = \tau_r(z)\,[I - \Delta t(z)^{-1} Tr(z)]^{-1} \quad , \tag{4.4}$$

where $\mathrm{At}(z)^{-1}$ is defined by

$$\Delta \mathbf{t}(z)^{-1} \equiv \mathbf{t}_r(z)^{-1} - \mathbf{t}(z)^{-1} \quad . \tag{4.5}$$

For practical reasons it is useful to derive an equivalent formulation of the generalized MST in which one can change GO *(z)* in Eq. (3.95). For this reason one can introduce the *structural Green function matrix* as

$$\begin{aligned} \mathbf{G}(z) &\equiv \mathbf{t}(z)^{-1}\,\boldsymbol{\tau}(z)\mathbf{t}(z)^{-1} - \mathbf{t}(z)^{-1} \\ &= \mathbf{G}_0(z) + \mathbf{G}_0(z)\,T(z)\,\mathrm{Go} \quad , \end{aligned} \tag{4.6}$$

which in the angular momentum-representation can be written as

$$\underline{G}^{nm}(z) = G_0^{nm}(1 - \delta_{mn}) + \sum_{j(\neq n)} \sum_{k(\neq m)} G_0^{nj} \tau^{jk} G_0^{km} \quad . \tag{4.7}$$

By using Eq. (3.95) $\mathbf{G}(z)$ can be expressed as,

$$\mathrm{G(z)} = \mathbf{G}_0(z)\,[\mathbf{I} - \mathbf{t}(z)\,\mathbf{G}_0(z)]^{-1} \quad . \tag{4.8}$$

and, similarly, for the reference system (V_r) as

$$\mathbf{G}_r(z) = \mathbf{G}_0(z)\,[\mathbf{I} - \mathbf{t}_r(z)\mathbf{G}_0(z)]^{-1} \quad . \tag{4.9}$$

Eqs. (4.8) and (4.9) can formally be rewritten as

$$\mathbf{G}(z)^{-1} = \mathbf{G}_0(z)^{-1} - \mathbf{t}(z) \quad , \tag{4.10}$$

$$\mathbf{G}_r(z)^{-1} = \mathbf{G}_0(z)^{-1} - \mathbf{t}_r(z) \quad , \tag{4.11}$$

from which one can find the relation

$$\mathbf{G}(z)^{-1} = \mathbf{G}_r(z)^{-1} - \mathbf{t}(z) + \mathbf{t}_r(z) \quad . \tag{4.12}$$

Introducing the notation $\mathbf{t}_\Delta(z)$,

$$\mathbf{t}_\Delta(z) \equiv \mathbf{t}(z) - \mathbf{t}_r(z) \quad , \tag{4.13}$$

$$\{\mathbf{t}_\Delta(z)\}_{ij} = \underline{t}^i_\Delta(z)\,\delta_{ij} = \left(\underline{t}^i(z) - t(z)\right) \text{ tfy} \quad , \tag{4.14}$$

a compact form for the structural Green function matrix can be given,

$$\begin{aligned} G(z) &= \mathbf{G}_r(z)\left[\mathbf{I} - \mathbf{t}_\Delta(z)\,\mathbf{G}_r(z)\right]^{-1} \\ &= \mathbf{G}_r(z) + \mathbf{G}_r(z)\mathbf{t}_\Delta(z)\,\mathbf{G}_r(z) + \mathbf{G}_r(z)\mathbf{t}_\Delta(2)\,\mathbf{G}_r(z)\mathbf{t}_\Delta(z)\,\mathbf{G}_r(z) + \ldots \\ &= \mathbf{G}_r(z) + \mathbf{G}_r(z)\mathbf{t}_\Delta(z)\,\mathbf{G}(z) \quad . \end{aligned} \tag{4.15}$$

It can be shown [Braspenning and Lodder, 1994] that the $\underline{t}_\Delta(z)$ is the single-site scattering matrix corresponding to the potential (see also Eqs. (3.12)–(3.16))

$$U_i(\mathbf{r}) = V_i(\mathbf{r}) - V_{r,i}(\mathbf{r}) \quad . \tag{4.16}$$

In order to find a relation between the r-matrix of the investigated system and the structural Green function matrix one can use the definition at Eq. (4.6) as

$$\mathrm{t}(z) + \mathbf{t}(2)\,\mathrm{G}(2)\,\mathrm{t}(2) = \boldsymbol{\tau}(z) \tag{4.17}$$

and similarly

$$\mathbf{t}_\Delta(z) + \mathbf{t}_\Delta(2)\,\mathrm{G}(z)\,\mathbf{t}_\Delta(z) = \boldsymbol{\tau}_\Delta(z) \tag{4.18}$$

where the $\boldsymbol{\tau}_\Delta(z)$ matrix is defined analogously to Eq. (3.95) as

$$\boldsymbol{\tau}_\Delta(z) \equiv \left[\mathbf{t}_\Delta(z)^{-1} - \mathbf{G}_r(z)\right]^{-1} \quad . \tag{4.19}$$

Using the fact that G (z) is the same for both systems (4.17, 4.18) one finally obtains

$$\boldsymbol{\tau}(z) = \mathbf{t}(z)\,\mathbf{t}_\Delta(z)^{-1}\,\boldsymbol{\tau}_\Delta(z)\,\mathbf{t}_\Delta(z)^{-1}\,\mathbf{t}(z) - \mathbf{t}(z)\,\mathbf{t}_\Delta(z)^{-1}\,\mathbf{t}_r(z) . \tag{4.20}$$

In this section two equivalent formalisms based on the freedom of choice of the reference system were derived in order to extend the ordinary MST method. In Eq. (4.4) one can use the SPO matrix of the reference system which is useful for the embedding method (see chapter 6). In the other formalism which is represented by Eqs. (4.11) and (4.19) by using a suitable reference system the structure constants can be transformed to be short-ranged in real space, which is highly desirable for surface and interface calculations due to the lack of translational symmetry along the z-axis (see chapter 5).

Chapter 5

The Screened KKR Method for Layered Systems

The idea of using a transformation to make the structure constants short-ranged was first put forward by Anderson *et al.* [Andersen and Jepsen, 1984] by introducing a suitable basis set within the LMTO method. A decade later the concept of the *screening* of the structure constants was transfered to the KKR method by Szunyogh *et al.* [Szunyogh et al., 1994a,b] and applied for layered systems. It was shown by Zeller *et al.* [Zeller et al., 1995] that the transformation of the structure constants, in order to make them short-ranged can be interpreted within the framework of the generalized KKR method (see chapter 4) as introducing a reference system with a uniform repulsive potential. Exploiting the rapid spatial decay of the screened structure constants the computational time scales linearly with the linear size of the investigated system, N in contrast to the non-screened N^3-scaling.

In the following a detailed description of the treatment of layered systems (surfaces, interfaces) and the application of the screening method will be given.

5.1 Layered Systems

The aim is to calculate physical properties of magnetic impurities embedded into layered systems. Therefore, one first needs an accurate method to calculate the electronic structure of the surrounding host. In the case of a surface or interface, the 3d-translational symmetry is broken perpendicular to the layers (along the z direction if the layers lie in the xy plane). Thus, one can employ only a two-

dimensional lattice Fourier transformation. A layered system with a simple lattice can be built from a 2D lattice, $\mathcal{L}_{\|}$ by augmenting the lattice vectors by $\mathbf{c}_p = p\mathbf{c}_0$ ($p = -\infty, \infty$) where $\mathbf{c}_0$ is the separation vector between two neighboring layers:

$$\mathbf{R}_n = \mathbf{c}_p + \mathbf{T}_i \quad , \tag{5.1}$$

where $\mathbf{T}_i$ 6 $C\backslash\backslash$ is an in-plane lattice vector. The set of the lattice vectors referring to positions in layer p can be defined as

$$\mathcal{L}_p \equiv \{\mathbf{R}_n | \mathbf{R}_n = \mathbf{c}_p + \mathbf{T}_i, \quad \mathbf{T}_i \in \mathcal{L}_{\|}\} \quad , \tag{5.2}$$

and also a corresponding set of position indices can be introduced as

$$L_p = \{j\backslash \quad \mathbf{R}_j \in \mathcal{L}_p\} \quad . \tag{5.3}$$

The real-space structure constants can be written in a layer indexed form for $\mathbf{R}_m$ = Cp + $\mathbf{T}_i$ and $\mathbf{R}_n$ — $\mathbf{c}_q$ - Tj as

$$\underline{G}_0^{pq}(\mathbf{T}_i - \mathbf{T}_j) = \underline{G}_0(\mathbf{c}_p + \mathbf{T}_i - \mathbf{c}_q - \mathbf{T}_j) = \underline{G}_0(\mathbf{R}_m - \mathbf{R}_n \ne \underline{G}_0^{mn} \quad . \tag{5.4}$$

Since $\underline{G}_0^{pq}(\mathbf{T}_i$ — Tj) depends only on the difference $\mathbf{T}_i$ - Tj, the lattice Fourier transformation of the structure constants is defined as

$$\underline{G}_0^{pq}(\mathbf{k}_{\|}) \equiv \sum_{\mathbf{T}_i \in \mathcal{L}_{\|}} \underline{G}_0^{pq}(\mathbf{T}_i)\, e^{i\mathbf{k}_{\|}\mathbf{T}_i} \quad . \tag{5.5}$$

Introducing the notation

$$\underline{G}_0^{pi,qj} \equiv \underline{G}_0(\mathbf{R}_m = \mathbf{c}_p + \mathbf{T}_i,\ \mathbf{R}_n = \mathbf{c}_q + \mathbf{T}_j) \quad , \tag{5.6}$$

the real-space structure constant can be expressed as,

$$\underline{G}_0^{pi,qj} = \frac{1}{\Omega_{SBZ}} \int_{SBZ}^{J} \mathrm{d}^2 k_{\|} \underline{G}_0^{pq}(\mathbf{k}_{\|})\, e^{-i\mathbf{k}_{\|}(\mathbf{T}_i - \mathbf{T}_j)} \quad , \tag{5.7}$$

where Ω_{SBZ} is now the volume of the two dimensional (surface) Brillouin-zone (SBZ) and k‖ lies in the first 2D Brillouin-zone. It should be noted that applying the formalism in terms of $\mathbf{k}_{\|}$ means that the in-plane directions *(x, y)* are treated in Fourier-space while with respect to the z-direction (perpendicular to the layers)

a real-space approach is used. Similarly to (5.5) a new matrix notation can be introduced for the t-matrices, SPO and the structure constant in terms of layer indices (p, q),

$$\mathbf{t} = \{\underline{t}^p \delta_{pq}\}, \quad \mathbf{G}_0(\mathbf{k}_{||}) = \{\underline{G}_0^{pq}(\mathbf{k}_{||})\}, \quad \boldsymbol{\tau}(\mathbf{k}_{||}) = \{\underline{\tau}^{pq}(\mathbf{k}_{||})\} \quad , \tag{5.8}$$

where t^p is the t-matrix corresponding the uniform potential in layer p

$$\underline{t}^p(\mathbf{z}) = \underline{t}^n(z), \quad n \in L_p \quad . \tag{5.9}$$

From Eq. (3.95) one can deduce

$$\boldsymbol{\tau}(z; \mathbf{k}_{||}) = \left(\mathbf{t}^{-1}(z) - \mathbf{G}_0(z; \mathbf{k}_{||})\right)^{-1} \tag{5.10}$$

Due to the asymptotic behavior of the Bessel functions, the free Green function decays slowly in real-space at positive energies. The long-ranged GO $(\mathbf{k}_{||})$ can be partitioned as,

$$\mathrm{GO} = \begin{pmatrix} \mathbf{G}_{0,LL} & \mathbf{G}_{0,LI} & \mathbf{G}_{0,LR} \\ \mathbf{G}_{0,IL} & \mathbf{G}_{0,II} & \mathbf{G}_{0,IR} \\ \mathbf{G}_{0,RL} & \mathbf{G}_{0,RI} & \mathbf{G}_{0,RR} \end{pmatrix} \begin{array}{ll} \text{left } (L): & -\infty < p < 0 \\ \text{interface } (I): & 1 < p < N \\ \text{right } (R): & N + l < p < \infty \end{array} \quad , \tag{5.11}$$

where N is the number of the layers within the studied interface region and in (5.11) the k|| argument is dropped. This partitioning reflects the treatment of layered systems within the SKKR method, where the left and the right region (L, R) represent semi-infinite substrates (or the vacuum region) in which all layers are assumed to be identical, thus one can use a unique t-matrix for the left-hand side, $t^L(z)$ and the right-hand side. $t^R(z)$ bulk. In order to get a smooth crossover between the bulk and the surface, one can ad some "bulk layers", called buffer layers, to the interface region /. In Eq. (5.10) one has to invert a matrix with infinite dimension (in layer indices) (see Eq. (5.8)) which can not be performed directly. Introducing, however, a repulsive potential, V_r, which is usually 1 — 2 Ry above the valence band, as a reference system, the reference Green function, $G_r(z)$ becomes spatially localized [Szunyogh et al., 1994b]. If, in terms of the matrix-notation (5.8), $\mathbf{t}_r(z)$ denotes the single-site t-matrices of the uniform repulsive potentials, V_r, the so-called screened counterpart of the t-matrices can be defined as in Eq. (4.13). The structure constants in the screened representation are defined as the structural Green function of

the reference system,

$$\mathbf{G}_r(z;\mathbf{k}_{||}) = \mathrm{Go}(2;\mathbf{k}_{||})\,[\mathrm{I} - \mathbf{t}_r(z)\,\mathrm{Go}(z;\mathbf{k}_{||})]^{-1} \quad , \tag{5.12}$$

and the SPO in the screened representation can be given as

$$\tau_\Delta(z;\mathbf{k}_{||}) = [\mathbf{t}_\Delta(z)^{-1} - \mathbf{G}_r(z;\mathbf{k}_{||})]^{-1} \quad . \tag{5.13}$$

As what follows, the subscript A of the M and T matrices will be dropped and if not stated otherwise, the forms correspond to the screened representation. Since $\mathbf{G}_r(z;\mathbf{k}_{||})$ stands, essentially, for a matrix representation of the resolvent of the reference system, it is found to be decaying exponentially in real space [Szunyogh et al., 1994b|. As the numerical tests in Ref. [Szunyogh et al., 1994b] proved that $\underline{G}_r^{pq}(z;\mathrm{k}||)$ is now well localized, therefore, it can be truncated for $|p-q| > \mathrm{n}$, $n \approx 3$ in BCC and FCC systems. Thus $\mathbf{G}_r(z,\mathrm{k}||)$ and therefore $\mathrm{M}(z;\mathbf{k}_{||}) = (\tau(\mathrm{z};\mathbf{k}_{||}))^{-1}$ can be viewed to be block-tridiagonal

$$\mathrm{M} = \begin{pmatrix} \ddots & \ddots & 0 & 0 & 0 \\ \ddots & \mathbf{M}_{P,P} & \mathbf{M}_{P,P+1} & 0 & 0 \\ 0 & \mathbf{M}_{P+1,P} & \mathbf{M}_{P+1,P+1} & \mathbf{M}_{P+1,P+2} & 0 \\ 0 & 0 & \mathbf{M}_{P+2,P+1} & \mathrm{M}P+2,P+2 & \ddots \\ 0 & 0 & 0 & \ddots & \ddots \end{pmatrix} \tag{5.14}$$

where the $\mathbf{M}_{P,Q}$ blocks are labeled by the so-called *principal layer* index. It should be noted that a principal layer contains n subsequent atomic layers,

$$\mathbf{M}_{P,Q}(\mathbf{k}_{||}) \equiv \{\underline{M}^{pq}(\mathbf{k}_{||})\} \quad \begin{matrix} p = (P-1)\,n+1,\ldots,Pn \\ q = (Q-1)\,n+1,\ldots,Qn \end{matrix} \quad . \tag{5.15}$$

Assuming that the separation between adjacent layers is identical in the whole system one can write for the interface-interface region,

$$\begin{aligned} \mathbf{M}_{P,P}(z;\mathbf{k}_{||}) &= \mathbf{t}_\Delta^P(z)^{-1}\,\delta_{PP} - \mathbf{G}_{r,00}(z;\mathbf{k}_{||}) \quad , \\ \mathbf{M}_{P+1,P}(z;\mathbf{k}_{||}) &= \mathbf{M}_{P+2,P+1}(2;\mathbf{k}_{||}) = -\mathbf{G}_{r,10}(z;\mathbf{k}_{||}) \quad , \\ \mathbf{M}_{P,P+1}(z;\mathbf{k}_{||}) &= \mathbf{M}_{P+1,P+2}(z;\mathbf{k}_{||}) = -\mathbf{G}_{r,01}(z;\mathbf{k}_{||}) \quad , \end{aligned} \tag{5.16}$$

where

$$\begin{aligned}
\left\{\mathbf{t}_{\Delta}^{P}(z)^{-1}\right\}_{pq} &\equiv \underline{t}_{\Delta}^{l}(z)^{-1}\delta_{pq} \quad \text{where } l=(P-1)n+p \quad , \\
\left\{\mathbf{G}_{r,00}\left(z;\mathbf{k}_{\|}\right)\right\}_{pq} &\equiv \underline{G}_{r}^{pq}\left(z;\mathbf{k}_{\|}\right) \quad , \\
\left\{\mathbf{G}_{r,01}\left(z;\mathbf{k}_{\|}\right)\right\}_{pq} &\equiv \underline{G}_{r}^{p,n+q}\left(z;\mathbf{k}_{\|}\right) \quad , \\
\left\{\mathbf{G}_{r,10}\left(z;\mathbf{k}_{\|}\right)\right\}_{pq} &\equiv \underline{G}_{r}^{n+p,q}\left(z;\mathbf{k}_{\|}\right) \quad ,
\end{aligned} \tag{5.17}$$

and p = 1, . . . , *n* and *q* = 1, . . . , *n*. Using a similar partitioning as in Eq. (5.11), M *(z;* k||) takes the form,

$$\mathrm{M} = \begin{pmatrix} \mathrm{M}_{L,L} & \mathrm{M}_{L,I} & 0 \\ \mathrm{M}_{I,L} & \mathrm{M}_{I,I} & \mathrm{M}_{I,t} \\ 0 & \mathrm{M}_{R,I} & \mathrm{M}_{R,R} \end{pmatrix} \quad , \tag{5.18}$$

where the block-diagonal elements for an interface region consisting of N_{PL} principal layers can be written,

$$\mathbf{M}_{LL} = \begin{pmatrix} \ddots & \ddots & 0 & & \\ \cdots & \mathrm{M}_{-2,-2} & \mathrm{M}_{-2,-1} & 0 & \\ 0 & \mathrm{M}_{-1,-2} & \mathrm{M}_{-1,-1} & \mathrm{M}_{-1,0} & \\ & 0 & \mathrm{M}_{0,-1} & \mathrm{M}_{0,0} & \end{pmatrix} \tag{5.19}$$

$$\mathbf{M}_{II} = \begin{pmatrix} \mathrm{M}_{1,1} & \mathrm{M}_{1,2} & 0 & & \\ \mathrm{M}_{2,1} & \mathrm{M}_{2,2} & \mathrm{M}_{2,3} & 0 & \\ 0 & \mathrm{M}_{3,2} & \ddots & \ddots & 0 \\ & 0 & \ddots & \ddots & \mathrm{M}_{N_{PL}-1,N_{PL}} \\ & & 0 & \mathrm{M}_{N_{PL},N_{PL}-1} & \mathrm{M}_{N_{PL},N_{PL}} \end{pmatrix} \tag{5.20}$$

$$\mathbf{M}_{LL} = \begin{pmatrix} \mathrm{M}_{N_{PL}+1,N_{PL}+1} & \mathrm{M}_{N_{PL}+1,N_{PL}+2} & 0 & \\ \mathrm{M}_{N_{PL}+2,N_{PL}+1} & \mathrm{M}_{N_{PL}+2,N_{PL}+2} & \mathrm{M}_{N_{PL}+2,N_{PL}+3} & 0 \\ 0 & \mathrm{M}_{N_{PL}+3,N_{PL}+2} & \ddots & \ddots \\ & 0 & \ddots & \ddots \end{pmatrix} \quad , \tag{5.21}$$

and the off-diagonal parts contain one non-vanishing block only,

$$(\mathbf{M}_{I,L})_{PQ} = \mathrm{M}_{1,0}\delta_{P1}\delta_{Q0}, \quad (\mathbf{M}_{L,I})_{PQ} = \mathrm{M}_{0,1}\delta_{P0}\delta_{Q1} \quad , \tag{5.22}$$

$$(\mathbf{M}_{I,R})_{PQ} = \mathbf{M}_{0,1}\delta_{P,N}\delta_{Q,N+1}, \quad (\mathbf{M}_{R,I})_{PQ} = \mathbf{M}_{1,0}\delta_{P,N+1}\delta_{Q,N} \quad . \tag{5.23}$$

Using the relation,

$$\mathbf{M}\left(z;\mathbf{k}_{||}\right)\boldsymbol{\tau}\left(z;\mathbf{k}_{||}\right) = \mathbf{I} \quad , \tag{5.24}$$

it can be shown that the interface-interface (/, /) part of $\boldsymbol{\tau}$ (z; $\mathbf{k}_{||}$) which is the object of interest can be written as [Szunyogh et al., 1994b],

$$\boldsymbol{\tau}_{II} = \left[\mathbf{M}_{I,I} - \mathrm{M/,i}\left(\mathbf{M}_{L,L}\right)^{-1}\mathbf{M}_{L,I} - \mathbf{M}_{I,R}\left(\mathbf{M}_{R,R}\right)^{-1}\mathbf{M}_{R,I}\right]^{-1} \quad . \tag{5.25}$$

Inserting Eqs. (5.22) and (5.23) into (5.25) one can immediately gets

$$\left[\mathbf{M}_{I,L}\left(\mathbf{M}_{L,L}\right)^{-1}\mathbf{M}_{L,I}\right]^{PQ} = \mathbf{M}_{1,0}\boldsymbol{\tau}^{L}\mathbf{M}_{0,1}\delta_{P,1}\delta_{Q,1} \quad , \tag{5.26}$$

$$\left[\mathbf{M}_{I,R}\left(\mathbf{M}_{R,R}\right)^{-1}\mathbf{M}_{R,I}\right]^{PQ} = \mathbf{M}_{0,1}\boldsymbol{\tau}^{R}\mathbf{M}_{1,0}\delta_{P,N}\delta_{Q,N} \tag{5.27}$$

where $\boldsymbol{\tau}^{L}$(z; $\mathbf{k}_{||}$) and $\boldsymbol{\tau}^{R}\left(z;\mathrm{k}_{||}\right)$, defined as

$$\boldsymbol{\tau}^{L}\left(z;\mathbf{k}_{||}\right) = \left[\left(\mathbf{M}_{L,L}\left(z;\mathbf{k}_{||}\right)\right)^{-1}\right]_{11} \quad \boldsymbol{\tau}^{R}\left(z;\mathbf{k}_{||}\right) = \left[\left(\mathbf{M}_{R,R}\left(\mathrm{z};\mathbf{k}_{||}\right)\right)^{-1}\right]_{N+1,N+1} \quad , \tag{5.28}$$

are usually referred to as the *surface SPO* serving as boundary conditions due to the L and R bulk regions. The matrices $\boldsymbol{\tau}^{L}$(z; $\mathbf{k}_{||}$) and $\boldsymbol{\tau}^{R}\left(z;\mathbf{k}_{||}\right)$ can be calculated from the conditions,

$$\boldsymbol{\tau}^{L}_{00}\left(z;\mathbf{k}_{||}\right) = \left[\mathbf{t}^{L}\left(z;\mathbf{k}_{||}\right)^{-1} - \mathbf{G}_{r,00}\left(z;\mathbf{k}_{||}\right) - \mathbf{G}_{r,10}\left(z;\mathbf{k}_{||}\right)\boldsymbol{\tau}^{L}_{00}\left(2;\mathbf{k}_{||}\right)\mathbf{G}_{r,01}\left(z;\mathbf{k}_{||}\right)\right]^{-1} \quad , \tag{5.29}$$

$$\boldsymbol{\tau}^{R}_{00}\left(z;\mathbf{k}_{||}\right) = \left[\mathbf{t}^{R}\left(z;\mathbf{k}_{||}\right)^{-1} - \mathbf{G}_{r,00}\left(z;\mathbf{k}_{||}\right) - \mathbf{G}_{r,01}\left(z;\mathbf{k}_{||}\right)\boldsymbol{\tau}^{R}_{00}\left(z;\mathbf{k}_{||}\right)\mathbf{G}_{r,10}\left(z;\mathbf{k}_{||}\right)\right]^{-1} \quad , \tag{5.30}$$

arising from the so-called removal invariance of a perfect semi-infinite surface. In practice the so-called *decimation technique* is used to calculate the surface SPO and a high convergence is achieved usually in a few tens of iterations [Sancho et al., 1985). In order to exploit the block-tridiagonal form of M *(z;* $\mathbf{k}_{||}$) the $\mathcal{O}(N)$method suggested by Godfrin is used to invert M [Godfrin, 1991] (see in appendix B).

In a layered system one can calculate the 2D lattice Fourier transform of the screened SPO as

$$\mathrm{r}''\left(\mathrm{z};\mathbf{k}_{||}\right) = \left\{\left[\left(\mathbf{t}_{\Delta}\left(z\right)\right)^{-1} - \mathbf{G}_{r}\left(\mathrm{z},\mathbf{k}_{||}\right)\right]^{-1}\right\}_{J\,pq} \quad . \tag{5.31}$$

Performing the 2D BZ integral

$$\underline{\tau}^{pi,qj}(z) = \frac{1}{\Omega_{SBZ}} \int_{SBZ} \underline{tfkjM}(z;\mathbf{k})\, e^{-i\mathbf{k}_{\parallel}(\mathbf{T}_i-\mathbf{T}_j)} \quad , \tag{5.32}$$

one obtains the real-space SPO in the screened representation. The principal layer concept together with the surface Green function method also allow one to treat the bulk and interface systems on an equal footing, namely, the 3D inverse Fourier transformation can be replaced by a 2D integral over the SBZ and a real-space treatment perpendicular to the surface. In brief: a bulk system can be seen as an interface between two semi-infinite hosts with the condition that the physical properties of the two hosts on both side and the interface have to be identical.

In order to obtain physical properties one needs to evaluate the Green function. According to the 2D translational invariance, it is enough to focus for a single cell in every layer and evaluate the site-diagonal SPO corresponding to this site. Denoting the site-diagonal elements of the SPO matrix in layer p (see the definition at Eq. (5.2)) as follows

$$\underline{\tau}^{p}(z) - \underline{\tau}^{p0,p0}(z) \quad , \tag{5 33}$$

and the screened t-matrices with respect to the uniform potential in layer p as

$$\underline{t}^{p}_{\Delta}(z) = t^{n}(z) - \underline{t}_{r}(z), \quad n \in L_p \tag{5.34}$$

one can calculate the unscreened (physical) τ-matrix as (see Eq. (4.20))

$$\underline{\tau}^{p}(z) = \mathrm{f}(z)\, \underline{t}^{p}_{\Delta}(z)^{-1} \underline{\tau}^{p}_{\Delta}(z) \,\&\, (z)^{-1}\mathrm{f}(z) - \mathrm{f}(z)\, \underline{t}^{p}_{\Delta}(z)^{-1}\, \underline{t}_{r}(z) \quad . \tag{5.35}$$

The layer-resolved contributions to the one-electron observables (DOS, charge, magnetic moment, band-energy) can be then easily calculated from $\underline{\tau}^{p}(z)$ applying the form of the Green function in Eq. (3.98).

In cluster calculations using the embedding technique (see Chapter 6) one needs to know the real-space unscreened SPO for the unperturbed system. The non-site-diagonal elements of SPO can be calculated from screened the ones according to Eq. (4.20),

$$\begin{aligned}\tau^{pi,qj}(z) = {} & \mathrm{f}(z) \,\&\, (z)^{-1} \underline{\tau}^{pi,qj}_{\Delta}(z)\, \underline{t}^{q}_{\Delta}(z)^{-1} \underline{t}^{q}(z) \\ & - \delta_{pq}\delta_{ij}\underline{t}^{p}(z)\, \underline{t}^{p}_{\Delta}(z)^{-1}\, \underline{t}_{r}(z) \quad .\end{aligned} \tag{5.36}$$

5.2 The Surface Brillouin Zone Integration

In this section it is shown how the SBZ integrations (5.32) can be reduced by making use of the point group symmetry of the 2D lattice. This group denoted by $\mathcal{G}$ is also the symmetry group of the reciprocal lattice. The irreducible wedge of the SBZ (IBZ) is the smallest subset of SBZ such that for every $\mathbf{k}_{||} \in$ SBZ a kf| 6 IBZ and a point-group operation $\hat{K}$ 6 Q can be found to satisfy $\hat{R}'\mathbf{k}'_{||} = \mathbf{k}_{||}$. In here calculations for fcc(lOO) and fcc(111) surfaces are performed for which the corresponding groups are shown in Table 5.1. Using the definition of irreducible wedges of the Brillouin zone, the integral in Eq. (5.32) can be rewritten as,

$$\underline{\tau}^{pi,qj}(z) = \frac{1}{\Omega_{IBZ}} \frac{1}{|\mathcal{G}|} \int_{IBZ} \sum_{\hat{R}} e^{-i(\mathbf{T}_i - \mathbf{T}_j)\hat{R}\mathbf{k}_{||}} \underline{\tau}^{pq}(\hat{R}\mathbf{k}_{||}, z) \mathrm{d}^2k \quad , \tag{5.37}$$

where $|\mathcal{G}|$ is the order of group Q. In order to make use of this form one needs to explore the transformation properties of the SPO-matrix. For that purpose one has to use the transformation of structure constants (see Appendix C)

$$\underline{G}_0^{pq}(z; \hat{R}\mathbf{k}_{||}) = e^{-i\Delta\mathbf{c}_{pq,||}\mathbf{k}_{||}} \underline{D}(\hat{R}) \underline{G}_0^{pq}(z; \mathbf{k}_{||}) \underline{D}^{\dagger}(\hat{R}) \quad , \tag{5.38}$$

where $\underline{D}(\hat{R})$ are bispinor representations of transformations $\hat{R}$ in coordinate space. and $\Delta\mathbf{c}_{pq,||}$ is defined as

$$\Delta\mathbf{c}_{pq,||} = \hat{R}^{-1}(\mathbf{c}_p - \mathbf{c}_q) - (\mathbf{c}_p - \mathbf{c}_q) \quad , \tag{5.39}$$

namely is an in-plane vector provided that in the case of fcc(OOl) and fcc(lll) the relation,

$$\hat{R}^{-1}(\mathbf{c}_p - \mathbf{c}_q)_{\perp} = (\mathbf{c}_p - \mathbf{c}_q)_{\perp} \quad , \tag{5.40}$$

is satisfied. Inserting Eq. (5.38) into Eq. (5.10) one obtains the transformation properties of the SPO matrix,

$$\underline{\tau}^{pq}(\hat{R}\mathbf{k}_{||}, \mathrm{z}) = D^{\dagger}(\hat{R}^{-1}) \underline{\tau}^{pq}_{\hat{R}}(\mathbf{k}_{||}, z) D(R^{-1}) e^{i\Delta\mathbf{c}_{pq}\mathbf{k}_{||}} \quad , \tag{5.41}$$

where the matrix $\underline{\tau}^{pq}_{\hat{R}}(\mathbf{k}_{||}, z)$ is introduced as

$$\boldsymbol{\tau}_{\hat{R}}(\mathbf{k}_{||}, z) \equiv \mathbf{M}_{\hat{R}}(\mathbf{k}_{||}, z)^{-1} \quad , \tag{5.42}$$

Surface	Lattice type	Point group	$\|\mathcal{G}\|$
fcc(lOO)	centered rectangular	C_{4v}	8
fcc(111)	hexagonal	C_{3v}	6

Table 5.1: Symmetry groups of fcc(lOO) and fcc(lll) surfaces.

$$\underline{M}^{pq}_{\hat{R}}(\mathbf{k}_{\|}, z) \equiv \underline{D}(\hat{R}^{-1})\underline{t}^{p}(z)^{-1}\delta_{pq}\underline{D}^{\dagger}(\hat{R}^{-1}) - \underline{G}^{pq}_{0}(\mathbf{k}_{\|}, z) \tag{5.43}$$

where the transformation of the $t^{p}(z)^{-1}$ matrices by $\underline{D}(R^{-1})$ is necessary due to independence of the t-matrix from the rotation of the k$\|$ vector. Inserting Eq. (5.41) into (5.37) one obtains,

$$\underline{\tau}^{pi,qj}(z) = \frac{1}{\Omega_{IBZ}}\frac{1}{|\mathcal{G}|} \times \sum_{\hat{R}} \underline{D}^{\dagger}(\hat{R}^{-1}) \left(\int_{IBZ} e^{-i[\hat{R}^{-1}(\mathbf{T}_i - \mathbf{T}_j) - \Delta\mathbf{c}_{pq}]\mathbf{k}_{\|}} \underline{\tau}^{pq}_{\hat{R}}(\mathbf{k}_{\|}, z) \right) \underline{D}(\hat{R}^{-1}) \mathrm{d}^2k \quad . \tag{5.44}$$

It should be noted that in actual calculations the integration over the k-space is replaced by a summation over special k$\|$ points within the IBZ [Cunningham, 1974]. It also has to be noted that Eq. (5.44) helps to save computational time only when there are elements of $\mathcal{G}$ for which

$$\underline{\tau}^{pq}_{\hat{R}}(\mathbf{k}_{\|}, z) = \underline{\tau}^{pq}_{\hat{R}'}(\mathbf{k}_{\|}, z), \quad \hat{R}, \hat{R}' \in \mathcal{G} \quad , \tag{5.45}$$

or equivalently

$$D(\hat{R}^{-1})\underline{t}^{p}(z)^{-1}D^{\dagger}(\hat{R}^{-1}) = D(\hat{R}'^{,-1})\underline{t}^{p}(z)^{-1}D^{\dagger}(\hat{R}'^{,-1}), \quad \forall p \quad . \tag{5.46}$$

If Eq. (5.45) is full-filled the time-consuming inversion in Eq. (5.42) has to be performed only for one $\hat{R}$. The condition at Eq. (5.45) or (5.46) applies for all $\hat{R}$ 6 Q in the case of non-magnetic surfaces. For magnetic surfaces with a magnetization pointing along the symmetry axis (z-direction) the computational effort can be reduced to calculate $\tau_{\hat{R}}(\mathbf{k}_{\|}, z)$ for two $\hat{R}$'s, namely, one for the proper and one for the improper rotations.

Chapter 6

The Embedding Technique

After having introduced the generalized Multiple Scattering Theory, this approach will be applied to the problem of primary interest, namely the electronic and magnetic structure of substitutional impurities and clusters. In general, the problem of impurities on top of surfaces, in different distances near the surface as well in the bulk will be addressed. Since the vacuum region is treated using empty spheres an adatom placed on the top of the surface can be seen technically as a substitutional impurity in the vacuum layer adjacent to the surface. Now the unperturbed host is chosen to be the reference system and one can look for the physical properties of the impurity atoms and the host atoms around them as compared to the unperturbed host. The embedding technique requires that the host system and the perturbed one have the same lattice geometry and, therefore, throughout here no lattice relaxation effects have been considered.

6.1 The τ-matrix of a Single Embedded Atom

For the sake of simplicity first the r-matrix for a single impurity at a position labeled by i_0 is derived. For the host system the potential can be written as

$$V^{host}(\mathbf{r}) = \sum_i V_i^{host}(\mathbf{r}_i) \quad , \tag{6.1}$$

while for a system with a single impurity as

$$V_i(\mathbf{r}_i) = \begin{cases} V_i^{host}(\mathbf{r}_i) & \text{if } i \neq i_0 \\ V^{imp}(\mathbf{r}_i) & \text{if } i = i_0 \end{cases} \quad , \tag{6.2}$$

or, in brief,

$$V_i(\mathbf{r}_i) = V_i^{host}(\mathbf{r}_i)\,(1 - \delta_{ii_0}) + V_i^{imp}(\mathbf{r}_i)\delta_{ii_0} \quad , \tag{6.3}$$

where it should be noted that V_i^{host} could be different for different sites. In the present calculations V_i^{host} are different for different layers. The t-matrices corresponding to the perturbed system can be written as

$$\underline{t}^i(z) = \begin{cases} \underline{t}^i_{host}(z) & \text{if } i \neq i_0 \\ \underline{t}_{imp}(z) & \text{if } i = i_0 \end{cases} \quad . \tag{6.4}$$

Making use of the definition of $\Delta\mathbf{t}^{-1}$ in (4.5) one can write,

$$\Delta\underline{t}^i(z)^{-1} = \begin{cases} 0 & \text{if } i \neq i_0 \\ \underline{t}^{i_0}_{host}(z)^{-1} - \underline{t}_{imp}(z)^{-1} & \text{if } i = i_0 \end{cases} \tag{6.5}$$

or, compactly,

$$\Delta\underline{t}^i(z)^{-1} = \left(\underline{t}^{i_0}_{host}(z)^{-1} - \underline{t}_{imp}(z)^{-1}\right)\delta_{i,i_0} \quad . \tag{6.6}$$

Writing Eq. (4.4) for the τ-matrix describing the system with the impurity embedded into the host yields

$$\boldsymbol{\tau}(z) = \boldsymbol{\tau}_{host}(z)\left[\mathbf{I} - \Delta\mathbf{t}(z)^{-1}\boldsymbol{\tau}_{host}(z)\right]^{-1} \quad , \tag{6.7}$$

which can be expanded as,

$$\begin{aligned} T(Z) \;=\; & \boldsymbol{\tau}_{host}(z)\big[\mathbf{I} + \Delta\mathbf{t}(z)^{-1}\boldsymbol{\tau}_{host}(z) + \\ & + \Delta\mathbf{t}(z)^{-1}\boldsymbol{\tau}_{host}(z)\Delta\mathbf{t}(z)^{-1}\boldsymbol{\tau}_{host}(z) + \ldots\big] \quad . \end{aligned} \tag{6.8}$$

Inserting Eq. (6.5) into Eq. (6.8) it can clearly be seen that $\underline{\tau}^{i_0,i_0}$ can be written as

$$\begin{aligned} \underline{\tau}^{i_0,i_0}(z) = \underline{\tau}^{i_0,i_0}_{host}(z)\,\big[L + \Delta\underline{t}(z)^{-1}\underline{\tau}^{i_0,i_0}_{host}(z) + \\ + \Delta\underline{t}(z)^{-1}\underline{\tau}^{i_0,i_0}_{host}(z)\Delta\underline{t}(z)^{-1}\underline{\tau}^{i_0,i_0}_{host}(z) + \ldots\big] \quad , \end{aligned} \tag{6.9}$$

or, in a more compact form as,

$$\underline{\tau}^{i_0,i_0}(z) = \underline{\tau}^{i_0,i_0}_{host}(z)\left[\underline{I} - \left(\underline{t}^{i_0}_{host}(z)^{-1} - \underline{t}_{imp}(z)^{-1}\right)\underline{\tau}^{i_0,i_0}_{host}(z)\right]^{-1} \tag{6.10}$$

which allows one to obtain the Green function referring to a single impurity using the site diagonal matrix $\underline{\tau}_{host}^{i_0,i_0}$ which is of dimension 1 x 1 in spatial indices in contrary to the whole real-space SPO matrix which obviously is of dimension ∞ x ∞. This feature is highly desirable for computational purposes. Applying the form in (6.10) all the scattering events between the impurity and the host atoms are taken into account, however, the changes in the host atoms around the impurity are excluded. In order to overcome this problem one has to investigate a cluster of atoms which can contain an arbitrary large number host atoms besides the impurities.

6.2 The τ-matrix for N Embedded Atoms

In the following a finite *duster* is defined as a geometrical arrangement of a set of scatterers. As shown in Fig. (6.1) it is important to emphasize that a cluster can contain, the investigated impurity atoms, some sites from the host material, for which one can study the changes caused by the impurities (like induced magnetization in a non-magnetic host), or even empty spheres which can contain also some electron density. Let C denote the set of the position vectors pointing to sites in the cluster,

$$\mathrm{C} = \{\mathbf{R}_{j_i}\}, \quad i = 1, \ldots, N \quad , \tag{6.11}$$

where N is the number of sites in the cluster and ji are the labels of these sites. It is also meaningful to introduce a set which only contains the site-indices,

$$C_N = \{ji| \quad \mathbf{R}_{j_i} \in \mathcal{C}, \quad i = 1, \ldots, N\} \quad . \tag{6.12}$$

A cluster of N scatterers embedded into a layered system, can be decomposed into "*sub-clusters*"$(\mathcal{C}_p)$ overlapping with different layers $(\mathcal{L}_p)$,

$$\mathcal{C}_p = \mathcal{L}_p \cap \mathcal{C} = \{\mathbf{R}_i | \mathbf{R}_i \in \mathcal{L}_p \quad \text{and} \quad \mathbf{R}_i \text{ e } \mathcal{C}\} \quad , \tag{6.13}$$

where $\mathcal{L}_p$ refers to the set of position vectors in a layer labeled by p and the corresponding set of indices can be defined as

$$C_p = L_p \text{ n } C_N = \{j_i | \mathbf{R}_{j_i} \in \mathcal{L}_p \quad \text{and} \quad \mathbf{R}_{j_i} \text{ e } \mathcal{C}\} \quad . \tag{6.14}$$

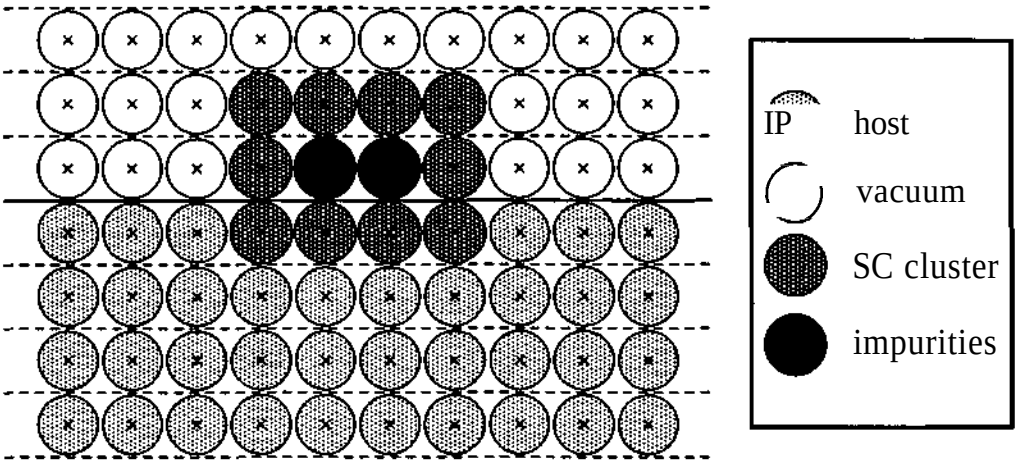

Figure 6.1: Schematic view of an embedded cluster on a surface. The cluster, which is in the present context a group of atomic sites, contains two impurities, several atoms from the supporting host surface and several vacuum spheres.

If N_p is the number of sites in $\mathcal{C}_p$, obviously,

$$\sum_p N_p = N \quad . \tag{6.15}$$

For a finite cluster, there is only a finite subset of $\mathcal{C}_p$ that $\mathcal{C}_p \neq 0$, where 0 stands for the empty set. Therefore, it makes sense to define the following layer indices,

$$p_{min(max)} = \min\,(\max)\,\{p \quad | \mathcal{C}_p \neq 0\} \quad . \tag{6.16}$$

For latter purposes, the notation for the complementary set of C can be introduced

$$\mathcal{S} \equiv \left\{ \bigcup_{p=-\infty}^{\infty} \mathcal{L}_p \setminus \mathcal{C}_p \right\} \quad , \tag{6.17}$$

where S can be interpreted as the substrate which surrounds the cluster and is assumed not to be affected by the embedded impurities.

The definition of $\Delta \mathbf{t}(z)^{-1}$ in Eq. (6.6) can be extended for N sites as

$$\Delta \underline{t}^i(z)^{-1} = \begin{cases} 0 & \text{if } i \notin \mathcal{C}_N \\ \underline{t}^i_{host}(z)^{-1} - \underline{t}^i_{imp}(z)^{-1} & \text{if } i \in \mathcal{C}_N \end{cases} \tag{6.18}$$

or,

$$\left\{\Delta \mathbf{t}(z)^{-1}\right\}_{ij} = \sum_{n \in \mathcal{C}_N} \left(\underline{t}^n_{host}(z)^{-1} - \underline{t}^n_{imp}(z)^{-1}\right) \delta_{in}\delta_{ij} \quad , \tag{6.19}$$

which can be visualized as an ∞ x ∞ matrix with N non-zero diagonal blocks,

$$\Delta \mathbf{t}^{-1} = \begin{pmatrix} \ddots & \ddots & & & & & & \\ \ddots & 0 & 0 & & & & & \\ & 0 & \underline{t}_{host}^{i_1,-1} - \underline{t}_{imp}^{i_1,-1} & 0 & & & & \\ & & 0 & \ddots & \ddots & & & \\ & & & \ddots & \underline{t}_{host}^{i_N,-1} - \underline{t}_{imp}^{i_N,-1} & 0 & \ddots & \\ & & & & 0 & 0 & & \\ & & & & & \ddots & \ddots & \end{pmatrix} . \tag{6.20}$$

Inserting Eq. (6.19) into Eq. (6.8) one finds

$$\underline{\tau}^{ij}(z) = \underline{\tau}_{host}^{ij}(z) + \sum_{k \in C_N} \underline{\tau}_{host}^{ik}(z) \Delta \underline{t}^{k}(z)^{-1} \underline{\tau}_{host}^{kj}(z) + \sum_{l,m \in C_N} \underline{\tau}_{host}^{il}(z) \Delta \underline{t}^{l}(z)^{-1} \underline{\tau}_{host}^{lm}(z) \Delta \underline{t}^{m}(z)^{-1} \underline{\tau}_{host}^{mj}(z) + \ldots \quad . \tag{6.21}$$

It is now useful to establish a notation for matrices restricted only to the cluster-sites, such as for the difference of the inverse t-matrices,

$$\left\{ \Delta \mathbf{t}^{\mathcal{C}}(z)^{-1} \right\}_{ij} \equiv \left[\underline{t}_{host}^{i}(z)^{-1} - \underline{t}^{i}(z)^{-1} \right] \delta_{ij} \qquad i,j \in C_N \tag{6.22}$$

for the τ-matrix of the host,

$$\boldsymbol{\tau}_{host}^{\mathcal{C}}(z) \equiv \left\{ \underline{\tau}_{host}^{ij}(z) \right\} \qquad i,j \in C_N \tag{6.23}$$

and of the perturbed system (cluster),

$$\boldsymbol{\tau}^{\mathcal{C}}(z) \equiv \left\{ \underline{\tau}^{ij}(z) \right\} \qquad i,j \in C_N \quad . \tag{6.24}$$

Eqs. (6.21), (6.22) (6.23) and (6.24) thus immediately imply,

$$\boldsymbol{\tau}^{\mathcal{C}}(z) = \boldsymbol{\tau}_{host}^{\mathcal{C}}(z) \left[\mathbf{I} + \Delta \mathbf{t}^{\mathcal{C}}(z)^{-1} \boldsymbol{\tau}_{host}^{\mathcal{C}}(z) + \Delta \mathbf{t}^{\mathcal{C}}(z)^{-1} \boldsymbol{\tau}_{host}^{\mathcal{C}}(z) \Delta \mathbf{t}^{\mathcal{C}}(z)^{-1} \boldsymbol{\tau}_{host}^{\mathcal{C}}(z) + \ldots \right] \tag{6.25}$$

or, compactly,

$$\boldsymbol{\tau}^{\mathcal{C}}(z) = \boldsymbol{\tau}_{host}^{\mathcal{C}}(z) \left[\mathbf{I}_{N \times N} - \Delta \mathbf{t}^{\mathcal{C}}(z)^{-1} \boldsymbol{\tau}_{host}^{\mathcal{C}}(z) \right]^{-1} \quad , \tag{6.26}$$

which is a particular application of the expression Eq. (4.4). For the present purpose, namely to study local physical properties of impurities embedded into a host material, one only needs to calculate the diagonal blocks of the $\boldsymbol{\tau}^C$ matrix in order to evaluate the local Green function according to Eq. (3.98),

$$G(z,\mathbf{r}_i,\mathbf{r}_i) = \sum_{Q,Q'} \Big[Z^i_Q(z,\mathbf{r}_i)\tau^{C,ii}_{QQ'}(z)Z^{it}_{Q'}(z,\mathbf{r}_i) - \\ - \delta_{QQ'}\Big(\theta(r_i - r_i)Z^i_Q(z,\mathbf{r}_i)I^{it}_{Q'}(z,\mathbf{r}_i) + \theta(r_i - r_i)Z^i_Q(z,\mathbf{r}_i)I^{it}_{Q'}(z,\mathbf{r}_i)\Big)\Big] \quad , \tag{6.27}$$

where the scattering solutions correspond to the particular potentials of sites within the cluster.

6.3 Self-consistent Calculation for a Cluster

Due to the non-linearity of the Kohn-Sham or the Kohn-Sham-Dirac equation one should use an iterative method to find its solution. A self-consistent calculation usually follows the scheme,

$$V^{(0)} \to \boldsymbol{\tau}^{(0)} \to V^{(1)} \to \boldsymbol{\tau}^{(1)} \to \ldots \to V^{(n)} \to \boldsymbol{\tau}^{(n)} \to V^{(n+1)} \to \ldots \tag{6.28}$$

where $\boldsymbol{\tau}^{(i)}$ ($V^{(i)}$) is the SPO matrix (potential) after the ith iterative step. As it was mentioned in chapter 2, in the LSDA approach the potential is determined exclusively by the charge- and magnetization densities (see Eqs. (3.24) and (3.26)). A self-consistent potential or charge density in a solid can be obtained as a fix-point of the iterative method,

$$\lim_{n\to\infty} V^{(n)}(\mathrm{r}) = V(\mathrm{r}) \quad , \tag{6.29}$$

$$\lim_{n\to\infty} \rho^{(n)}(\mathrm{r}) = p(\mathrm{r}) \quad , \tag{6.30}$$

which also implies for the SPO,

$$\lim_{n\to\infty} \boldsymbol{\tau}^{(n)}(z) = \boldsymbol{\tau}(z) \quad . \tag{6.31}$$

However, the standard iteration process which is sketched at (6.28) can diverge due to increasing charge oscillations in the forthcoming iterational steps [Dederichs and

Zeller, 1983]. In order to avoid this, the output from some of the previous iterations is "mixed" with that of the last one and used as an input for the next iteration,

$$V_{in}^{(n+1)}(\mathbf{r}) = V_{in}^{(n)}(\mathbf{r}) + \sum_{j=1}^{m} \mathrm{ft}\left(V_{out}^{(n-j)}(\mathbf{r}) - V_{out}^{(n)}(\mathbf{r})\right) \quad , \tag{6.32}$$

where $V_{in}^{(i)}$ is the input potential of the ith step, $V_{out}^{(i)}$ is the corresponding output potential, m is an arbitrarily chosen integer and β_m is a weighting (mixing) factor for the previous output potentials. There are various *potential mixing* schemes the complexities of which can be different due to the different choice of m and the method of the optimizing ft (e.g. simple-mixing: m = 1 and ft arbitrary; Anderson mixing [Dederichs and Zeller, 1983]: m = 1 and ft is determined by a least-square deviation process). In the present calculations the so-called *modified Broyden mixing* as proposed by Johnson [Johnson, 1988] is used. It should be noted that the mixing procedure can be performed equivalently for the charge and spin densities.

6.4 Approximations of the Inversion of the τ-matrix

With a little modification of Eq. (6.26) the SPO in the nth self-consistent step is given by,

$$\boldsymbol{\tau}^{C,(n)}(z) = \left[\boldsymbol{\tau}_{host}^{C}(z)^{-1} - \mathbf{t}_{host}^{C}(z)^{-1} + \mathbf{t}^{C,(n)}(z)^{-1}\right]^{-1} \quad . \tag{6-33}$$

Combining the above equation for the $(n-1)$th and nth steps, one can easily derive, that

$$\boldsymbol{\tau}^{C,(n)}(z) = \boldsymbol{\tau}^{C,(n-1)}(z) \left[\mathbf{t}^{C,(n-1)}(z)^{-1} - \mathbf{t}^{C,(n)}(z)^{-1} + \boldsymbol{\tau}^{C,(n-1)}(z)\right]^{-1} \quad , \tag{6.34}$$

which is of similar form as (6.26) and shows that the previous self-consistent step can serve as a reference for the embedding process. Close to the self-consistent solution the following criterion is fulfilled (dropping the C indices).

$$\lim_{n\to\infty} \left\| (\mathbf{t}^{(n-1)}(z)^{-1} - \mathbf{t}^{(n)}(z)^{-1}) \right\| \to 0 \quad \forall z \quad , \tag{6.35}$$

or, alternatively,

$$\left\| (\mathbf{t}^{(n-1)}(z)^{-1} - \mathbf{t}^{(n)}(z)^{-1}) \boldsymbol{\tau}^{(n-1)}(z) \right\| \ll 1 \quad \forall z \quad . \tag{6.36}$$

In this case one can expand Eq. (6.34),

$$\begin{aligned}\boldsymbol{\tau}^{(n)}(z) \cong \boldsymbol{\tau}^{(n-1)}(z) + \\ \boldsymbol{\tau}^{(n-1)}(z)\left(\mathbf{t}^{(n-1)}(z)^{-1} - \mathbf{t}^{(n)}(z)^{-1}\right)\boldsymbol{\tau}^{(n-1)}(z) + \\ \boldsymbol{\tau}^{(n-1)}(z)\left(\mathbf{t}^{(n-1)}(z)^{-1} - \mathbf{t}^{(n)}(z)^{-1}\right) \times \\ \boldsymbol{\tau}^{(n-1)}(z)\left(\mathbf{t}^{(n-1)}(z)^{-1} - \mathbf{t}^{(n)}(z)^{-1}\right)\boldsymbol{\tau}^{(n-1)}(z) + \ldots \quad . \end{aligned} \tag{6.37}$$

This implies that the matrix inversion (6.34) can be estimated up to an arbitrary order. For example up to first order it can be written as

$$\begin{aligned}\underline{\tau}^{ij,(n),\mathrm{I}}(z) \cong \underline{\tau}^{ij,(n-1)}(z) + \\ \sum_{k=1}^{N} \tau^{ik,(n-1)}(z)\left(\underline{t}^{k,(n-1)}(z)^{-1} - \underline{t}^{k,(n)}(z)^{-1}\right)\underline{\tau}^{kj,(n-1)}(z) \quad , \end{aligned} \tag{6.38}$$

or, using the super-matrix notation,

$$\boldsymbol{\tau}^{(n),\mathrm{I}}(z) \cong \boldsymbol{\tau}^{(n-1)}(z) + \boldsymbol{\tau}^{(n-1)}\left(\mathbf{t}^{(n-1)}(z)^{-1} - \mathbf{t}^{(n)}(z)^{-1}\right)\boldsymbol{\tau}^{(n-1)}(z) \quad , \tag{6.39}$$

while the kth order approach can be obtained from the algorithm,

$$\boldsymbol{\tau}^{(n),0}(z) = \boldsymbol{\tau}^{(n-1)}(z) \quad , \tag{6.40}$$

$$\boldsymbol{\tau}^{(n),k}(z) = \boldsymbol{\tau}^{(n),k-1}(z) + \boldsymbol{\tau}^{(n),k-1}(z)\left[\mathbf{t}^{(n-1)}(z)^{-1} - \mathbf{t}^{(n)}(z)^{-1}\right]\boldsymbol{\tau}^{(n-1)}(z) \quad . \tag{6.41}$$

This formulation is especially useful to reduce the computational time in the case when the calculation is started near a known self-consistent solution. An example for this situation can be when the orientation of the magnetization is updated during the iterations and subsequent orientations differ from each other by only a few degree. This is the case in spin-dynamics calculations which enable one to study non-collinear magnetic configurations in nanostructures.

Chapter 7

Electrostatic potential for an embedded cluster

For a given potential, V_{eff}(r) one can calculate the charge- and magnetization density of a solid which within the framework of LSDA (see Chapter 2) determines the V_{xc}(r) and B_{xc} (r) parts of the potential. In order to update $V_{eff}(r)$ within a self-consistent calculation one has to calculate also the electrostatic (Hartree) potential of the system. The solution of the Poisson equation for an embedded cluster consists basically of two steps, similar to the calculation of the Green function. First, one has to solve the Poisson equation for the unperturbed host and then for the cluster with the boundary conditions set by the host. In this section a detailed description of treatment of the electrostatic potential for a finite embedded cluster will be given.

7.1 Basic Definitions

The electrostatic potential of a charge distribution $p(r)$ confined to a finite domain Ω can be written as

$$V(\mathbf{r}) = 2 \int_a d^3r' \frac{\rho(\mathbf{r}')}{|\mathbf{r} - \mathbf{r}'|} \quad , \qquad (7.1)$$

where the boundary condition $V(\mathbf{r}) \to 0$ in the limit of r $\to \infty$ has been chosen. A well-known solution of the above equation relies on the *multipole expansion* [Landau and Lifshitz, 1997] which is based on the expansion of $\frac{1}{|\mathbf{r}-\mathbf{r}'|}$ in the case of |r'| < |r|

(outside Ω),

$$\frac{1}{|\mathbf{r}-\mathbf{r}'|} = 4\pi \sum_{(=0}^{\infty} \sum_{m=-l}^{l} \frac{Y_{lm}^*(\hat{\mathbf{r}})Y_{lm}(\hat{\mathbf{r}}')}{2l+1} \frac{r'^l}{r^{l+1}} \qquad (r' < r)\,, \tag{7.2}$$

where the $Y_{lm}(\hat{\mathbf{r}})$ are complex spherical harmonics and $r^{(\prime)}$ — $\mathbf{r}^{(\prime)}$. Combining Eq. (7.1) with Eq. (7.2) yields

$$V(\mathbf{r}) = 8\pi \int_a d^3r' \rho(\mathbf{r}') \sum_{lm} \frac{Y_{lm}^*(\hat{\mathbf{r}})Y_{lm}(\hat{\mathbf{r}}')}{2l+1} \frac{r'^l}{r^{l+1}} \quad . \tag{7.3}$$

Using the definition of the multipole moments of the charge-density in the finite volume fi as

$$Q^{lm} \equiv \frac{\sqrt{4\pi}}{2l+1} \int_\Omega d^3r' \rho(\mathbf{r}')(r')^l Y_{lm}(\hat{\mathbf{r}}') \tag{7.4}$$

and the multipole fields as

$$M^{lm}(\mathbf{r}) = 2\sqrt{4\pi} \frac{Y_{lm}^*(\hat{\mathbf{r}})}{r^{l+1}} \quad , \tag{7.5}$$

for r > S_Ω, S_Ω = max $\{r'|\mathbf{r}' \in$ fi$\}$ one can write the Coulomb potential in a compact expression as

$$V(\mathbf{r}) = \sum_{lm} Q^{lm} M^{lm}(\mathbf{r}) \quad . \tag{7.6}$$

7.2 Electrostatic Potential of a Lattice

For ordered lattices a real-space vector can be decomposed as

$$\mathrm{r} = \mathbf{R}_i + \mathbf{r}_i \quad , \tag{7.7}$$

where $\mathbf{R}_i$ points to the center of the cell i and $\mathbf{r}_i$ is inside the particular cell. The electrostatic potential at cell i,

$$V_i(\mathbf{r}_i) \equiv V(\mathbf{R}_i + \mathbf{r}_i) \quad (\mathbf{r} \in \Omega_i) \quad , \tag{7.8}$$

can be split up into intra-cell and inter-cell parts,

$$V_i(\mathbf{r}_i) = V_i^{intra}(\mathbf{r}_i) + V_i^{inter}(\mathbf{r}_i) \quad , \tag{7.9}$$

arising from the charge density within and outside the particular cell, respectively. Within the ASA the intra cell part is given by [MacLaren et al., 1989]

$$V_i^{intra}(r) = -\frac{Z_i}{r} + \frac{4\pi}{r}\int_0^r (r')^2 \rho_i(r')\,dr' + 4\pi \int_r^{S_i^{ASA}} r'\rho_i(r')\,dr' \quad , \tag{7.10}$$

where Zi is the nuclear charge at site i and S_i^{ASA} is the radius of ASA sphere around $\mathbf{R}_i$. Obviously the method of calculation of $V_i^{intra}(\mathbf{r}_i)$ does not depend on the geometrical arrangement of the lattice positions. Therefore, as what follows the evaluation of $V_i^{inter}(\mathbf{r}_i)$ for layered systems and embedded clusters is described.

The inter-cell part of the electrostatic potential, which for matters of simplicity will be denoted by $V_i(\mathbf{r}_i)$, can be expressed as

$$V_i(\mathbf{r}_i) = 2\sum_{j(\neq i)}\int_{\Omega_j} d\mathbf{r}'_j \frac{\rho_j(\mathbf{r}'_j)}{|\mathbf{r}_i + \mathbf{R}_i - \mathbf{r}'_j - \mathbf{R}_j|} \quad , \tag{7.11}$$

where the summation runs over all cells in the solid but the one labeled by i and $\rho_j(\mathbf{r}'_j)$ is the charge density in cell j. Applying for $|\mathbf{r}'_j| < |\mathbf{r}_i + \mathbf{R}_i - \mathbf{R}_j|$ the expansion in Eq. (7.2) one obtains,

$$V_i(\mathbf{r}_i) = \sum_{j(\neq i)}\sum_{lm} \frac{8\pi}{2l+1}\frac{Y^*_{lm}(\mathbf{r}_i + \widehat{\mathbf{R}_i - \mathbf{R}_j})}{|\mathbf{r}_i + \mathbf{R}_i - \mathbf{R}_j|^{l+1}} \int_{\Omega_j} d\mathbf{r}'_j \rho(\mathbf{r}'_j) r'^l_j Y_{lm}(\hat{\mathbf{r}}'_j) \quad . \tag{7.12}$$

Similarly to Eq. (7.6) one can write,

$$V_i(\mathbf{r}_i) = \sum_{j(\neq i)}\sum_{lm} M^{lm}(\mathbf{r}_i - \mathbf{R}_i - \mathbf{R}_j) Q_j^{lm} \quad , \tag{7.13}$$

in terms of the definition of the charge density moments (7.4),

$$Q_j^{lm} \equiv \frac{\sqrt{4\pi}}{2l+1}\int_{\Omega_j} d\mathbf{r}'_j \rho_j(\mathbf{r}'_j)(r'_j)^l Y_{lm}(\hat{\mathbf{r}}'_j) \quad , \tag{7.14}$$

and the multipole field (7.5),

$$M^{lm}(\mathbf{r}_i + \mathbf{R}_i - \mathbf{R}_j) = 2\sqrt{4\pi}\frac{Y^*_{lm}(\mathbf{r}_i + \widehat{\mathbf{R}_i - \mathbf{R}_j})}{|\mathbf{r}_i + \mathbf{R}_i - \mathbf{R}_j|^{l+1}} \quad . \tag{7.15}$$

If the relation $|\mathbf{r}_i| < |\mathbf{R}_i - \mathbf{R}_j|$ is fulfilled one can apply again an expansion for $M^{lm}(\mathbf{r}_i + \mathbf{R}_i - \mathbf{R}_j)$ separating the dependence on Rj - $\mathbf{R}_j$ and $\mathbf{r}_i$ as

$$M^{lm}(\mathbf{r}_i + \mathbf{R}_i - \mathbf{R}_j) = \sum_{l'm'} A_{ij}^{lm,l'm'} r_i^{l'} Y_{l'm'}^*(\hat{\mathbf{r}}_i) \quad , \tag{7.16}$$

where the *real-space Madelung constants* were introduced as

$$\begin{aligned} A_{ij}^{lm,l'm'} &\equiv A^{lm,l'm'}(\mathbf{R}_i - \mathbf{R}_j) \\ &\equiv 2\sqrt{4\pi}(-1)^{l'} \frac{4\pi[2(l+l')-1]!!}{(2l-1)!!(2l'+1)!!} \times \\ &\quad g_{lm,(l+l')(m'-m)}^{l'm'} \frac{1}{|\mathbf{R}_i - \mathbf{R}_j|^{l+l'+1}} Y_{(l+l')(m'-m)}(\widehat{\mathbf{R}_i - \mathbf{R}_j}) \end{aligned} \tag{7.17}$$

with $g_{lm,l''m''}^{l'm'}$ are the Gaunt coefficients (3.88). Care has to be taken, however, since the conditions $|\mathbf{r}_j'| < |\mathbf{r}_i + \mathbf{R}_i - \mathbf{R}_j|$ and $|\mathbf{r}_i| < |\mathbf{R}_i - \mathbf{R}_j|$ are fulfilled for adjacent cells only if non-overlapping spherical domains, i.e., muffin-tins are considered. As shown in Ref. [Zabloudil, 2000] and references therein, for space-filling cells a particular technique using an auxiliary displacement vector has to be used to calculate the inter-cell potential between neighboring cells. As the electrostatic potential is taken to be spherically symmetric within the ASA, only the $A^{lm,00}$ term has to be considered

$$M_{ij}^{lm} \equiv A_{ij}^{lm,00} = 2\sqrt{4\pi} \frac{Y_{lm}^*(\widehat{\mathbf{R}_i - \mathbf{R}_j})}{|\mathbf{R}_i - \mathbf{R}_j|^{l+1}} \quad . \tag{7.18}$$

Similar to Eq. (7.6) the intercell part of the electrostatic potential which is independent from $\mathbf{r}_i$ according to (7.18) can be written in the ASA as

$$V_i(\mathbf{r}_i) = V_i = \sum_{j(\neq i)} \sum_{lm} M_{ij}^{lm} Q_j^{lm} \quad . \tag{7.19}$$

For further purposes it is useful to introduce the quantities,

$$V_{ij} \equiv \sum_{lm} M_{ij}^{lm} Q_j^{lm} \quad , \tag{7.20}$$

which stand for the contribution of cells *j* to the electrostatic potential in cell *i*.

7.3 Electrostatic Potential in a Layered System

The 2D translation invariance of a layered system implies that multipole moments are equivalent in all cells in a particular layer. Therefore, it is useful to introduce

the notation Q_q^{lm} for the uniform multipole moments in layer q. Furthermore, introducing the notation

$$M_{pi,qj}^{lm} = A^{lm,00}(\mathbf{c}_p + \mathbf{T}_i - \mathbf{c}_p - \mathbf{T}_j) \quad ,$$

the uniform Madelung potential at a site within layer p can be written as

$$V_p \equiv \sum_q \sum_{j \in L_q}{}' \sum_{lm} M_{p0,qj}^{lm} Q_q^{lm} \tag{7.21}$$

where the index q runs over all the layers and j labels sites in layer q. Note that for $q = p$, the case $j = 0$ is excluded from the summation as it is indicated by $\sum'$. Due to the symmetry of simple surfaces the most important contributions to (7.21) arise from the monopole and dipole moments, Q_p^{00} and Q_p^{10}. Thus one has to evaluate the corresponding two coefficients,

$$M_{pq}^{00} \equiv \sum_{j \in L_q}{}' M_{p0,qj}^{00} \quad \text{and} \quad M_{pq}^{01} \equiv \sum_{j \in L_q}{}' M_{p0,qj}^{10} \quad . \tag{7.22}$$

Inspecting the explicit form of the spherical harmonics, from Eq. (7.5) it turns out that

$$M^{10}(\mathbf{r}) = -\frac{g}{\partial r_\perp} M^{00}(\mathbf{r}) \quad , \tag{7.23}$$

where the position vector r is split up as $\mathrm{r} = (\mathbf{r}_\parallel, r_\perp)$. Due to the $|\mathbf{R}_i - \mathbf{R}_j|^{-(l+1)}$ factor in M_{ij}^{lm}, the sums in Eq. (7.22) converge extremely slowly with increasing distance. In order to avoid this problem an approximate solution of the 2D Ewald problem is required [Szunyogh et al., 1994b]. For point-like charges arranged in a two-dimensional lattice it can be shown that for $p \neq q$ [Szunyogh et al., 1994b]

$$M_{pq}^{00} = \frac{4\pi}{\Omega} \sum_{G_\parallel \neq 0} \frac{\cos(\mathbf{G}_\parallel \mathbf{r}_\parallel)}{|\mathbf{G}_\parallel|} e^{-|\mathbf{G}_\parallel||(\mathbf{c}_p - \mathbf{c}_q)_\parallel|} \quad , \tag{7.24}$$

where $\mathbf{G}_\parallel$ refers to the reciprocal lattice vectors of the 2D lattice and the $\mathbf{c}_p = (\mathbf{c}_{p\parallel}, c_{p\perp})$. The contribution coming from sites in one and the same layer $(p = q)$ can be obtained as

$$M_{pp}^{00} = -\frac{8\sigma\sqrt{\pi}}{\Omega} + \frac{4\pi}{\Omega} \sum_{G_\parallel \neq 0} \frac{\mathrm{erfc}(|\mathbf{G}_\parallel \sigma)}{|\mathbf{G}_\parallel|} +$$

$$\sum_{\mathbf{T}_i \neq 0} \frac{2}{|\mathbf{T}_i|} \mathrm{erfc}\left(\frac{|\mathbf{T}_i|}{2\sigma}\right) + \frac{2}{\sigma\sqrt{\pi}} \tag{7.25}$$

where erfc is the error function,

$$\mathrm{erfc}(z) = 1 - \frac{2}{\sqrt{\pi}} \int_0^x e^{-t^2} \mathrm{d}t \quad , \tag{7.26}$$

and a is the Ewald-parameter. The Madelung constant for the dipoles can be evaluated by combining Eqs. (7.23) and (7.24),

$$M_{pq}^{10} = \frac{4\pi}{\Omega} \left[1 + \mathrm{sign}\left((\mathbf{c}_p - \mathbf{c}_q)_\perp\right) \sum_{\mathbf{G}_\parallel \neq 0} e^{-\left(|(\mathbf{c}_p - \mathbf{c}_q)_\perp||\mathbf{G}_\parallel|\right)} \cos\left(- \left| \mathbf{G}_\parallel (\mathbf{c}_p - \mathbf{c}_q)_\parallel \right| \right) \right] \quad . \tag{7.27}$$

The $G_\parallel = 0$ contribution can be obtained solving the one-dimensional Poisson equation,

$$\frac{d^2}{dr_\perp^2} V_\perp(r_\perp) = -8\pi \rho_\perp(r_\perp) \quad , \tag{7.28}$$

where $\rho_\perp(r_\perp)$ is given by [Szunyogh et al., 1994b)

$$\rho_\perp(r_\perp) = \sum_p Q_p^{00} \delta(r_\perp - c_{p,\perp}) \quad . \tag{7.29}$$

Eq. (7.28) can easily be solved to yield

$$V_\perp(r_\perp) = -\frac{4\pi}{\Omega} \sum_p Q_p^{00} |r_\perp - c_{p,\perp}| + A r_\perp - B \quad , \tag{7.30}$$

where the constants A and B have to be used to satisfy different boundary conditions. For the closest layer of the left-hand side medium to the interface ($p = 0$) (see the definition at Eq. (5.11))

$$V_\perp(c_{0,\perp}) \doteq V^L \quad , \tag{7.31}$$

where V^L is the Madelung potential of the left-hand side bulk (for simple lattices $V^L = 0$). For the right-hand side, two distinct boundary condition can be specified one for the interface case and an other for the surface case. For an interface it is given by

$$V_\perp(c_{N+1,\perp}) \doteq V^R \quad , \tag{7.32}$$

with V^R being the Madelung potential on the right-hand side bulk, while for a surface, one has to ensure that the potential is constant sufficiently deep in the vacuum region

$$\frac{d}{dr_\perp} V_\perp (c_{N+1,\perp}) = 0 \quad , \tag{7.33}$$

which, in fact, implies charge neutrality of a metal surface. Taking the boundary conditions into account, for an interface containing N layers, $V_{\perp,p}$ can be written as

$$V^{int}_{\perp,p} = \frac{4\pi}{\Omega} \sum_{9=1}^{N} Q_q^{00} \left[-2 \min (c_{p\perp}, c_{q\perp}) + 2\frac{c_{q\perp} c_{p\perp}}{c_{N+1,\perp}} \right] +$$
$$\frac{4\pi}{\Omega} \sum_{q=1}^{N} Q_q^{10} \left[1 + (1 - \delta_{p,q}) \text{sign} (c_p - c_q)_1 - 2\frac{c_{p,\perp}}{c_{N+1,\perp}} \right] +$$
$$\frac{(V^R - V^L)}{c_{N+1,\perp}} + V^L \tag{7.34}$$

where the first term is the contribution of the monopole moment and the second is that of the dipoles. For a surface this yields

$$V^{surf}_{\perp,p} = \frac{8\pi}{\Omega} \sum_{q=1}^{N} Q_q^{00} \min (c_p, c_q)_\perp +$$
$$\frac{4\pi}{\Omega} \sum_{9=1}^{N} Q_q^{10} \left[1 + \text{sign} (c_p - c_q)_\perp \right] + V^L \quad , \tag{7.35}$$

and the vacuum potential level can be calculated as

$$V^{vac} = V^{surf}_\perp (c_{N+1,\perp}) = \frac{8\pi}{\Omega} \sum_{9=1}^{N} (Q_q^{00} c_{q,\perp} + Q_q^{10}) + V^L \quad .$$

7.4 Electrostatic Potential in a Cluster

Due to the additivity of the Poisson equation, the inter-cell potential in a given cell can be decomposed into contributions of atoms inside and outside of the cluster, V_i^C and V_i^S, respectively as

$$V_i = V_i^C + V_i^S \quad , \tag{7.36}$$

with

$$V_i^C \equiv \sum_{j \in C_N \setminus \{i\}} V_{ij} \tag{7.37}$$

and

$$V_i^S = \sum_{j \notin C_N} V_{ij} \quad . \tag{7.38}$$

In the following, the assumption is made that outside the embedded cluster the system has the same physical properties as the perfect 2D translational invariant host, i.e., the atoms in S are not disturbed by the cluster C. This implies that V_i^S has to be independent of the type of the atoms inside the cluster, that is,

$$V_i^S = V_i' - V_i^{C\prime} \quad , \tag{7.39}$$

where V_i' and $V_i^{C\prime}$ correspond to a cluster of atoms other than the host atoms. In particular, if atoms identical to those in the host are embedded, the 2D translationally invariant system is recovered. Using this property, one can calculate V_i^S as

$$V_i^S = \bar{V}_p - \bar{V}_i^C \qquad (i \in C_p) \quad , \tag{7.40}$$

where $\bar{V}_p$ is the electrostatic potential of the cells in layer p in the unperturbed host and $\bar{V}_i^C$ is the potential arising from host atoms placed at the cluster positions.

The above assumption also fixes the boundary condition of the Poisson equation, since the electrostatic potential within the cluster has to join smoothly the electrostatic potential of the surrounding host. For a site at the border of the cluster this immediately implies that

$$V? = \bar{V}_i^C \quad . \tag{7.41}$$

This property can be fulfilled only approximately by including a sufficiently large number of the host atoms in the cluster.

In practice, Eq. (7.40) can be evaluated as follows

$$V_i^S = \bar{V}_p^{l_{max}} - \sum_{lm}^{(l_{max})} \sum_{q=p_{min}}^{p_{max}} \bar{Q}_q^{lm} \sum_{j \in C_q}{}' M_{pi,qj}^{lm} \quad (i \in C_p) \quad , \tag{7.42}$$

where the multipole expansion for the 2D translational invariant system has been performed up to l_{max} and the $\bar{Q}_q^{lm}$ denote the moments of the charge densities of the host layers.

One is only left with the task to calculate V_i^C in Eq. (7.36)

$$V_i^C = \sum_{lm}^{(l'_{max})} \sum_{q=p_{min}}^{p_{max}} \sum_{j\in C_q}{}' M_{pi,qj}^{lm} Q_j^{lm} \quad (i \in C_p) \tag{7.43}$$

where Q_j^{lm} refer now to the perturbed cells. Putting Eqs. (7.36), (7.42) and (7.43) together one ends up with

$$V_i^C \quad \bar{W}_p^{l_{max}} - \sum_{\mathbf{lm}}^{(\mathbf{lmax})} \sum_{q=p_{min}}^{\mathbf{Pmax}} \bar{Q}_q^{lm} \sum_{j\in C_q}{}' M_{pi,qj}^{lm} + \sum_{lm}^{(l'_{max})} \sum_{q=p_{min}}^{\mathbf{Pmax}} \sum_{j\in C_q}{}' M_{pi,qj}^{lm} Q_j^{lm} \quad . \tag{7.44}$$

It should be noted, that the highest order of the Madelung expansion for the 2D translational invariant system and for the cluster, l_{max} and l'_{max}, respectively, not necessarily have to be the same.

For an energy-resolved representation $V(\mathbf{r})$ can be written as

$$V(\mathbf{r}) = \int_{E_B}^{E_F} dE \sum_{lm} Q^{lm}(E) M^{lm}(\mathbf{r}) \quad , \tag{7.45}$$

where

$$Q^{lm}(E) = \frac{\sqrt{4\pi}}{2l+1} \int_{\mathrm{n}} \mathrm{d}^3 r' \rho(E, \mathbf{r}') r'^l Y_{lm}(\hat{\mathbf{r}}') \quad , \tag{7.46}$$

and $p(E, \mathrm{r}')$ is the energy resolved charge density. In terms of the Green function (3.29) this corresponds to

$$Q^{lm}(E) = \frac{\sqrt{4\pi}}{2l+1} \left(-\frac{1}{\pi}\right) \int_{\mathrm{n}} \mathrm{d}^3 r' \, \mathrm{Im} \left\{ G^+(E, \mathbf{r}', \mathbf{r}') \right\} r'^l Y_{lm}(\hat{\mathbf{r}}') \quad . \tag{7.47}$$

This expression can be re-written also as a complex contour-integration in the upper semi-plane as follows

$$V(\mathbf{r}) = -\frac{1}{\pi} \int^{f} \mathrm{d}z \left\{ \sum_{lm} Q^{lm}(z) M^{lm}(\mathbf{r}) \right\} \tag{7.48}$$

where $Q^{lm}(z)$ is the complex extension of the definition in Eq. (7.47).

Chapter 8

The Magnetic Anisotropy Energy

In ferromagnetic solids there are preferred directions of the magnetization. This property is known as *magnetic anisotropy.* In non-relativistic quantum mechanics the energy of a system is independent of the direction of the magnetization. Relativistic corrections, spin-orbit coupling and the magnetic dipole-dipole interaction, to the Hamiltonian break the rotational invariance with respect to the spin quantization axis. The ground state energy depends on the direction of the spontaneous magnetization relative to the crystalline axis, called the *magneto-crystalline anisotropy,* and on the shape of the sample, referred to as the *shape anisotropy.* The origin of the shape anisotropy is the magnetic dipole-dipole interaction, while the magneto-crystalline anisotropy arises essentially from the spin-orbit interaction, but also to lesser extent, from the magnetic dipole-dipole interaction [Bruno, 1993].

The magnetic anisotropy energy (MAE) is defined as the difference of the ground state energy, E_{gs}, between two different orientations of the spontaneous magnetization, $\hat{M}_0$

$$\mathrm{MAE} = E_{gs}(\hat{M}_0^1) - E_{gs}(\hat{M}_0^2) \quad . \tag{8.1}$$

The earliest attempts to understand the phenomenon of magnetic anisotropy in iron, cobalt and nickel go back to Van Vleck [Vleck, 1937]. In his approach the magnetic moments were considered to be localized on the atoms. Van Vleck found that, although it is almost quenched, the orbital moment influences the MAE. Later on, Brooks [Brooks, 1940] and Fletcher [Fletcher, 1954] used an itinerant electron model to explain the MAE and the quenching of orbital moments in cubic crystals. By using an electron gas model, Bloch *et al.* [Bloch and Gentile, 1931] came up with

the same conclusion as Van Vleck.

Due to time reversal symmetry, the free energy has to remain unchanged if $\hat{M}_0$ is replaced by $-\hat{M}_0$. Expanding therefore the free energy in terms of direction-cosines $\hat{\mathrm{MO}} = (\alpha_1, \alpha_2, \alpha_3)$, only even powers of the corresponding components can occur

$$F(\hat{M}_0) = F_0 + \sum_{i,j} b_{ij}\alpha_i\alpha_j + \sum_{i,j,k,l} b_{ijkl}\alpha_i\alpha_j\alpha_k\alpha_l + \ldots \quad , \tag{8.2}$$

Furthermore, the crystalline symmetry imposes some restrictions, which reduce the number of independent parameters. In a cubic system the usual expression for the anisotropy energy can be written as

$$F(\hat{M}_0) = K_0 + K_1(\alpha_1^2\alpha_2^2 + \alpha_2^2\alpha_3^2 + \alpha_3^2\alpha_1^2) + K_2\alpha_1^2\alpha_2^2\alpha_3^2 + \ldots \quad , \tag{8.3}$$

where $K\backslash$ and K_2 are the *anisotropy constants* for the fourth and sixth order term. respectively. In most cases, the fourth order term dominates the MAE of cubic crystals.

A surface has a lower point group symmetry than the bulk, therefore, as noticed first by Neel [Neel, 1954], in the expansion of the MAE with respect to the direction cosines, contributions of lower order appear. For uniaxial systems, such as thin films with four-fold rotational symmetry axis (z) the corresponding expansion reads:

$$F(\hat{M}_0) = K_0 + K_1(\alpha_1^2 + \alpha_2^2) + K_2(\alpha_1^2 + \alpha_2^2)^2 + K_2'\alpha_1^2\alpha_2^2 + \ldots \quad , \tag{8.4}$$

where now K_1 is a second order, while K_2 and K_2' are fourth-order parameters. Expressing the direction-cosines by spherical coordinates $(\vartheta, \varphi), \alpha_1 = \sin\vartheta\cos\varphi$ and $\alpha_2 = \sin fl \sin\varphi$, one gets the following angle dependence for the energy

$$F(\vartheta, \varphi) = K_0 + K_1\sin^2\vartheta + K_2\sin^4\vartheta + \frac{1}{4}K_2'\sin^4\vartheta\sin^2(2\varphi) + \ldots \quad . \tag{8,5}$$

8.1 The Magnetic Force Theorem

The total energy per atom is of the order of a few 10 000 eV/atom. Therefore, an accuracy of about 10^{-11} - 10^{-8} is needed, if one wants to calculate the MAE from total energy which is a very demanding task. By using the so-called *magnetic Force Theorem* [Jansen, 1988], the anisotropy energy can be obtained as the difference between the sum of the eigenvalues of the Dirac equation for different magnetic

configurations, which is of the order of 10 eV. This treatment requires much less computational efforts for a same numerical accuracy.

Assuming that the spin moment points along the direction $\hat{M}_0$ the total energy functional can then be written as

$$E[n(\mathbf{r}),m(\mathbf{r}),\hat{M}_0] = T^s[n(\mathbf{r}),m(\mathbf{r}),\hat{M}_0] + V_H[n(\mathbf{r})]+ E_{xc}[n(\mathbf{r}),m(\mathbf{r})] + \int v_{ext}(\mathbf{r})n(\mathbf{r})d^3r \quad . \tag{8.6}$$

At the self-consistent solution for the charge- and magnetic density, $n_{sc}(\mathbf{r})$ and $m_{sc}(\mathbf{r})$, every term depending on $\hat{M}_0$ is included by the non-interacting kinetic energy, T^s given by

$$\begin{aligned} T^s &= \sum_{occ} \int d^3r \bar{\psi}_n(\mathbf{r}) \left(\frac{\hbar c}{i}\alpha\nabla + \beta mc^2 \right) \psi_n(\mathbf{r}) \\ &= \sum_{occ} \int d^3r \bar{\psi}_n(\mathbf{r}) \left(\varepsilon_n - ev^s(\mathbf{r}) - \mu_B B_{xc}(\mathbf{r}) \hat{M}_0 \beta\Sigma \right) \psi_n(\mathbf{r}) \quad , \end{aligned} \tag{8.7}$$

where the $\psi_n(\mathbf{r})$ are solutions of the Kohn-Sham-Dirac equation (2.29) corresponding to energy eigenvalues ε_n and the sum runs over the occupied electron states. At self-consistency the first variation of the total energy functional with the respect to the density and the spin-density has to vanish by definition,

$$\frac{\delta E}{\delta n} = \frac{\delta T^s}{\delta n} + \frac{\delta V_H}{\delta n} + \frac{\delta E_{xc}}{\delta n} + v_{ext} = 0 \quad , \tag{8.8}$$

and

$$\frac{\delta E}{\delta m} = \frac{\delta T^s}{\delta m} + \frac{\delta E_{xc}}{\delta m} = 0 \quad . \tag{8.9}$$

The variation of the total energy functional can be written as follows

$$\Delta E = \frac{\delta E}{\delta n}\Delta n + \frac{\delta E}{\delta m}\Delta m + \frac{\partial E}{\partial \hat{M}_0}\Delta \hat{M}_0 \quad . \tag{8.10}$$

Since at the self-consistent solution the first two terms vanish the orientation dependence of the ground-state energy is given by

$$\frac{dE_{gs}}{d\hat{M}_0} = \frac{\partial E}{\partial \hat{M}_0} = \frac{\partial T^s}{\partial \hat{M}_0} \quad . \tag{8.11}$$

As can be seen from Eq. (8.11) within the framework of LSDA in the vicinity of the self-consistent solution, the ground state energy depends on MÔ, exclusively through the non-interacting kinetic energy. Eq. (8.7) can be formally rewritten as

$$T^s = \sum_{occ} \epsilon_n - \int t\, \mathrm{d}^3 r v^s(\mathbf{r}) n_{sc}(\mathbf{r}) - 2\mu_B \int \mathrm{d}^3 r B^{eff}(\mathbf{r}) \hat{M}_0 \mathbf{m}(\mathbf{r}) \quad , \tag{8.12}$$

which gives in turn the form for the variation of the non-interacting kinetic energy,

$$\Delta T^s = \mathrm{A} \sum_{occ} \mathrm{en} - \mathrm{d}^3 r v^s(\mathbf{r}) \Delta n_{sc}(\mathbf{r}) - 2\mu_B \int_J \mathrm{d}^3 r B^{eff}(\mathbf{r}) \hat{M}_0 \Delta \mathbf{m}(\mathbf{r}) \quad . \tag{8.13}$$

It is useful to write also the general variation of AT with respect to MÔ

$$\Delta T^s = \frac{\delta T^s}{\delta n} \Delta n + \frac{\delta T^s}{dm} \mathrm{Am} + \frac{\partial T^s}{\partial \hat{M}_0} \hat{\Delta} M_0 \, , \tag{8.14}$$

where one has to include the changes in the charge and spin densities due to the change of the direction of magnetization.

On the other hand, from Eq. (8.11), varying the total energy, the dependence of T^s on $\hat{M}_0$ can be expressed as

$$\Delta T^s = - \int \mathrm{d}^3 r v^s(\mathbf{r}) \Delta n_{sc}(\mathbf{r}) - 2\mu_B \int_J^f \mathrm{d}^3 r B^{eff}(\mathbf{r}) \hat{M}_0 \Delta \mathbf{m}(\mathbf{r}) + \frac{\partial T^s}{\partial \hat{M}_0} \Delta M_0 \quad . \tag{8.15}$$

Comparing the two expressions for $\Delta T^s[n_{sc}, m_{sc}, \hat{M}_0]$ in Eqs. (8.13) and (8.15) one can find

$$\frac{\partial T^s}{\partial \hat{M}_0} = \frac{\partial}{\partial \hat{M}_0} \sum_{occ} \epsilon_n \quad . \tag{8.16}$$

Combining Eqs. (8.11) and (8.16) one obtains that the dependence of ground-state energy on the direction of magnetization can be associated with the explicit dependence of the single-particle energies,

$$\frac{\partial E_{gs}}{\partial \hat{M}_0} = \frac{\partial}{\partial \hat{M}_0} \sum_{occ.} \epsilon_k \quad . \tag{8.17}$$

Although the Force Theorem is valid in the above differential form only for a self-consistent solution and for a magnetization pointing along a (high-symmetry) crystal

axis, it is often used it in its integral form to take the difference between the energies with respect to two distinct directions of the magnetization,

$$\mathrm{MAE} = \sum_{occ.} \varepsilon_k \Big|_{\hat{M}_0^1} - \sum_{occ.} \varepsilon_k \Big|_{\hat{M}_0^2} \quad . \tag{8.18}$$

The validity of this approach has been proven by the success of many previous calculations by Daalderop *et al.* [Daalderop et al., 1990] and Szunyogh *et al.* [Szunyogh et al., 1995; Üjfalussy et al., 1996b]. By definition, only the explicit dependence of the Hamiltonian on $\hat{M}_0$ has to be considered in Eq. (8.18). In other words, the potentials and effective fields are assumed to be the same for the two orientations *(frozen-potential approximation)*. As the charges and spin-moments do not change significantly with respect to $\hat{M}_0$, this seems to cause only small errors in $V(r)$ and $B_{xc}(r)$. In contrary, the orbital moments, undergo a relatively big change with respect to $\hat{M}_0$.

Actually the MAE is calculated in two steps. First, a self consistent calculation for a given direction of the magnetization is performed. Then only one iteration to calculate the single-particle energy using the potential is made, which is obtained from the self-consistent calculation. Without self-consistency one can not recover a given number of charges. Therefore, instead of the sum of the one-particle energies, the grand canonical potential (in the present context usually called band energy) has to be used, which can be written at $T = OK$ as

$$E_{band}^{\mathcal{C}}(\hat{M}_0) = \int_{\varepsilon_B}^{\varepsilon_F} (\varepsilon - \varepsilon_F) n^{\mathcal{C}}(\varepsilon, \hat{M}_0) d\varepsilon \quad , \tag{8.19}$$

where ε_B stands for the bottom of the valence band and $n^{\mathcal{C}}(\epsilon, \hat{\mathrm{MO}})$ denotes the DOS of the cluster with orientation $\hat{\mathrm{MO}}$, which obviously can be decomposed into DOS's corresponding to specific sites,

$$n^{\mathcal{C}}(\varepsilon, \hat{M}_0) = \sum_{i \in C_N} n_i(\varepsilon, \hat{M}_0) \quad - \tag{8.20}$$

Therefore the MAE of the cluster,

$$\Delta E_{\hat{M}_0^1 - \hat{M}_0^2}^{\mathcal{C}} \equiv E_{band}^{\mathcal{C}}(\hat{M}_0^1) - E_{band}^{\mathcal{C}}(\hat{M}_0^2) \quad , \tag{8.21}$$

can also be split into atomlike contributions,

$$\Delta E^{\mathcal{C}}_{\hat{M}_0^1 - \hat{M}_0^2} = \mathop{\mathbf{E}}_{i \in C_N} \Delta E^{i}_{\hat{M}_0^1 - \hat{M}_0^2} = \sum_{i \in C_N} E^{i}_{band}(\hat{M}_0^1) - E^{i}_{band}(\hat{M}_0^2) \ . \tag{8.22}$$

This decomposition often helps to analyze the results obtained for a given system. The preferred direction of the magnetization can be read off from the following conditions

$$\Delta E^{\mathcal{C}}_{\hat{M}_0^1 - \hat{M}_0^2} < 0 \quad \rightarrow \hat{M}_0^1 \text{ is preferred,} \tag{8.23}$$

$$\Delta E^{\mathcal{C}}_{\hat{M}_0^1 - \hat{M}_0^2} > 0 \quad \rightarrow \hat{\mathrm{MO}} \text{ is preferred.} \tag{8.24}$$

As for small system it is of less importance, in here the magnetic dipole-dipole energy part to MAE is not calculated.

Chapter 9

Fe, Co and Ni adclusters on Ag(OOl)

9.1 Introduction

In the present chapter selected, planar Fe, Co and Ni adclusters deposited on a fcc Ag(OOl) surface are investigated as a first application of the newly developed computational code for the KKR embedding technique described in chapter 6, taking special attention to the convergence of the magnetic properties of impurities with respect to the number of host atoms contained by the self-consistently treated cluster. The magnetic adatoms occupy sites in the first vacuum layer referring to positions of an ideal fcc parent lattice with the experimental Ag lattice constant (4.12 Å). In each case three different orientations for the magnetization were considered: along the *z* axis (normal to planes), as well as along the *x* and *y* axes (nearest neighbor directions in an fcc(OOl) plane). The results are compared to corresponding overlayer values and former cluster calculations.

The embedding technique based on the Korringa-Kohn-Rostoker Green's function method in the local spin-density approximation (LSDA) has been applied for more than two decades to the magnetism of transition metal adatoms and clusters embedded into bulk hosts [Podloucky et al., 1980; Zeller et al., 1980| or deposited on surfaces [Lang et al., 1994; Wildberger et al., 1995|. The main feature of this approach is that the interaction between adatoms and host surface atoms can be analyzed within *first principles* electronic structure calculations [Stepanyuk et al., 1996a,b|, in several cases exhibiting novel phenomena in nanomagnetism such as the existence of meta-magnetic states [Stepanyuk et al., 1997a,b| or intermixing effects between adatoms and the host surface [Stepanyuk et al.. 1999|. An accurate calcu-

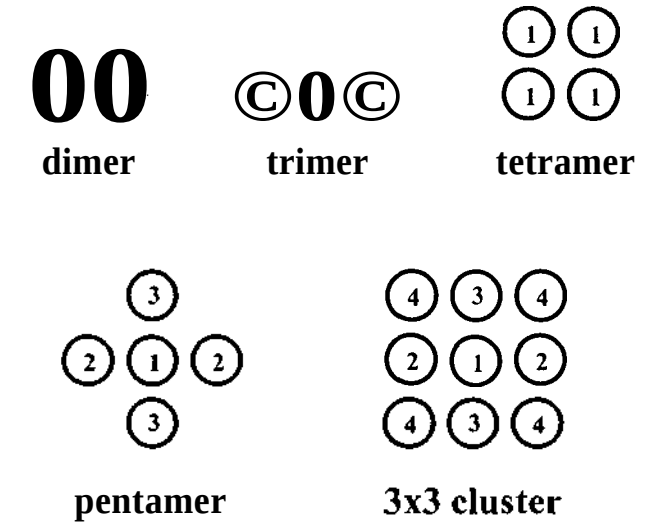

Figure 9.1: Sketch of the planar clusters considered. For an orientation of the magnetization along the *x* or *y* axis, the equivalent atoms in a cluster are labeled by the same number.

lation of the total energy in terms of full potential or full charge density schemes made possible investigations of the energetics of adatoms [Nonas et al., 1998; Levanov et al., 2000; Stepanyuk and Hergert, 2000]. As compared to TB methods an obvious drawback of the embedded KKR technique is that with respect to computational limitations the number of the atoms in the cluster is restricted to about less than 100. Furthermore, the inclusion of structural relaxations is exceedingly difficult. In order to circumvent these problems, a quasi-ab initio molecular-dynamics method can be employed by parameterizing interatomic potentials to the first principles KKR Green's function electronic structures [Izquierdo et al., 2001]. On the level of a fully relativistic spin-polarized electron theory, recently, strongly enhanced orbital magnetism and MAE of adatoms and small clusters on Ag and Au(OOl) surfaces have been reported [Nonas et al., 2001; Cabria et al., 2002].

9.2 Results

9.2.1 Spin and Orbital Moments

As shown in Fig. 9.1, dimers and linear trimers oriented along the *x* axis were considered, square-like tetramers, centered pentamers (as in Ref. [Cabria et al., 2002|), as well as a cluster arranged on positions of a 3x3 square denoted in the following simply as 3x3 cluster. In Fig. 9.1, for each particular cluster the equivalent atoms with respect to an orientation of the magnetization along the *x* or *y* axis are labeled by the same number. Note that for a magnetization aligned in the *z* direction, the atoms labeled by 2 and 3 in the pentamer and the 3x3 cluster become equivalent. Up to a total of 67 sites, the clusters consisted of adatoms, several substrate Ag atoms and empty sites from neighboring shells. A stability test of the local electronic and magnetic properties for a single Fe adatorn with respect to the number of self–consistently treated neighboring shells is shown in Fig. 9.2. Although the calculated orbital moment of the Fe adatom shows a somewhat slower convergence than the valence charge and the spin moment, it is remarkable that considering only a first shell of neighbors this already yields values which differ by less than 1% from the fully converged ones.

Calculations for different orientations of the magnetization revealed that the spin moments are fairly insensitive to the direction of the magnetization, while for the orbital moments remarkably large anisotropy effects apply, a phenomenon that will be discussed in the next section. For a magnetization along the *z* axis, the calculated values of the spin and orbital moments for an adatom and selected clusters of Fe, Co and Ni on Ag(OOl) are listed in Table 9.1. In there the position indices in a particular cluster refer to the corresponding numbers in Fig. 9.1 and the number of nearest neighbors of magnetic atoms (coordination number, n_c) is also given.

As compared to the corresponding monolayer values (3.15 μ_B for Fe and 2.03 μ_B for Co), the spin moment of a single adatom of Fe (3.39 μ_B) and Co (2.10 μ_B) is slightly increased. In the case of Fe clusters, the spin moments decrease monotonously with increasing n_c. A slight deviation from that behavior can be seen for the 3x3 cluster, where the atoms with n_c = 2 and 3 exhibit the same spin moment. As can be seen in Figs. 9.3 and 9.4 for the central atom of the pentamer and, in particular, of the 3x3 cluster, the value of the spin moment of the corresponding monolayer is

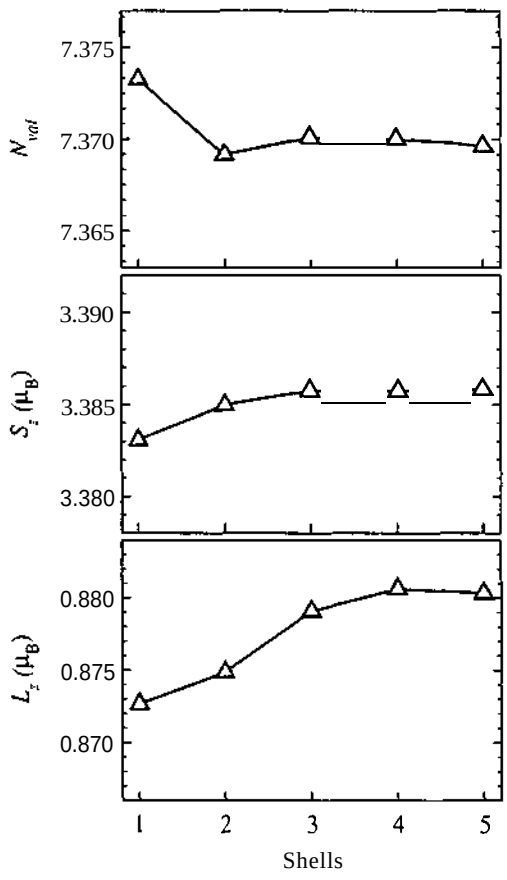

Figure 9.2: Calculated number of valence electrons (N_{val}), spin moment (S_z) and orbital moment (L_z) of a single Fe adatom on a Ag(OOl) surface as a function of the number of the self-consistently treated atomic shells around the Fe atom.

practically achieved for Fe and Co while for Ni one can find in Fig. 9.5 the values are close for the monolayer ones already for the trimers, however, the tendency with increasing number of impurities is less clear. The above results for Fe compare fairly well to those of Cabria *et al.* [Cabria et al., 2002] and reflect a very short ranged magnetic correlation between the Fe atoms.

The general tendency of decreasing spin moments with increasing n_c is obvious also for the Co clusters up to the pentamer case. For the 3x3 cluster, however, just the opposite trend applies. Establishing a correlation between S_z and n_c for Co seems to be more ambiguous than for Fe, because the changes of the spin moment are much smaller in this case. Nevertheless, it is tempting to say that in the formation

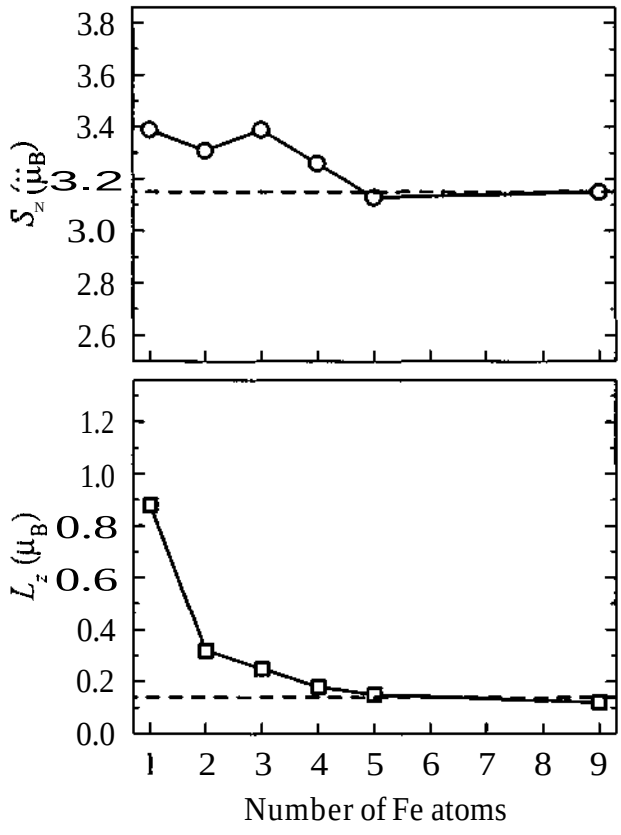

Figure 9.3: Calculated spin (S_z) and orbital moments (L_z) of the most symmetric Fe atom in Fe_n (n = 1, 2, 3, 4, 5, 9) clusters on Ag(OOl) surface with a magnetization pointing normal to the surface. For comparison, the spin and orbital moments of the corresponding monolayer (Fe|Ag(001)) is marked by dashes.

of the magnetic moment of Co, further off neighbors play a more significant role than in the case of Fe.

In the case of an adatom and dimer of Ni no stable magnetic state was found. Quite contradictory, Cabria *et al.* [Cabria et al., 2002] reported a spin moment of about 0.5 μ_B for a Ni adatom on Ag(OOl). As the computational method of these authors is very similar to the present one, it is at present not quite clear what causes this discrepancy between the two calculations. One possible reason for differences between the two calculations can be that Cabria et al. [Cabria et al., 2002] used an angular momentum cut-off of ℓ_{max} = 3, whereas in here ℓ_{max} = 2 is used. Within the ASA, however, a monotonous convergence with respect to ℓ_{max} is not obvious at

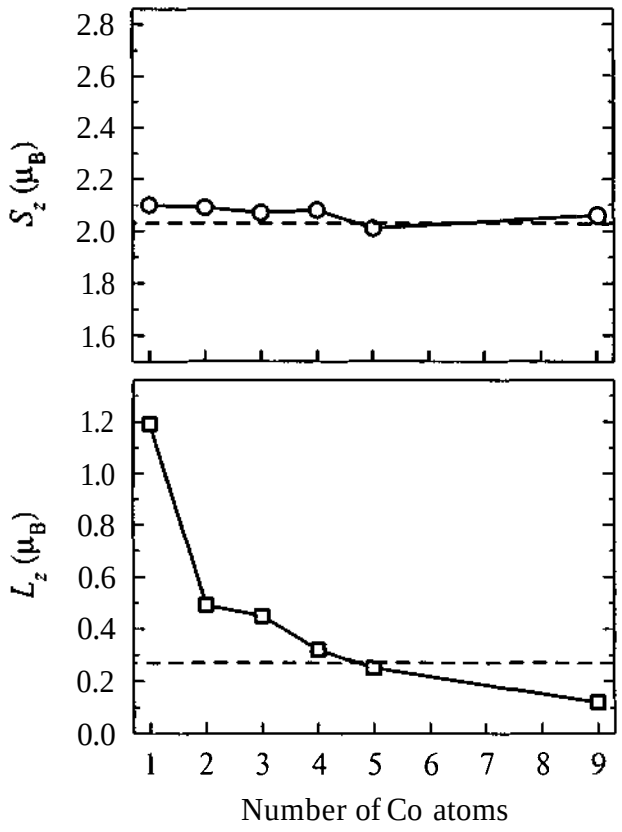

Figure 9.4: Calculated spin (S_z) and orbital moments (L_z) of the most symmetric Co atom in Co_n $(n = 1, 2, 3, 4, 5, 9)$ clusters on Ag(OOl) surface with a magnetization pointing normal to the surface. For comparison, the spin and orbital moments of the corresponding monolayer (Co Ag(001)) is marked by dashes.

all. Furthermore, it should be noted that, the present result clearly is in line with the experiments of Beckmann and Bergmann who found no magnetic moment for Ni adatoms on a Au surface [Beckmann and Bergmann, 1996], which as a substrate is rather similar to Ag. It should be noted, however, that in Ref. [Beckmann and Bergmann, 1996] the actual surface orientation is not specified.

For clusters of Ni one can observe an opposite tendency as for Fe and Co: the spin moment enhances with increasing number of neighbors. This clearly can be seen from Table 9.1. Having in mind the calculated monolayer value (0.71 μ_B), small cluster calculations indicate a fairly slow evolution of the spin moment of Ni with increasing cluster size, implying that the magnetism of Ni is subject to

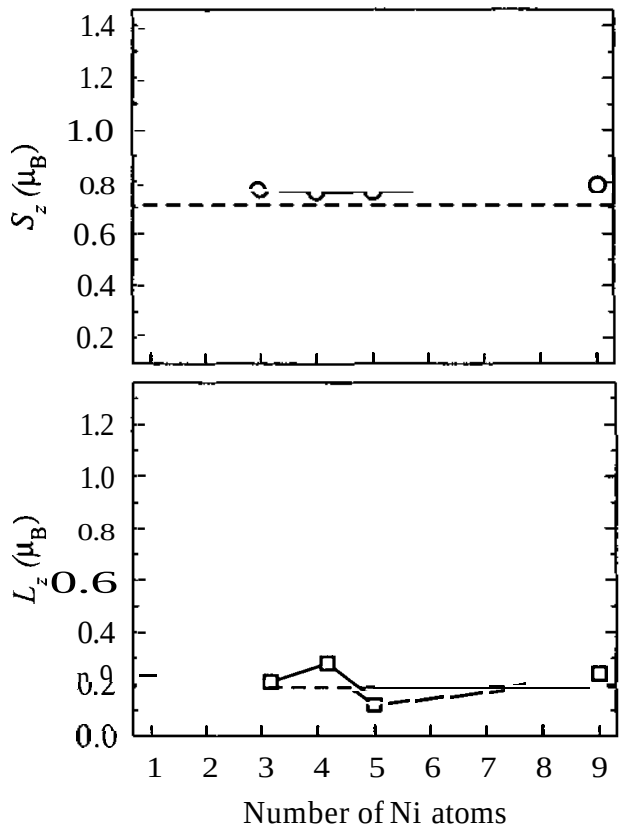

Figure 9.5: Calculated spin (S_z) and orbital moments (L_z) of the most symmetric Ni atom in Ni_n $(n — 3, 4, 5, 9)$ clusters on Ag(OOl) surface with a magnetization pointing normal to the surface. For comparison, the spin and orbital moments of the corresponding monolayer (Ni|Ag(001)) is marked by dashes.

correlation effects on a much longer scale than in Fe or Co according to real-space KKR calculations for bulk fcc Ni [Beiden et al., 1998; Petit et al., 2000|.

Apparently, the orbital moments show a different, in fact, more complex behavior as the spin moments. For single adatoms of Fe and Co orbital moments enhanced by a factor of $\sim$ 6 and ~ 4.5, respectively, as compared to the monolayer values (0.14 μ_B for Fe and 0.27 μ_B for Co) were found. This is a direct consequence of the reduced coordination number and crystal field splitting, being relatively large in monolayers, and, in particular, in corresponding bulk systems [Bruno, 1993|. In spite of a qualitative agreement, the L_z values for the adatoms are considerably larger than those calculated by Cabria *et al.* [Cabria et al., 2002| (0.55 μ_B for Fe and 0.76 μ_B

for Co). It should be noted, however, that by including orbital polarization effects (Hund's second rule) in terms of Brooks' parameterization [Brooks, 1985; Ebert and Battocletti, 1996], Nonas *et al.* [Nonas et al., 2001] found orbital moments for Fe and Co adatoms on Ag(OOl) close to the atomic limit (2.20 μ_B for Fe and 2.57 μ_B for Co).

For dimers of Fe and Co, the value of L_z drops to about 40% in magnitude as compared to a single adatom. The evolution of the orbital moment seems, however, to decrease explicitly only for the central atom of larger clusters. It was shown by Szunyogh *et al.* [Szunyogh et al., 1997] that the (local) symmetry can be correlated with the magnetic anisotropy, i.e., with the quenching effect of the crystal field experienced by an atom. The central atom of the linear trimers, pentamers and the 3×3 clusters exhibit well-defined rotational symmetry, namely, C_2, C_4 and C_4, respectively. The corresponding values of L_z, namely, 0.25 μ_B, 0.15 μ_B, and 0.12 μ_B for Fe, and 0.49 μ_B, 0.25 μ_B and 0.23 μ_B for Co, nicely reflect the increasing rotational symmetry and coordination numbers of the respective atoms. Although the outer magnetic atoms exhibit systematically larger orbital moments than the central ones, even a qualitative correlation with the local environment (n_c) can hardly be stated. The orbital moment for the trimer of Ni is already close to the monolayer value (0.19 μ_B) but shows rather big fluctuations with respect to the size of the cluster and also to the positions of the individual atoms.

9.2.2 Magnetic Anisotropy

By using the self-consistent potentials for a given orientation of the magnetization (along z), magnetic anisotropy energies are calculated by means of the magnetic force theorem (see section 8.1) as differences of band-energies.

The anisotropies of the orbital moments and the contributions of the individual magnetic atoms to the MAE are displayed in Tables 9.2, 9.3 and 9.4 for Fe, Co and Ni clusters, respectively. In addition, the total MAE per magnetic atoms of the clusters including the neighborhood is also given. Although the dominating contributions to the MAE arise from the magnetic species, the environment, in particular, the Ag atoms and the empty sites within the first shell add a remarkable amount to the MAE. However, due to the weak polarization of the Ag atoms, a fast convergence of the total MAE with respect to the size of the cluster (environment) was obtained.

As can be inferred from the corresponding positive values of the MAE in Tables 9.2 and 9.3, single adatoms of Fe and Co exhibit a magnetization oriented perpendicular to the surface. This again is in perfect agreement with the experiments of Beckmann and Bergmann [Beckmann and Bergmann, 1996]. As compared with the monolayer case (0.47 meV), the MAE of an Fe adatom (5.61 meV) is enhanced by a factor of twelve. Contrary to the present results, Cabria *et al.* [Cabria et al., 2002) predicted in-plane magnetism (ΔE_{x-z} — −0.98 meV) for an Fe adatom on Ag(OOl), and perpendicular magnetism for Co, albeit with a much larger anisotropy energy (> 7 meV) than the present one (4.36 meV). It should be noted that Cabria *et al.* [Cabria et al., 2002] employed the so-called Lloyd's formula, for details, see Ref. [Weinberger, 1990], for calculating the MAE, claiming that it is essential for an accurate evaluation of the effects of perturbed host atoms. As was mentioned above, for the present case of a Ag substrate the direct evaluation of the MAE (see Eqs. (8.19) to (8.22)) provides well-converged results for the MAE. It should also be stressed at this point, that the present calculations are consistent with a qualitative rule, valid for transition metals with a more than half-filled *d*–band and based on simple, perturbative phenomenological or tight-binding reasoning [Bruno, 1993]: the direction, along which the orbital moment is the largest, is energetically favored.

As can be seen from Table 9.2, perpendicular magnetism is characteristic for all Fe clusters considered. For the dimer and the trimer one observes a small in-plane anisotropy with preference of the *x* axis, i.e., in the direction of the Fe-Fe bonds. In agreement with the reduction of the orbital moment, as discussed in the previous section, the contribution of the central atom to the MAE for the trimer, the pentamer and the 3×3 cluster rapidly decreases, being even less than the monolayer value in the case of the 3x3 cluster. The outer atoms in the pentamer and in the 3×3 cluster can add considerably more to the MAE than the central atom. As a consequence, the average MAE strongly fluctuates with increasing size of the magnetic cluster and shows a very slow tendency to converge to the MAE of an Fe monolayer on Ag(OOl). Such a complicated behavior of the MAE with respect to the cluster size has also been found by Guirado–López [Guirado-López, 2001] for free-standing fcc transition metal clusters.

In comparison to an adatom, for a Co dimer ΔE_{x-z} drops to a large negative value (-3.49 meV/per Co), while ΔE_{y-z} remains slightly positive (0.76 meV/per

Co), implying that a Co dimer favors the x (in-plane) direction of the magnetization and also experiences a strong in-plane anisotropy. The strong tendency of Co clusters to an in-plane magnetization pertains for larger clusters and is characteristic also for a Co monolayer ($\Delta E_{x-z} = -1.31$ meV). The atom-like resolution of the MAE indicates, that this tendency is driven by nearest-neighbor Co-Co interactions. An explanation of this effect in terms of perturbation theory and symmetry resolved densities of states can be found in Refs. [Wang et al., 1994; Zhong et al.. 1996; Üjfalussy et al., 1996a]. As an unexpected consequence, the contribution to the MAE of the central atom in the cluster can be larger than that of some outer atoms. Quite obviously, the MAE of the central atom of the trimer, the pentamer and the 3x3 cluster, -9.06 meV, -2.46 meV, and -1.86 meV, respectively, fall monotonously off to the monolayer value, whereas the average MAE possesses a much more complicated evolution also in this case.

With exception of the tetramer, for which a MAE close to zero was found, all Ni clusters prefer an in-plane magnetization. The in-plane anisotropy, seen from Table 9.4 for the trimer, but also from the atom-like contributions for the larger clusters, is, however, smaller than in the case of Co. Again the complicated nature of the magnetism of Ni shows up, in particular, for the 3x3 cluster: while the contribution of the central atom to the MAE almost vanishes, those of the outer atoms oscillate in magnitude. Considering the MAE of a Ni monolayer on Ag(OOl) (-2.23 meV), no straightforward connection with the magnetic anisotropy properties of small clusters can be traced.

9.2.3 Magnetic Interaction between Adatoms

Interactions between magnetic nanoclusters are of great importance for technological applications. Clearly enough the most important questions are *(i)* what is the magnetic structure of the individual entities, *(ii)* of what nature (strength, range, etc.) is the coupling between them, and *(iii)* what influences the magnetic orientation of these entities relative to each other. In this section a preliminary study in this field is presented by investigating the interaction of two Fe or Co adatoms on Ag(OOl).

First self-consistent calculations for two adatoms by varying the distance d between them from a to $5a$ along the x direction were performed, where a is the 2D

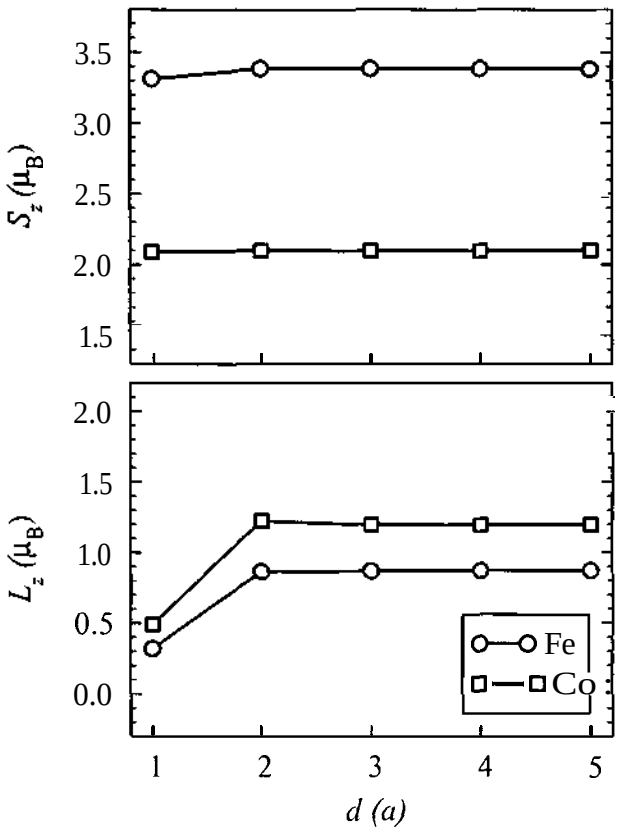

Figure 9.6: Calculated spin and orbital moments of two adatoms of Fe or Co on Ag(OOl) as a function of their distance d measured in units of the 2D lattice constant a.

lattice constant and keeping the orientation "of the magnetizations parallel to each other (along the z axis). The calculated spin and orbital moments of the (coupled) adatoms are shown in Fig. 9.6. Note that the distance a refers to the bondlength in dimers. As can be seen from Fig. 9.6, both for Fe and Co the values of S_z and L_z rapidly converge to the respective single adatom value.

Next the exchange-coupling energy, ΔE_X, between the two adatoms was calculated by taking the energy difference between a parallel ($\uparrow\uparrow$) and an antiparallel ($\uparrow\downarrow$) orientation of the two adatoms,

$$\Delta E_X = E^c_{band}(\uparrow\uparrow) - E^c_{band}(\uparrow\downarrow) \quad , \tag{9.1}$$

using, however, the self-consistent potentials for the parallel configuration.

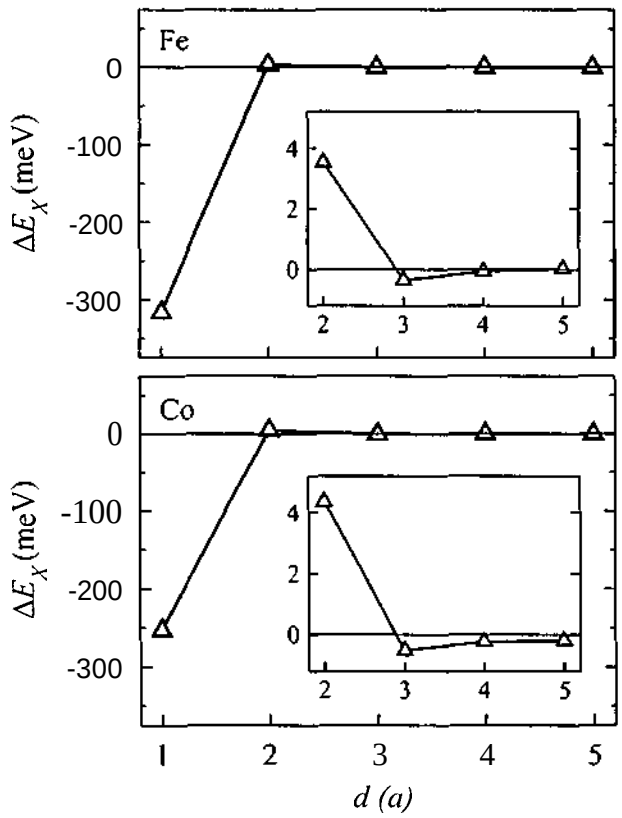

Figure 9.7: Calculated exchange coupling energy, ΔE_X, between two adatoms of Fe or Co on Ag(OOl) as a function of the distance d measured in units of the 2D lattice constant a. The insets show the range $2a < d < 5a$ on a blown up scale.

The calculated ΔE_X is shown in Fig. 9.7 for Fe and Co as a function of the distance d between the two adatoms. Apparently, for $d = a$ in both cases a strong, ferromagnetic nearest-neighbor exchange-coupling between these two atoms applies, with an interaction energy somewhat larger for Fe than for Co. As the two adatoms are adjacent in this case, this strong coupling can be attributed to a direct exchange mechanism. Increasing the separation between the two adatoms, ΔE_X rapidly decreases. For $d = 2a$ it changes sign, i.e., the coupling becomes antiferromagnetic. Since for an antiparallel alignment of the spin moments of the two adatoms, lying close to each other, the electronic structure and the magnetic moments might be expected to differ to some extent as compared to a parallel configuration, the corresponding values of S_z and L_z in Table 9.6 can be questioned. Therefore, for this

particular case self-consistent calculations were performed also for the antiparallel alignment. Assuringly, for both Fe and Co, the same value of S_z and L_z within 1% relative accuracy were obtained as in the case of a parallel alignment. For larger distances ferromagnetic coupling can be observed, which virtually vanishes for $d > 5a$. implying a very weak, short ranged exchange interaction between the adatoms of Fe and Co induced by the Ag host.

Table 9.1: Calculated spin moments (S_z) and orbital moments (L_z), in units of μ_B, for small clusters of Fe, Co and Ni on Ag(OOl) with magnetization perpendicular to the surface *(z)*. For each position in a particular cluster (see Fig. 9.1), n_c refers to the number of the neighboring magnetic (Fe, Co, Ni) atoms.

Cluster	position	n_c	Fe		Co		Ni	
			S_z	L_z	S_z	L_z	S_z	L_z
adatom		0	3.39	0.88	2.10	1.19	–	–
dimer	1	1	3.31	0.32	2.09	0.49	–	–
trimer	1	2	3.29	0.25	2.07	0.45	0.77	0.21
	2	1	3.33	0.44	2.06	0.49	0.70	0.23
tetramer	1	2	3.26	0.18	2.08	0.32	0.76	0.28
pentamer	1	4	3.13	0.15	2.01	0.25	0.76	0.12
	2	1	3.35	0.37	2.10	0.59	0.71	0.33
	3	1	3.35	0.37	2.10	0.59	0.71	0.33
3x3 cluster	1	4	3.15	0.12	2.06	0.23	0.79	0.24
	2	3	3.23	0.16	2.04	0.30	0.71	0.20
	3	3	3.23	0.16	2.04	0.30	0.71	0.20
	4	2	3.23	0.33	2.00	0.29	0.63	0.19

Table 9.2: Calculated orbital moment anisotropies (ΔL), in units of μ_B, and contributions of the Fe atoms to the MAE, ΔE, in units of meV, for small clusters of Fe on Ag(OOl). For each cluster, the total MAE per Fe atom of the cluster including the neighborhood is also given in parentheses.

Cluster	position	n_c	ΔL_{x-z}	ΔE_{x-z}	ΔL_{y-z}	ΔE_{y-z}
adatom		0	-0.37	5.07	-0.37	5.07
				(5.61)		(5.61)
dimer	1	1	-0.12	2.14	-0.11	1.66
				(2.30)		(1.83)
trimer	1	2	-0.12	1.93	-0.08	0.93
	2	1	-0.16	2.83	-0.15	2.39
				(2.72)		(2.13)
tetramer	1	2	-0.02	0.50	-0.02	0.50
				(0.54)		(0.54)
pentamer	1	4	-0.03	0.49	-0.03	0.49
	2	1	-0.03	0.92	-0.08	0.85
	3	1	-0.08	0.85	-0.03	0.92
				(0.90)		(0.90)
3x3 cluster	1	4	0.00	0.23	0.00	0.23
	2	3	-0.02	0.43	-0.01	0.84
	3	3	-0.01	0.84	-0.02	0.43
	4	2	-0.13	1.86	-0.13	1.86
				(1.20)		(1.20)

Table 9.3: Calculated orbital moment anisotropies (ΔL), in units of μ_B, and contributions of the Co atoms to the MAE, ΔE, in units of meV, for small clusters of Co on Ag(OOl). For each cluster, the total MAE per Co atom of the cluster including the neighborhood is also given in parentheses.

Cluster	position	n_c	ΔL_{x-z}	ΔE_{x-z}	ΔL_{y-z}	ΔE_{y-z}
adatom		0	-0.26	4.20	-0.26	4.20
				(4.36)		(4.36)
dimer	1	1	0.15	-3.50	-0.01	0.67
				(-3.49)		(0.76)
trimer	1	2	0.40	-9.06	-0.02	-0.11
	2	1	0.34	-6.29	0.05	-0.04
				(-7.44)		(-0.01)
tetramer	1	2	0.15	-2.29	0.15	-2.29
				(-2.37)		(-2.37)
entamer	1	4	0.12	-2.46	0.12	-2.46
	2	1	0.21	-4.16	-0.01	-0.03
	3	1	-0.01	-0.03	0.21	-4.16
				(-2.22)		(-2.22)
3x3 cluster	1	4	0.13	-1.86	0.13	-1.86
	2	3	0.10	-1.56	0.18	-2.96
	3	3	0.18	-2.96	0.10	-1.56
	4	2	0.16	-2.60	0.16	-2.60
				(-2.45)		(-2.45)

Table 9.4: Calculated orbital moment anisotropies (ΔL), in units of μ_B, and contributions of the Ni atoms to the MAE, ΔE, in units of meV, for small clusters of Ni on Ag(OOl). For each cluster, the total MAE per Ni atom of the cluster including the neighborhood is also given in parentheses.

Cluster	position	n_c	ΔL_{x-z}	ΔE_{x-z}	ΔL_{y-z}	ΔE_{y-z}
trimer	1	2	0.19	-6.12	0.18	-1.38
	2	1	0.11	-3.72	0.08	-1.00
				(-4.63)		(-1.13)
tetramer	1	2	-0.05	0.07	-0.05	0.07
				(0.10)		(0.10)
pentamer	1	4	0.15	-2.26	0.15	-2.26
	2	1	0.01	-1.64	0.05	-0.69
	3	1	0.05	-0.69	0.01	-1.64
				(-1.41)		(-1.41)
3×3 cluster	1	4	-0.06	-0.02	-0.06	-0.02
	2	3	0.02	-0.75	0.06	-2.00
	3	3	0.06	-2.00	0.02	-0.75
	4	2	0.05	-1.21	0.05	-1.21
				(-1.17)		(-1.17)

Chapter 10

Finite Co chains on Pt(111)

10.1 Introduction

In this study the magnetic properties of Co_n chains of different length ($1 < n < 10$) deposited along the ($1\bar{1}0$) direction on a fcc Pt(lll) surface are investigated. The Co adatoms occupy sites in the first vacuum layer referring to positions of an ideal fcc parent lattice with the experimental Pt lattice constant (3.92 Å). For each case three different orientations for the magnetization were considered: along the *z* axis (perpendicular to the surface) as well as along the *x* and *y* axes referring to in-plane directions parallel and perpendicular to the chains, respectively. Focusing on the spin- and orbital moments as well as on the MAE in particular the cross-over between a point-like impurity (OD) and a linear chain (1D) is traced. The results are also compared to the values measured for monoatomic Co chains grown at the step-edges of Pt(997) [Gambardella et al., 2002].

The *3d*(Fe, Co, Ni)|Pt(Pd) systems as possible candidates for the high-density magneto-optical recording media attracted extended interests both experimentally and theoretically in the last decade. These systems posses strong perpendicular anisotropy, enhanced Kerr effect at small optical wavelengths and adjustable Curie temperature which are highly desirable properties from an application point of view. The appearance of the atomic-scale manipulation and the self-assembly techniques gave the opportunity to apply a new class of materials with these peculiar physical properties amplified by the changes due to the reduced coordination number of the magnetic atoms. The step decoration effect enables the production of high-density, uniform monoatomic wires on stepped surfaces. However, the self-organization tech-

niques have the drawback of limited choice of the producible patterns in contrast to other writing techniques (e-beam, scanning probe writing, *etc.)* [Gambardella et al., 2000b].

10.1.1 Growth of Atomic-Scale Structures on Pt

Grütter *et al.* [Grütter and Dürig, 1994] demonstrated that the Co atoms nucleate spatially uniformly in a quasi-layer-by-layer mode on a flat Pt(lll) surface below 300 K upto the thickness of three atomic layer and after the third layer grow in three-dimensional hcp islands. The interaction between the Pt(lll) surface and the adsorbed Co adatom induces the formation of the so-called *double-line reconstruction* of the Pt surface. The surface reconstruction arises together with the formation of *dendrites* on the surface. It was shown by Lundgren *et al.* [Lundgren et al., 1999) that these dendrites mainly consist of Pt atoms with Co and Pt atoms underneath. They suggested that the development of the dendrites are caused by the higher mobility of atoms at the end of the double-line reconstruction rows due to the increased lattice spacing.

The growing process is completely different on a vicinal Pt(997) surface (cut 6.5° off normal with respect to the (111) plane) with monoatomic steps along the $(1\bar{1}0)$ direction. The terraces between the steps are in average 20.1 Å wide ($\sim$ 8 atomic rows). As was shown [Nötzel et al., 1992; Marsico et al., 1997] the step decoration phenomena on high-index surfaces can be exploited to grow in arranged 1D arrays during an early stage of the epitaxial growth. Marsico *et al.* [Marsico et al.. 1997] found a highly periodic structure by adsorbing Xe (at 40 K) and Ag (at 350 K) atoms onto a Pt(997) surface at one ($\sim$ 0.13 ML) and two eights ($\sim$ 0.26 ML) of the coverage with respect to the first complete mono-layer [Marsico et al., 1997]. This phenomenon indicates that the adsorbed atoms grow on the terraces in a row-by-row mode. It was also shown that while the Xe atoms prefer the upper edges of the steps, the Ag atoms attach exclusively to the bottom edges similarly to most metal adsorbates [Gambardella et al., 2000a,b]: the step-edges acts as nucleation sites due to the increased coordination number and the higher adsorption energy. After the second row the row-by-row growth cannot be observed which can be caused by the increased adsorbate-adsorbate interaction instead of the step-adsorbate one.

Investigating Co|Pt systems, Gambardella *et al.* [Gambardella et al., 2000a,b]

observed step decoration effect between 150 and 500 K. At lower temperature they found that the kinetic energy of the Co atoms are not enough to migrate to the Pt steps and therefore they stick to the already adsorbed Co atoms resulting into a rough growth. Between 250 K and 300 K the Co atoms form monoatomic chains on the lower step edges when their density is 0.13 ML, similarly to the Ag case [Marsico et al., 1997]. If 300 K < T < 500 K the formation of double layers sets in and at higher temperature (500 K < T) alloying of Co and Pt starts which reverts the formation of the monoatomic wires at the step edges.

10.1.2 Aspects of Magnetism

It was shown in a recent paper by Singh [Singh, 2003] comparing scalar-relativistic and non-relativistic results for Ni-Pd and Ni-Pt alloys that the different trends of changes in the magnetic moment of the Ni atoms due the increased Pt and Pd concentration which was experimentally observed arise mainly due to relativistic effects.

Pt and Pd which are non-magnetic as pure metal can be magnetically polarized by an interaction with ferromagnetic *3d* elements (Fe, Co, Ni) as was shown by using element-sensitive XMCD measurement [Wienke et al., 1991]. In Ni|Pt multilayers the Pt layer at the interface posses relatively large magnetic moment ($\sim$0.3 μ_B) which decreases rapidly with increasing distance from the interface [Wilhelm et al., 2000]. This indicates that hybridization effects are spatially localized mainly to the *3d*|Pt interface region. Similarly, for layered $CoPt_3$ systems Grange *et al.* [Grange et al., 1998] found a relatively large magnetization in the Pt layers ($S^{Pt} \sim$ 0.2 μ_B, $L^{Pt} \sim$ 0.04 - 0.06 μ_B) and a considerably large orbital moment anisotropy ($\Delta L^{Pt} \sim$ 0.01 μ_B). For the Co layers a large spin and orbital moment was found ($S^{Co} \sim$ 1.6 μ_B, $L^{Co} \sim$ 0.3 μ_B) together with an orbital moment anisotropy $\Delta L^{Co} \sim$ 0.13 μ_B. The magnetic moment of the interface Pt layer increased for thicker Co films [Ferrer et al., 1997].

As was recently reported by Gambardella *et al.* [Gambardella et al., 2002] the magnetic moments of monoatomic Co wires are drastically increased as compared to the corresponding monolayer case ($S^{Co}_{1D} \sim$ 2.08 μ_B, $L^{Co}_{1D} \sim$ 0.68 μ_B). The orbital moment drops to $L^{Co}_{1D} \sim$ 0.37 μ_B in the double wire case. The orbital moment anisotropy was found to be $\Delta L_{1D} \sim$ 0.14 μ_B together with an enhanced magnetic anisotropy

energy ($\Delta E_{1D} \sim 2.0$ meV/atom) which is about 14 times larger than in the corresponding ML case. The estimated average length of a continuous monoatomic Co chain was 80 atoms; at a temperature of 45 K the ferromagnetic order was, however, found to extend over about 15 Co atoms only.

10.2 Results

10.2.1 Spin and Orbital Moments

Because of the spatially extended $5d$ states of Pt, a relatively strong interaction between electronic states corresponding to the Co and the Pt atoms is to be expected. For the case of a single Co adatom. therefore, the sensitivity of the local physical properties of the Co adatom was carefully investigated with respect to the size of the environment by incorporating self-consistently treated Pt substrate atoms. Calculations were performed up to the fourth neighboring shell of Pt atoms around the Co adatom and found that in treating only the first shell of neighbors self-consistently results in to a relative deviation of less than 1% of the local charge and the magnetic moments of Co as compared to the case when all the four neighboring shells were treated self-consistently. Therefore, if not stated otherwise, in the following all calculations refer to clusters containing only Pt atoms adjacent to the Co atoms.

Fig. 10.1 shows the spin- (S_z) and orbital (L_z) moment of the central (most symmetric) atom of the monoatomic Co_n wires ($1 < n < 10$). First of all it can be noticed that the spin-moment of a single adatom (2.21 μ_B) is by about 10% larger than in the corresponding monolayer case (2.00 μ_B). This spin moment decreases with an increasing number of atoms forming the chain: in the case of a dimer $S_z = 2.17\ \mu_B$ while for the central atom of a trimer $S_z = 2.12\ \mu_B$ was found. The reason for this trend can clearly be traced from Fig. 10.2, where the spin-projected densities of states (DOS) [Szunyogh et al., 1994b; Staunton et al., 1988] of the corresponding Co atoms are displayed: for a Co adatom, the Fermi level crosses the very sharp peak of the minority spin d-band, which, as a consequence of the d-d hybridization between the Co atoms, remarkably broadens in the dimer and trimer case, thus, pushing more states below the Fermi level than above. For $n > 3$ the spin-moment of the central atom seems to be stabilized at about 2.11 μ_B, which despite of the different geometry is in good comparison to the experimental value

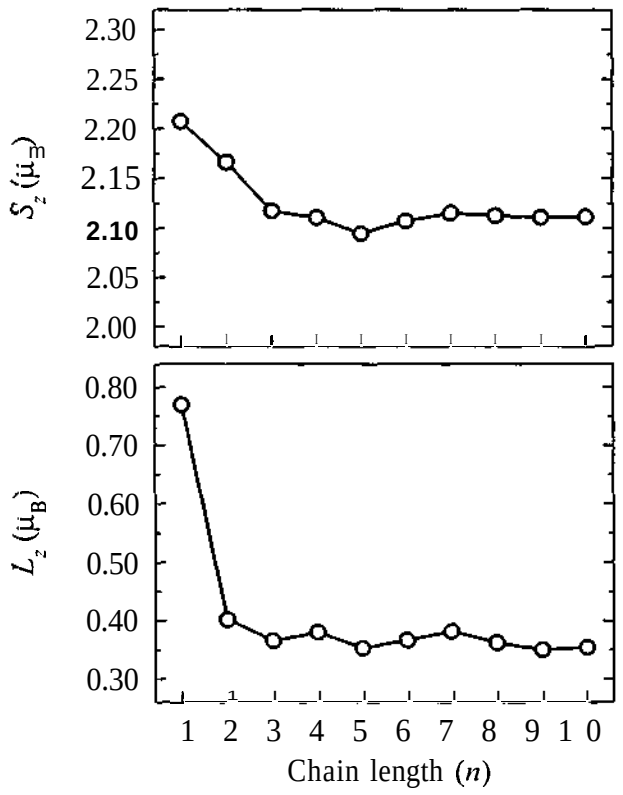

Figure 10.1: Calculated spin moments (S_z) and orbital moments (L_z) of the central (most symmetric) atom in Co_n $(n = 1, \ldots, 10)$ chains oriented along the $(1\bar{1}0)$ direction on the top of Pt(lll) as a function of the chain length.

of about 2.12 μ_B [Gambardella et al., 20021 and other LDA (FLAPW) calculations (2.06 μ_B, [Komelj et al., 2002|) for monoatomic Co chains on Pt(997).

The spin-moments calculated for each of the Co atoms in the chains are shown in Fig. 10.3. Apparently, for $n = 3, \ldots, 10$, the spin moments at the end of the chains $(\sim 2.15\ \mu_B)$ are systematically higher than those in the middle of the chains $(\sim 2.11\ \mu_B)$. This observation can again be attributed to the narrower minority spin *d*-band of the outer atoms due to one missing neighboring Co atom as compared to the inner atoms (see also Fig. 10.2). It should be noted, however, that the above feature can not be stated as a general feature, since the relation of the spin-moments of the outer and inner atoms in a linear chain can vary according to the varying nature of the *d-d* hybridization between transition metal atoms [Wildberger et al., 1995|. Contrary to the magnetic moments of compact *3d* clusters which tend rapidly

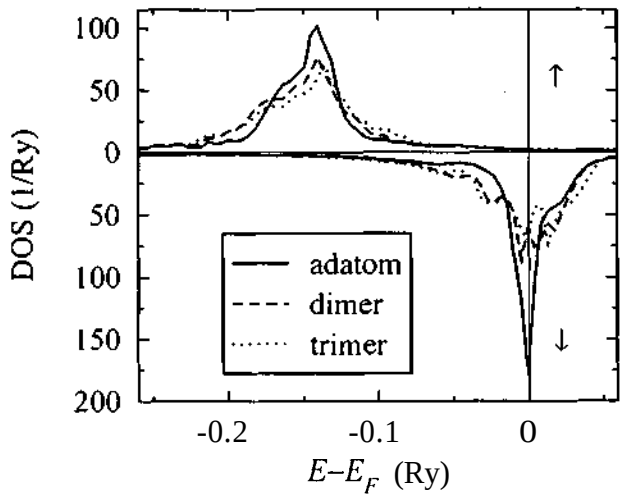

Figure 10.2: Spin-projected local densities of states (DOS) of Co as an adatom, a dimer atom and the central atom of a trimer on top of a Pt(111) surface.

to the monolayer value [Lazarovits et al., 2002] (see also chapter 9), independent of their length the wires are characterized by larger magnetic moments than the corresponding monolayer. This is one of the unique features of the nanowires which distinguishes them from other types of nanoclusters.

Inspecting the orbital moments from the lower panel of Fig. 10.1, the case of a single adatom distinctly differs from all other cases, since the huge orbital moment of the Co adatom, 0.77 μ_B, immediately decreases to 0.40 μ_B in the dimer and remains in the range of 0.35 — 0.40 μ_B for the central atom of all longer chains. This implies that the orbital moments of the Co atoms are more sensitive to the chemical environment than the corresponding spin-moments. Since the value for a Co monolayer on Pt(lll) amounts only to 0.15 μ_B, from the above results a clear trend of the Co orbital moment with respect to the dimensionality of the system (OD, 1D, 2D) can be read off.

Fig. 10.4 shows that the fluctuations of the orbital moments within the chains are somewhat larger than for the spin-moments (compare to Fig. 10.3). As can be seen, the orbital moments of the central and the outer atoms can even differ by more than 10% and also the variations at inner sites are remarkable. Nonetheless, similar to the spin-moments (see Fig. 10.3) for the inner atoms of the longer chains a tendency of forming a uniform orbital magnetization can be observed. Based on

Fig. 10.1, the Co orbital moment of the central atom was fitted numerically to the case of an infinite chain. The thus obtained value of 0.36 μ_B is smaller than the experimental value, 0.68 ± 0.05 μ_B [Gambardella et al., 2002]. For the step-edge like geometry used in Ref. [Komelj et al., 2002] an even smaller orbital moment (0.16 μ_B) was obtained, while using an orbital polarization scheme [Brooks, 1985] resulted in a value of 0.92 μ_B. While spin-polarized relativistic calculations usually underestimate the orbital part of the magnetization, in systems with reduced dimension the orbital polarization scheme seems to overestimate the orbital moments and, more peculiar, the size of the MAE [Lazarovits, 2000; Nonas et al., 2001].

Due to the experimental findings for the magnetically polarized Pt atoms at the *3d*|Pt interfaces it is worthwhile to discuss the spin- and orbital polarization of the Pt atoms close to Co sites. Depending on the position with respect to the Co chain induced Pt spin-moments of 0.09 — 0.14 μ_B and orbital moments in the range of 0.02 - 0.04 μ_B were found. These values are typically half as large as the corresponding moments considering a Pt(111) surface covered by a Co monolayer (0.22 μ_B and 0.05 μ_B, respectively). This decrease of the magnetic moments of Pt is apparently caused by the reduced number of the neighboring magnetic (Co) atoms, the actual source of the induced spin-polarization at the Pt sites. This observation agrees well with other theoretical results for a Co chain placed on Pd [Robles et al., 2000] and *3d* impurities on Pd(OOl) and Pt(OOl) surfaces [Stepanyuk et al., 1996b]. In Table 10.1 the induced spin- and orbital moments of Pt are shown treating four shells of Pt atoms selfconsistently in the neighborhood of a Co impurity on top of a Pt(lll) surface. Although the induced moments in the individual shells rapidly decrease with increasing distance from the Co impurity, the increasing number of Pt atoms gives rise to a slowly convergent total sum of moments. In particular, due to the Pt atoms, for longer chains an enhancement of the orbital moment of about 0.1 μ_B per Co atom can be estimated, which clearly improves the agreement between the present calculations and experiment (see above).

10.2.2 Magnetic Anisotropy

The induced moments on the Pt sites also imply that a considerable contribution to the MAE arises from the Pt atoms around the Co chains. Therefore, in the case of a single Co adatom again the effect of the first four nearest neighboring Pt shells on

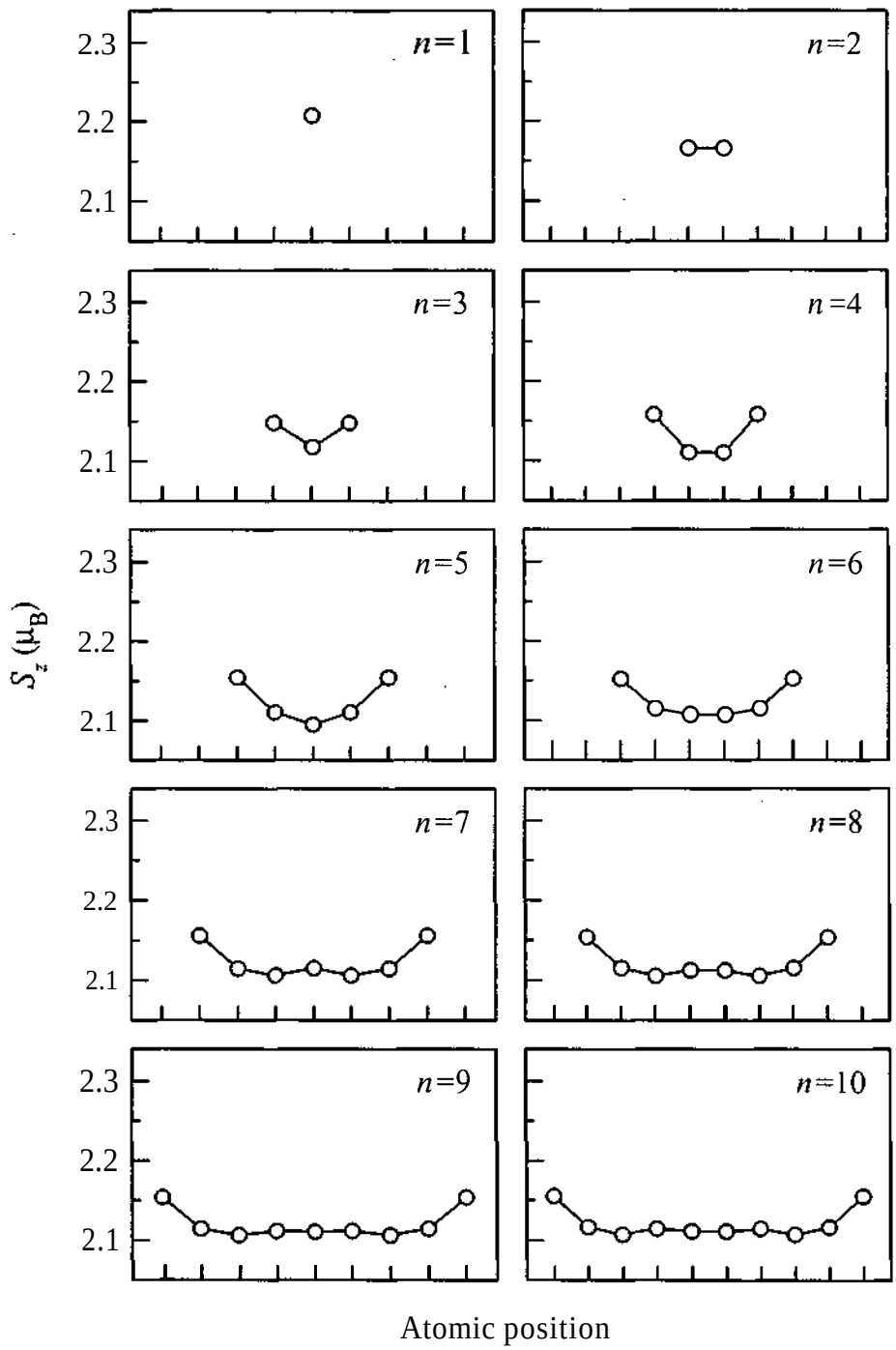

Figure 10.3: Calculated spin moments (S_z) of the Co atoms in Co_n ($n = 1, \ldots, 10$) chains on Pt(lll) with a magnetization pointing perpendicular to the surface.

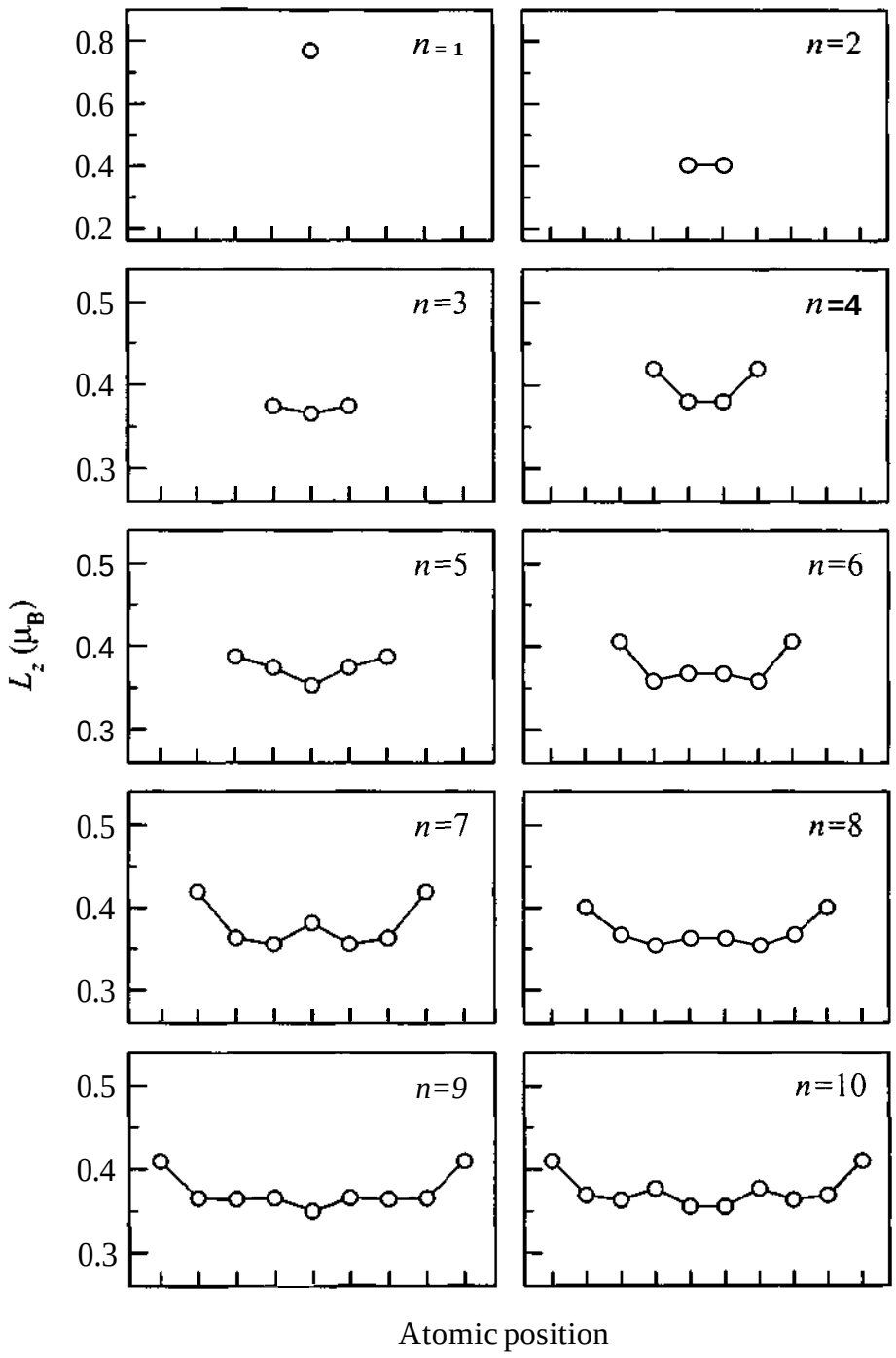

Figure 10.4: Calculated orbital moments (L_z)of the Co atoms in Co_n (n = 1, . . . , 10) chains on Pt(lll) with a magnetization pointing perpendicular to the surface.

Shell (i)	N_i	S_z^i	L_z^i	S_z	L_z
1	3	0.093	0.024	0.279	0.071
2	12	0.013	0.002	0.439	0.093
3	3	< 0.001	-0.001	0.441	0.089
4	16	0.003	0.001	0.493	0.107

Table 10.1: Calculated moments (in units of μ_B) of Pt atoms in a cluster with one Co impurity on top of a Pt(lll) surface. N_i: number of sites in the i-th shell of neighboring Pt atoms, S_z^i and L_z^i: average spin- and orbital moments in shell no. i, S_z and L_z: total sum of spin- and orbital moments of Pt atoms up to shell no. i.

the MAE was investigated. It was found that the contributions from the Pt atoms decrease rapidly with increasing distance from the Co atom and that the difference in the total MAE is less than 7% between the case when only the first shell and when all four shells of Pt atoms are included into the calculations. In the case of longer chains the Pt atoms in the first nearest shell contribute to the MAE in a similar manner (0.2 — 0.4 meV/atom depending on the position) as in the case of the adatom. Thus, also for the calculation of the MAE only the first Pt shell around the Co atoms with an estimated relative error of less than 10% was considered which seems to be a good compromise between the accuracy of the calculations and the numerical efforts required.

In Fig. 10.5 the magnetic anisotropy energies, ΔE_{x-z} and ΔE_{y-z}, including only contributions from the first shell of Pt sites (see above) and normalized to a single Co atom are shown with respect to the length of the Co chains. As can be seen from the positive sign of the MAE, in each case the easy axis points perpendicular to the surface, whereby for $n > 2$ there also appears a strong in-plane anisotropy with a preference of the x direction, i.e., parallel to the chains. It is interesting to mention that as compared to a single adatom in the case of small ($1 < n < 3$) linear clusters of Co on Ag(OOl) a reorientation of the easy axis from out-of plane to an in-line direction for the dimer and trimer [Lazarovits et al., 2002] (see also chapter 9) was found. The huge MAE of a single Co adatom, $\Delta E_{x-z} = \Delta E_{y-z} = 5.9$ meV, abruptly drops for the dimer and rapidly converges to $\Delta E_{x-z} \sim 1.5$ meV and $\Delta E_{y-z} \sim 3.3$ meV for the longer wires. Evidently, the experimental easy axis of the Co/Pt(997) chains,

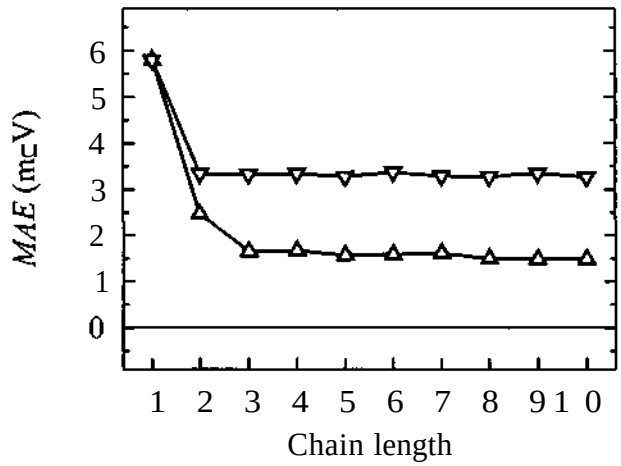

Figure 10.5: Calculated magnetic anisotropy energies (MAE) for Co_n (n = 1,. . . , 10) chains on Pt(lll) including also contributions from nearest neighbor Pt sites and normalized to one Co atom. Up- and down triangles refer to ΔE_{x-z} and ΔE_{y-z}, respectively.

perpendicular to the chains and 43° away from the normal of the (111) planes [Gambardella et al., 2002], could not be confirmed by these calculations. Nevertheless, the fact that the calculated easy axis points out-of-plane and is perpendicular to the chains, and also that the size of the calculated MAE is very close to the measured value of 2 ± 0.2 meV, can still be termed a nice agreement between experiment and theory.

The contributions of the individual Co atoms, $\Delta E^{\mathrm{Co}_i}_{x-z}$ and $\Delta E^{\mathrm{Co}_i}_{y-z}$ (i = 1,. . . , n), to the MAE are displayed in Fig. 10.6. In case of $(x - z)$, the largest contributions clearly come from the outer Co atoms, while in the $(y - z)$ case the contribution of the inner atoms to the MAE is nearly as big as the contribution of outer atoms. In both cases considered namely ΔE_{x-z} and ΔE_{y-z}, only weak oscillations in the MAE can be seen for the longer chains.

The anisotropies of the orbital moments are shown in Fig. 10.7. In the case of a single adatom the anisotropy of the orbital moment $\Delta L_{x(y)-z} = L_{x(y)} - L_z$ = -0.27 μ_B obeys the qualitative rule that the orbital moment is largest along the easy axis [Bruno, 1993]. As can be seen from Fig. 10.7, this rule applies also to the chains since along the y direction (hard axis) the orbital moments of all the Co atoms are by about 0.15 μ_B less than along the z direction (easy axis) (ΔL_{y-z} = -0.15 μ_B). Note

that this value is close to that given experimentally, namely, 0.12 μ_B [Gambardella et al., 2002]. The anisotropy of the orbital moments of the Co atoms with respect to the *x* and *z* directions (ΔL_{x-z}), however, is only a few of 0.01 μ_B, and in several cases changes even sign from site to site. This situation is quite unusual since the tiny orbital momentum anisotropies are to be compared with quite sizeable respective magnetic anisotropy energies, ($\Delta E_{x-z}^{\mathrm{Co}_i} \sim 0.5$ — 1.5 meV). In terms of perturbation theory this implies that for the *(x — z)* case, significant spin-flip coupling induced by the spin-orbit interaction may contribute to the MAE which, in turn, obscures the simple (inverse) proportionality between the MAE and the anisotropy of the orbital moment [Stöhr, 1999].

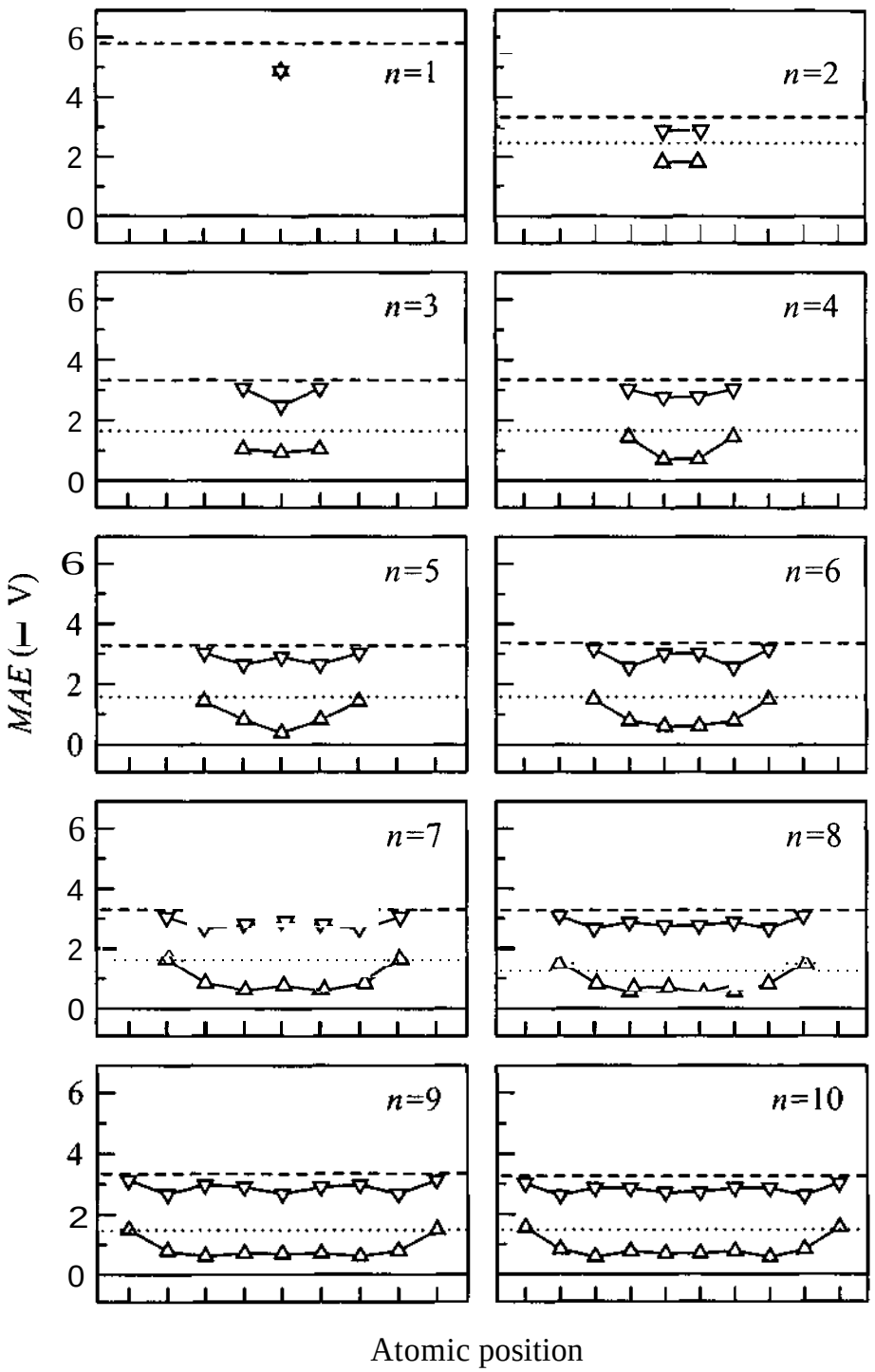

Figure 10.6: Contributions of the individual Co sites to the MAE of Co_n (n = $1, \ldots, 10$) chains on Pt(lll). Up- and down triangles refer to $\Delta E_{x-z}^{Co_i}$ and $\Delta E_{y-z}^{Co_i}$ $(i - 1, \ldots, n)$, respectively. For comparison, the corresponding MAE of the chains normalized to one Co atom is marked by dots (ΔE_{x-z}) and dashes (ΔE_{y-z}).

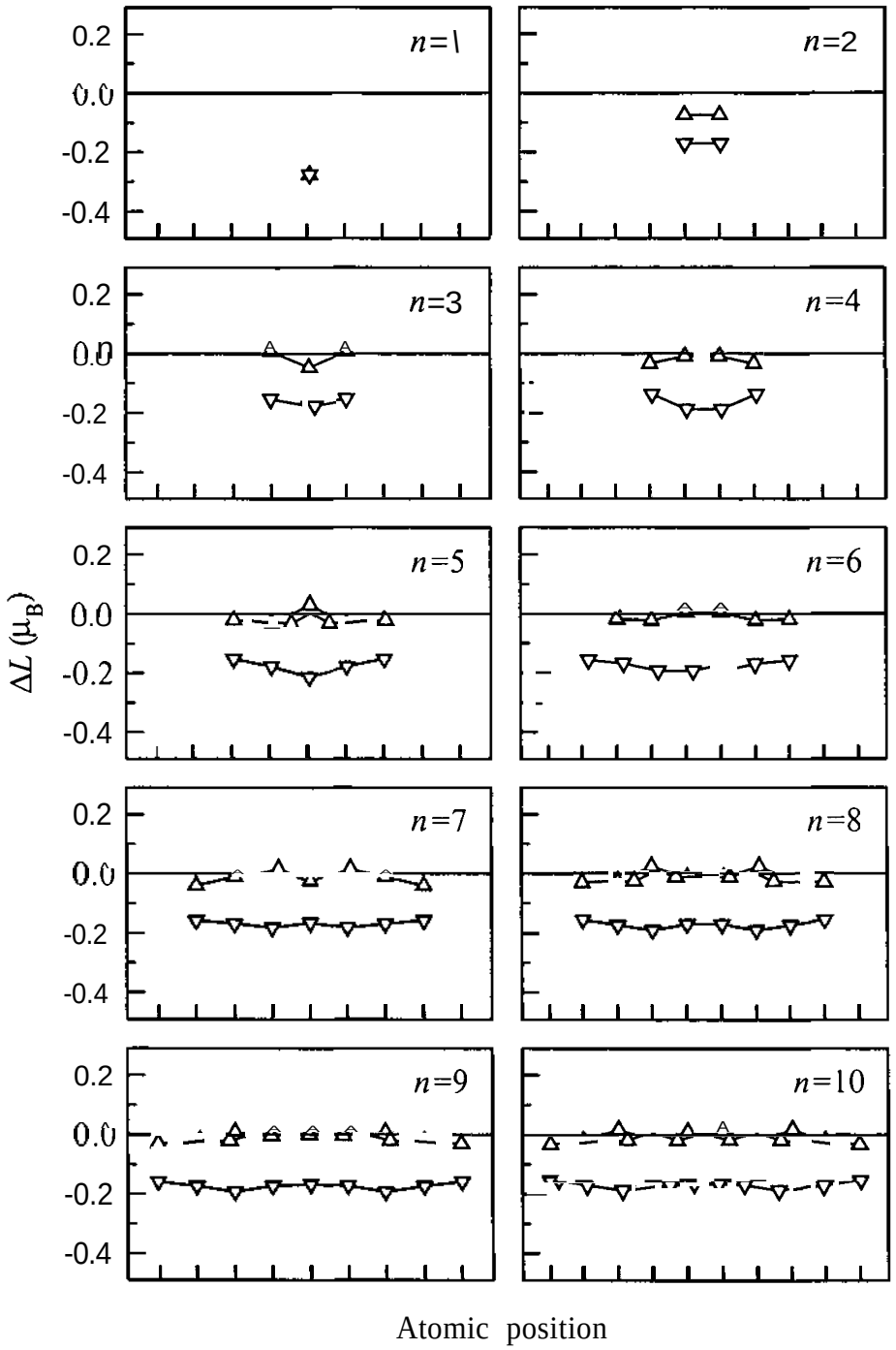

Figure 10.7: Anisotropy of the orbital moments of the Co sites in Co_n (n — 1, . . . , 10) chains on Pt(lll). Up- and down triangles refer to ΔL_{x-z} and ΔL_{y-z}, respectively.

Chapter 11

Finite Fe chains at fcc Cu(OOl) and Cu(111) surfaces

11.1 Introduction

The objective of this chapter is to study the magnetic properties of Fe_n chains deposited along the $(1\bar{1}0)$ direction on fcc Cu(OOl) and Cu(lll) surfaces as well as buried by the surface layers by performing calculations for different lengths of the chain, $1 < n < 9$, and by varying its distance from the surface. The Fe atoms substitute sites in the first vacuum layer, in the uppermost three surface layers as well as in the perfect 3D bulk host. The cluster sites refer to positions of an ideal fcc parent lattice with the experimental Cu lattice constant. For each case three different orientations for the magnetization were considered: along the z axis (perpendicular to the surface) as well as along the x and y axes referring to in-plane directions parallel and perpendicular to the chains, respectively. The role of the Fe-Fe and the Fe-host interactions on the spin- and orbital moments as well as on the MAE will be discussed. The cross-over from a point-like impurity (OD) to a linear chain (1D) in terms of the above quantities is also investigated.

11.1.1 Aspects of Growth

fcc Fe posses a large variety of magnetic behavior such as paramagnetic, antiferromagnetic, low-moment ferromagnetic, or high-moment ferromagnetic states with respect to the lattice constant. fcc bulk Fe is only stabilized above 1200 K (above the Curie temperature) therefore the magnetic behavior of this system is studied ex-

perimentally by depositing Fe on fcc substrates like fcc Cu surfaces. At low nominal coverage (< 4 — 5 ML) the Fe grows pseudomorphically on fcc Cu and then changes to a bcc structure. It was shown by Shen *et al.* [Shen et al., 1997a] that at an early stage of growth (< 1.4 ML) on a stepped Cu(lll) surface iron forms 1 — 2 ML high quasi-1D stripes along the step edges due to the step-decoration effect. The rough edges of these stripes are due to the tree equivalent (110) direction of growing.

The growth mode of Fe is sensitive to the method of growing. It was shown that thermally deposited (TD) films form 3D islands. By using pulsed laser deposition (PLD) technique the films grow in a layer-by-layer mode for both (001) [Shen et al., 1998a] and (111) [Ohresser et al., 1999] surfaces and are more stable with respect to the fcc → bcc transition. By using the PLD technique no step-decoration effect was observed on a stepped (111) surface. While Fe films grown by the TD method have a tetragonally distorted fct structure on the (001) surface, films deposited by using PLD technique are fcc like at an early stage of growth.

11.1.2 Aspects of Magnetism

It was reported by Shen *et al.* [Shen et al., 1998a] that both TD and PLD thin (< 3 ML) Fe films exhibit high-moment ferromagnetic behavior ($S \sim 2.5\ \mu_B$) on a Cu(OOl) surface, however, TD films have an out-of-plane easy axis while PLD ones have an in-plane one between thicknesses of 2 and 5 ML which shows the high sensitivity of magnetic behavior of fcc Fe films with respect to structural properties. On a Cu(111) surface the TD films were reported to be in the low-moment phase ($S \sim 0.5\ \mu_B$) [Shen et al., 1997a] and the PLD ones show high-moment ferromagnetism ($S > 2\ \mu_B$) [Shen et al., 1998b]. Both the TD and the PLD films are characterized by a perpendicular easy axis on Cu(111).

Quasi 1D Fe structures on a Cu(lll) surface also have an easy axis along the surface normal. The magnetization of these stripes is temperature and time dependent [Shen et al., 1997b]. Very recently it was observed by Boeglin *et al.* [Boeglin et al., 2002] that the orbital moment of 1D Fe structures is strongly enhanced when the size of the stripes is decreased. Strong in-plane and out-of-plane magneto-crystalline anisotropy energy favors an orientation perpendicular to the chain as was also reported.

The structure and magnetism of monoatomic Fe wires grown on different stepped

Cu(11n) (n = 3 – 11) surfaces were investigated by Spišák and Hafner [Spišák and Hafner, 2002], while Eisenbach *et al.* [Eisenbach et al., 2002] demonstrated that changing the crystallographic orientation of infinite Fe wires embedded into a Cu bulk can even result in a change of the easy axis. Recently, it was shown by Stepanyuk *et al.* [Stepanyuk et al., 2001] that small magnetic clusters buried by surface layers can be energetically more favorable than those deposited on the surface.

11.2 Results

11.2.1 Spin and Orbital Moments

For the Cu atoms adjacent the Fe impurities a relatively weak magnetic polarization was found even in the surface layer, where the magnetic polarizability of the host atoms is expected to be the strongest. The calculated spin moments of these host atoms (S_z^{Cu}) were about 0.02 μ_B and the corresponding orbital moments (L_z^{Cu}) were less than 10^{-3} μ_B. These values are much lower than found for substrate Pt atoms in a similar geometrical arrangement with Co chains (S_z^{Pt} = 0.09 — 0.14 μ_B, L_z^{Pt} = 0.02 - 0.04 μ_B) [Lazarovits et al., 2003] (see also chapter 10). For the Co-Pt system tests showed that treating only one shell of host atoms around the impurities self-consistently was sufficient to get reasonable results for the magnetic properties of the impurities. The weaker polarization of the Cu atoms as compared to the Pt atoms implies that this approach applies also for the Cu-Fe system.

In Fig. 11.1 the spin and orbital moment of a single Fe impurity is shown as a function of the distance of the impurity from the surface. It is found that the spin-only magnetic moment of a single Fe impurity deposited on a Cu(OOl) surface (3.19 μ_B) is by about 15% larger than in the corresponding monolayer case (2.78 μ_B) [Üjfalussy et al., 1996b]. This result agrees well with the full-charge density calculations of Stepanyuk *et al.* [Stepanyuk et al., 1997c].

A similar comparison between an Fe impurity embedded into the bulk host and an Fe monolayer sandwiched by two semi-infinite Cu(001) substrates shows that the difference between the corresponding spin moments of Fe (2.70 μ_B) and (2.54 μ_B), respectively, is by about 6% smaller than at the surface. This obviously demonstrates that the Fe-Cu interaction, subject to the actual position of the Fe impu-

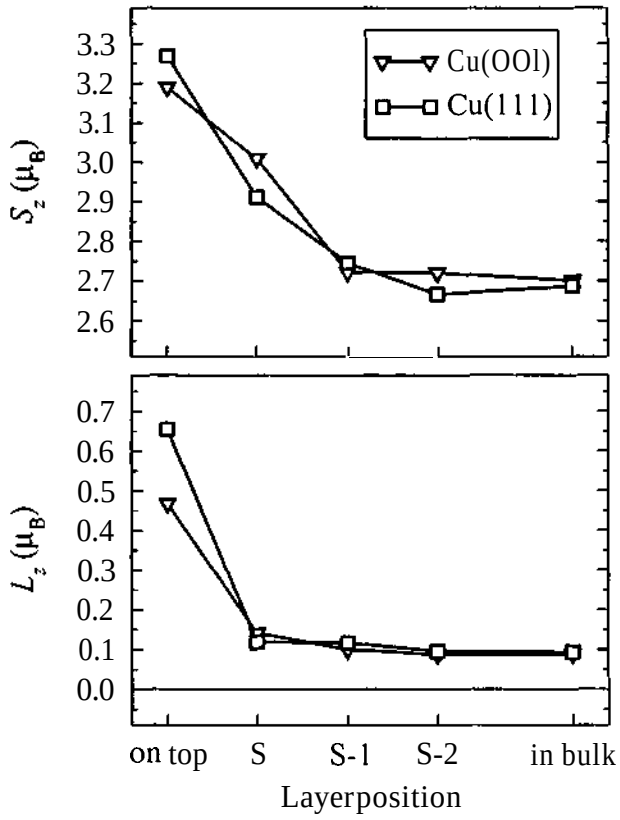

Figure 11.1: Calculated spin (S_z) and orbital moments (L_z) of a single Fe impurity embedded at different distances from a Cu(OOl) and a Cu(lll) surface with a magnetization pointing along the surface normal *(z)*. The position of the impurity is labeled as follows: on top - first vacuum layer, S - surface layer, S-l - 1st subsurface layer, S-2 - 2nd subsurface layer, in bulk - perfect bulk host.

rities, plays an important role in the formation of the magnetic properties of the Fe nanostructures. Placing the Fe impurity at increasing distances from the surface one can selectively trace the effect of hybridization between the impurity and the host atoms. A clear-cut correlation between the coordination number, N_{Cu}, of the impurity formed by the nearest neighbor Cu atoms and the actual value of the spin-moment of the impurity was observed. Inspecting Fig. 11.1 one can see that the spin moment of the Fe impurity on Cu(111) (3.27 μ_B) is larger than that on the Cu(OOl) surface (3.19 μ_B), which can be attributed to the smaller number of nearest neighbors Cu sites of the Fe impurity in case of a (111) surface (N_{Cu} = 3)

than in case of a (001) surface ($N_{Cu} = 4$). For an impurity embedded into the first Cu surface layer, on the contrary, S_z^{Fe} is larger for the (001) surface (3.01 μ_B) for which now N_{Cu} — 8 as compared to the (111) surface layer (2.91 μ_B) with N_{Cu} = 9.

Clearly enough, for Fe impurities buried deeper in the host, S_z^{Fe} differs only very little for the two kinds of surfaces and also it converges rapidly to the S_z value of an Fe impurity embedded into the bulk (2.70 μ_B) which is in good agreement with the experimental value (S_z — 2.74 μ_B) reported by Steiner *et al.* [Steiner et al., 1974]. The sensitivity of S_z^{Fe} on the choice of the surface and the distance of the impurity from the surface can be traced from Fig. 11.2 in terms of spin-projected densities of states (DOS) [Szunyogh et al., 1994a; Staunton et al., 1988] of the Fe impurity. Note that the DOS was calculated at an energy mesh parallel to the real axis with an imaginary part of 1 mRy. As can be seen the very sharp minority spin *d*-band of the Fe adatoms on the surface is intersected by the Fermi level just a little beneath the maximum of the peak. Therefore, the broadening of the minority spin band due to the increasing hybridization with Cu pushes more states below the Fermi level than above, resulting into a decrease of the spin-moment.

In Figs. 11.8 and 11.9 the calculated spin-moments are displayed for each Fe atom in the chains near the Cu(OOl) and the Cu(lll) surface, respectively. As can be seen, independent from the distance from the surface, for longer chains ($n > 3$) S_z^{Fe} is systematically higher at the edges of the chains than in the middle. This feature can (again) be attributed to the reduced coordination number, N_{Fe}, formed by the adjacent Fe atoms (N_{Fe} = *2* and 1 for atoms inside the chain and at the edge, respectively), since the strong Fe-Fe hybridization lowers the spin-moment of the Fe atoms. Note that a similar trend for Co chains on Pt(111) [Lazarovits et al., 2003] (see also chapter 10) was observed, while for Rh chains the opposite trend was reported [Wildberger et al., 1995]. The extent of the difference between the spin-moments of the inner and the outermost atoms is slightly affected by the distance from the surface.

For Fe_9 on top of Cu(111) the difference between S_z^{Fe} of the inner atoms (3.07 μ_B) and that of the outermost atoms (3.15 μ_B) is about 2% while for a chain of the same length embedded into the bulk this difference is only about 1%. In general, it can be concluded that the spin-magnetism of the Fe impurities is affected by the Fe-Cu interaction and modulated mainly by the distance of the magnetic nanostructure

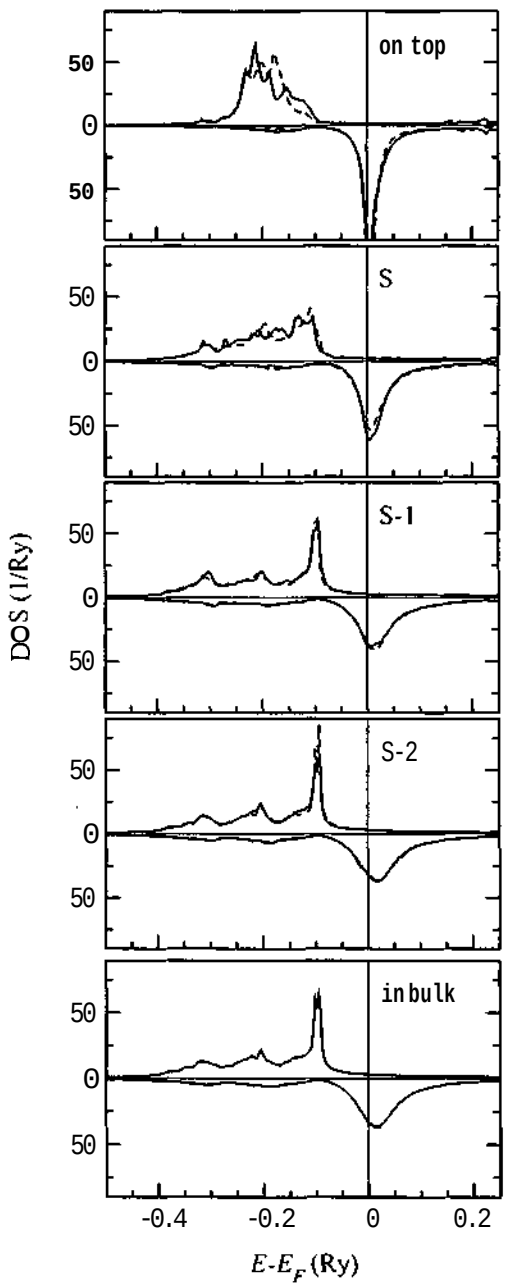

Figure 11.2: Calculated spin-projected densities of states (DOS) of an Fe impurity embedded into different layers of the Cu(OOl) (solid line) and the Cu(lll) (dashed line) surfaces and into a Cu bulk host with a magnetization pointing normal to the surface *(z).* In each entry, the majority and the minority spin-DOS is depicted in the upper and the lower panel, respectively. For the notation of the position of the impurity see Fig. 11.1.

from the surface and also by the Fe-Fe interaction.

In the lower panel of Fig. 11.1 one can see that the orbital moment of an Fe impurity dramatically decreases from its value as an adatom when it is placed into the surface and, by further moving it below the surface, it slowly tends to the corresponding bulk value. In fact, the orbital moment of the Fe adatom is about 3.3 times larger on top of the (001) surface (0.47 μ_B) than in the surface layer (0.14 μ_B), while for the (111) surface this ratio is as large as 5.5 (0.65 $\mu_B \rightarrow$ 0.12 μ_B). Note that these changes are much larger than the corresponding changes in the spin-moments ($\sim$ 6%, $\sim$ 12%, for the (001) and (111) surfaces, respectively).

Similar to previous studies of atomic-scale magnetic structures [Lazarovits et al., 2002, 2003] (see also chapters 9 and 10), this implies that the orbital moment is much more sensitive to the local environment than the spin magnetization: due to the localization of the *d*-like states (see also Fig. 11.2) L_z^{Fe} is less quenched for the adatom as compared to an impurity in or below the surface. For the same reason, the adatom on a Cu(lll) surface carries a considerably higher value of L_z^{Fe} than that deposited on a Cu(001) surface.

The calculated orbital-moments of the Fe atoms in the chains are shown in Figs. 11.10 and 11.11. As in the case of a single impurity, the chains deposited on the surface display a qualitatively different behavior as compared to those in or below the surface: L_z is much larger and also it exhibits remarkable oscillations for the chains on the surface.

Apparently these features are more pronounced for chains on a (111) surface than the (001). In case of an Fe trimer on Cu(lll), e.g., L_z of the outer atoms (0.35 μ_B) is about 2.2 times larger than that of the central one (0.15 μ_B). For longer chains ($n > 7$) the oscillations of L_z inside the chains are clearly damped. From Figs. 11.10 and 11.11 a rapid convergence of the orbital moment to the value of the chains embedded into the bulk host can be inferred.

A transition from a point-like (OD) to a quasi-one-dimensional (1D) system can be traced in terms of the spin- and orbital moments of the central atoms of the chains shown in Fig. 11.3 as a function of the length of the chains, *n*. As also can be inferred from Figs. 11.1, 11.8, 11.9, 11.10 and 11.11, up to $n = 3$ the magnetic moments decrease systematically and then seem to converge to a well-defined value. The value of S_z^{Fe} and L_z^{Fe} extrapolated from the data in Fig. 11.3 numerically to

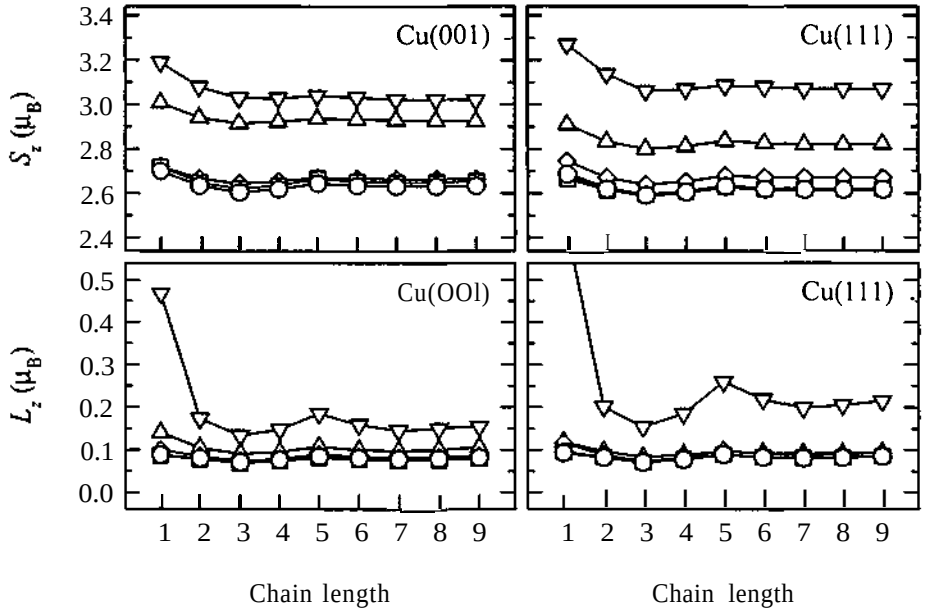

Figure 11.3: Calculated spin (S_z) and orbital moments (L_z) of the central (most symmetric) Fe atom in Fe_n (n — 2, . . . , 9) chains along the ($1\bar{1}0$) direction at the Cu(OOl) and Cu(111) surfaces with a magnetization pointing normal to the surface. (∇: on top ; A: layer S; 0: layer S-1; D: layer S-2; ○: in bulk, see Fig. 11.1).

n = ∞, listed in Tables 11.1 and 11.2, can be interpreted as an estimate for the magnetic moments in the corresponding infinite chains.

These estimated values for S_z^{Fe} compare well with the theoretical results for infinite Fe wires at a Cu(117) surface, 2.86 μ_B to 2.96 μ_B depending an the actual position of the wire, [Spišák and Hafner, 2002] and to that embedded into a copper bulk host, S_z^{Fe} = 2.50 μ_B, [Eisenbach et al., 2002]. Also listed in Table 11.1 are the moments of the corresponding Fe impurities (i.e., for the OD case) and, in case of a Cu(OOl) surface, those for the corresponding monolayers (2D) [Üjfalussy et al., 1996b]. Thus, a systematic trend of the reduction of both S_z and L_z can be seen when increasing the dimensionality of the magnetic nanostructure, OD → 1D → 2D. A similar trend has been explored experimentally [Poulopoulos and Baberschke, 1999] and theoretically [Komelj et al., 2002; Lazarovits et al., 2003] (see chapter 10) for Co nanostructures. The estimated values of L_z for infinite monoatomic chains on top (0.22 μ_B) and in the surface layer (0.10 μ_B) of Cu(lll) fit well into the tendency of the experimental values when reducing the thickness of the Fe film as reported in

Refs. [Boeglin et al., 2002; Ohresser et al., 2000].

The experimental value approximated to the wire case ($\sim 0.13\ \mu_B$) lies between the two above calculated values of L_z, most possibly since the step-edge geometry used in the experiments can be regarded as a crossover between wires on top of the surface and those embedded into the surface layer.

11.2.2 Magnetic Anisotropy

In Fig. 11.4 the MAE, ΔE_{x-z}, of single Fe impurities in different positions with respect to the Cu(OOl) and Cu(lll) surfaces and the corresponding orbital moment anisotropies, ΔL_{x-z}, are shown. Similar to previous observations [Lazarovits et al., 2002, 2003] (see chapters 9 and 10) the spin moments of the magnetic impurities are fairly insensitive to the orientation of the effective field. Comparing Figs. 11.1 and 11.4 one can find that the orbital moment and the anisotropy of orbital moment are of the same order of magnitude indicating that the orbital moment is indeed very sensitive to the magnetization direction coupled to the crystal due to the spin-orbit interaction. For an adatom placed on top of both kinds of surfaces an easy magnetization axis pointing perpendicular to the surface is favored, as can be inferred from the positive sign of the MAE (2.86 meV on Cu(OOl) and 4.30 meV on Cu(111)).

Remarkably, the MAE of the Fe adatom on Cu(OOl) is about 20 times larger as compared to the corresponding Fe monolayer case [Üjfalussy et al., 1996b]. Comparing the upper and the lower panels of Fig. 11.4 a strong correlation between AL and ΔE can be explored: in accordance with the the qualitative rule obtained from perturbation theory [Bruno, 1989; van der Laan, 1998] the easy axis corresponds to a maximum of the orbital moment. Clearly, both AL and ΔE of the Fe impurity decrease dramatically in magnitude when placed into the surface layer or below; ΔE approaches rapidly to the practically vanishing MAE of the impurity embedded into the bulk with perfect cubic symmetry. As can be seen from the oscillating sign of the MAE the orientation of the easy magnetization axis depends on the distance from the surface.

Previous theoretical studies by Szunyogh and Györffy [Szunyogh and Györffy, 1997] for Fe impurities buried by a Au surface also yielded an oscillatory behavior of the easy axis with varying distance from the surface. As can be seen in Fig. 11.2 the DOS of the Fe impurity refers to the case of a completely filled majority d-band.

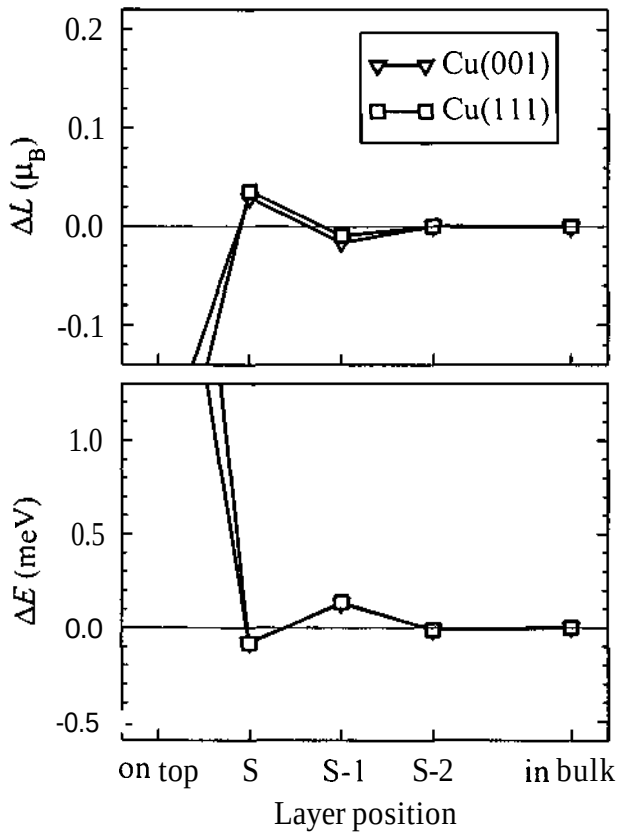

Figure 11.4: Calculated orbital moment anisotropy ($\Delta L = L_x - L_z$) and magnetic anisotropy energy ($\Delta E = E_x - E_z$) of a single Fe impurity embedded at different distances from a Cu(001) and a Cu(lll) surface. For the notation of the position of the impurity see Fig. 11.1.

Thus, the most important condition of using perturbation theory *in simple terms*, namely, omitting spin-flip processes can be assumed [Bruno, 1989; van der Laan, 1998; Stöhr, 1999]. In order to illustrate the change of the reorientation of the easy axis in terms of the electronic structure, in Fig. 11.5 the minority spin DOS of an Fe adatom on Cu(001) is plotted as well as that in the surface layer as projected onto "canonical" d_α Orbitals ($a = xy, xz, yz$, z^2 and $x^2 - y^2$). Note that only in this case the spin-orbit coupling (SOC) is "switched off" using the scaling scheme proposed by Ebert *et al.* [Ebert et al., 1996] (see appendix A).

As can be inferred from Fig. 11.5, for an Fe adatom, the large d_{xy} and $d_{x^2-y^2}$-like DOS at the Fermi level indicate a strong perpendicular anisotropy clue to the

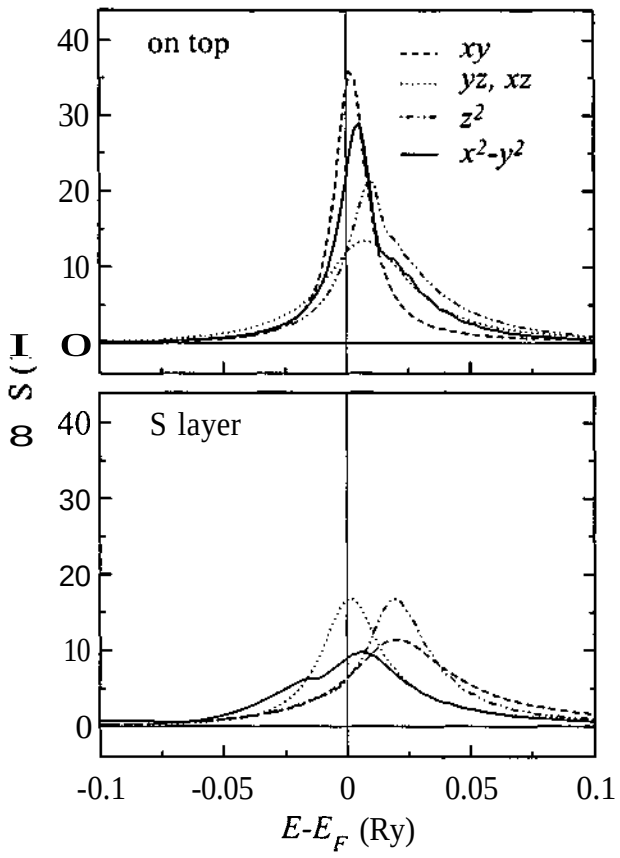

Figure 11.5: Calculated d–like minority DOS as projected onto d_{xz}, d_{yz}, d_{xy}, d_{z^2} and $d_{x^2-y^2}$ orbitals of a single Fe impurity deposited on (upper panel) and embedded into the surface layer (lower panel) of a Cu(OOl) surface.

interaction induced by the SOC (L_z-coupling) [Stöhr and König, 1995]. When placed into the surface layer, the in-plane states, namely, the d_{xy}- and $d_{x^2-y^2}$-like states of the impurity, get hybridized with mostly sp–like states of the adjacent Cu atoms, resulting into a broadening, and consequently into a corresponding lowering of these components of the DOS at the Fermi level.

The contributions of the individual Fe atoms within the chains ($n > 2$) to MAE, $\Delta E_{x-z}^{Fe_i}$ and $\Delta E_{y-z}^{Fe_i}$ ($i = 1, \ldots, n$) are displayed in Figs. 11.12 and 11.13 for a Cu(OOl) and in Figs. 11.14 and 11.15 for a Cu(111) surface. The first thing to note is that, although considerably decreased in magnitude as compared to the chains on top of the surfaces, all the contributions of $\Delta E_{x-z}^{Tr\,e_i}$ remain positive for all the embedded

chains, thus the orientation normal to the planes is always preferred with respect the one along the chains. As this observation does not apply for the case of a single Fe impurity (see Fig. 11.4), one can conclude that the origin of an easy axis normal to the chains can be attributed to the Fe-Fe bonds along the chains [Eisenbach et al., 2002; Wang et al., 1993].

For chains deposited onto the surface the direction normal to planes remains the easy axis as can be inferred from the corresponding positive values of $\Delta E_{y-z}^{Fe_i}$ in Figs. 11.13 and 11.15. However, for the embedded chains the energetical difference between the two orientations normal to the chains, namely, z and y, gets very small and converges to a value below 0.1 meV/Fe atom for the chains embedded into a perfect bulk.

On top of the surfaces, for shorter chains ($n < 5$) typical rapid variations of ΔE^{Fe_i} along the chains apply. For longer chains ($n > 6$) one can find that the largest contributions to ΔE_{y-z} come from the outermost atoms, while to ΔE_{x-z} the inner and the outermost sites add nearly the same contribution. Interestingly, this relationship is reversed for chains immersed in or below the surface: $\Delta E_{x-z}^{Fe_i}$ is systematically smaller at the edges of the chains than in the interior region, while $\Delta E_{y-z}^{Fe_i}$ seems to be quite homogeneous along the chains.

Except chains on top of the surfaces, the *total MAE* of the chains (including the contributions also from the first shell of Cu sites and as normalized to one Fe atom) is shown in Fig. 11.6. One can immediately recognize the different behavior of ΔE_{x-z} and ΔE_{y-z} with respect to the distance from the surface: the sign of ΔE_{x-z} does not change for any embedding depth, while ΔE_{y-z} is negative for wires embedded into the first layer of a Cu(OOl) surface or into the first and third layers of a Cu(lll) surface. Consequently, $\Delta E_{y-z} < 0$ refers to cases for which the easy axis is normal to both the surface and chain.

For chains embedded into the bulk, an easy axis perpendicular to both the (111) and the $(1\bar{1}0)$ directions is obtained, i.e., it can be identified by the $(11\bar{2})$ direction. Clearly, the convergence of the total MAE with respect to the length of chains is slower than that of the spin- and orbital moments of the central atoms (see Fig. 11.3), an approximate value for infinite wires can be estimated from the data contained by Fig. 11.6. Similar to the orbital moment, the estimated values of ΔE_{x-z} for the infinite wires on top and embedded into the surface layer of a Cu(lll) surface,

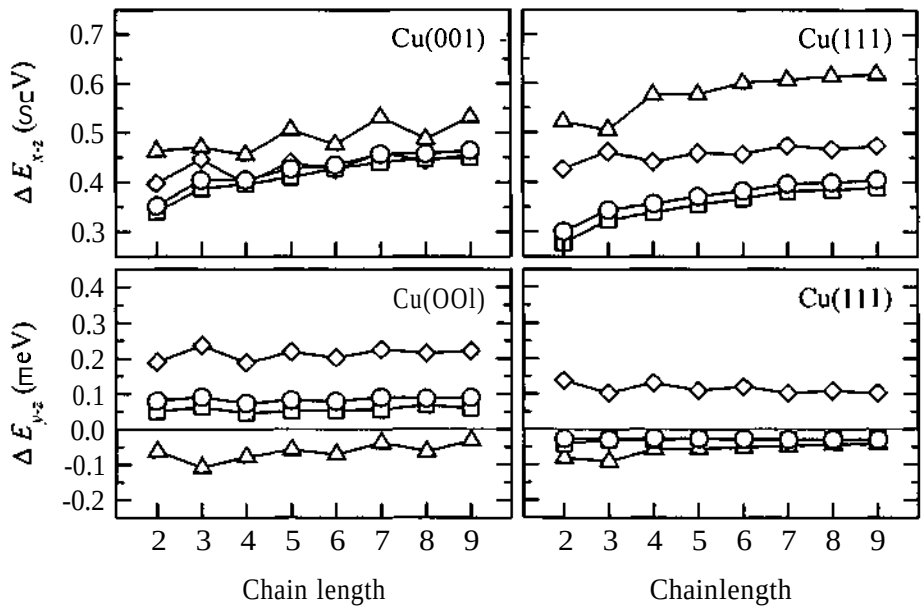

Figure 11.6: Calculated magnetic anisotropy energies, ΔE_{x-z} and ΔE_{y-z}, for Fe_n (n = 2, . . . , 9) chains immersed at different distances from a Cu(lll) and a Cu(OOl) surface including also contributions from the nearest neighbor Cu sites and normalized to one Fe atom. (A: layer S; 0: layer S-1; D: layer S-2; O: in bulk, see Fig. 11.1).

$\sim$ 1.5 meV and $\sim$ 0.65 meV, respectively, is again in a good agreement with that deduced from the experiments, $\sim$ 1.6 meV [Boeglin et al., 2002]. The perpendicular MAE numerically estimated from the results for an infinite Fe wire along the (110) direction in an fcc Cu bulk host is about 0.4 — 0.5 meV which is approximately 3 — 4 times larger as that obtained by Eisenbach *et al.* [Eisenbach et al., 2002].

This difference between the two theoretical results can be attributed to the different directions of the induced moments at the Cu sites adjacent the Fe atoms which was fixed to be parallel to the Fe moments in the present calculations but was freely fluctuating in Ref. [Eisenbach et al., 2002]. It should be noted, however, that the calculations of Ref. [Eisenbach et al., 2002] have been performed by using periodic boundary conditions in the plane normal to the wire, therefore, the corresponding results (in particular, the MAE) can also be influenced by "interchain" interactions. In Fig. 11.7 the *in-plane* magnetic anisotropy energies, ΔE_{y-x}, of chains on top and embedded into the surface layer of Cu(OOl) and Cu(lll) surfaces are displayed with

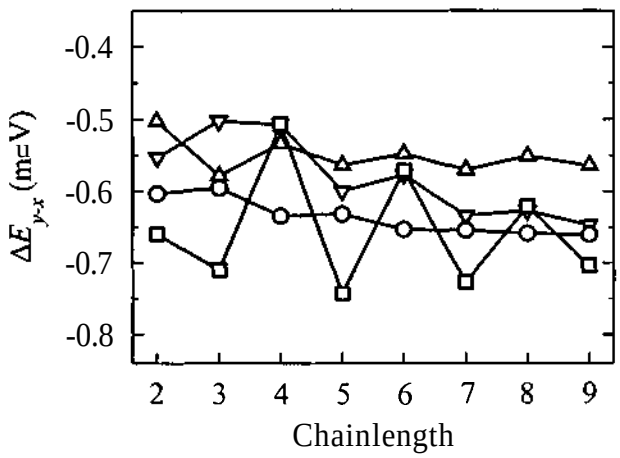

Figure 11.7: Calculated in-plane magnetic anisotropy energy, ΔE_{x-y}, for Fe_n (n = $1, \ldots, 9$) chains on a Cu(OOl) and a Cu(lll) surface including also contributions from nearest neighbor Cu sites and normalized to one Fe atom. ($\bigtriangledown$: Cu(OOl) on top ; A: Cu(OOl) layer S; D: Cu(-lll) on top; $\circ$: Cu(lll) layer S, see Fig. 11.1).

respect to the length of Fe chains. In particular, for chains on top of the Cu(lll) surface, ΔE_{y-x} shows rapid oscillations (with a period of 2 atoms) indicating that the in-plane MAE is influenced by confinement effects caused most possibly by surface states. The extrapolated value of the in-plane MAE for an infinite chain on a Cu(111) surface, $\sim$ 0.6 meV, is close to the experimental value of about 0.4 meV reported by Boeglin *et. al.* [Boeglin et al., 2002).

In order to complete the comparison between the present calculations and experiment the anisotropy of the orbital moment for an infinite Fe wire from the calculated values for the sites at the center of longer chains ($n > 7$) is also estimated, yielding a value of $\Delta L_{y-x} \sim 0.025\ \mu_B$ on top of a Cu(lll) surface and $\Delta L_{y-x} \sim 0.035\ \mu_B$ in the corresponding surface layer, again in good agreement with the experimental data $\Delta L_{y-x} \sim 0.032\ \mu_B$ [Boeglin et al., 2002).

position	S_z^{0D}	S_z^{1D}	S_z^{2D}	L_z^{0D}	L_z^{1D}	L_z^{2D}
on top	3.19	3.02	2.78	0.47	0.16	0.08
S	3.01	2.92	-	0.14	0.11	-
S-1	2.72	2.66	2.61	0.10	0.09	0.07
S-2	2.72	2.65	2.58	0.09	0.08	0.06
in bulk	2.70	2.62	2.54	0.09	0.08	0.07

Table 11.1: Calculated spin-moment (S_z) and orbital moment (L_z), in units of μ_B, of an Fe atom as a single impurity (OD) and in an infinite wire (1D) as estimated from the calculations for finite chains embedded along the $(1\bar{1}0)$ direction at different distances from a Cu(OOl) surface (on top - first vacuum layer, S - surface layer, S-1 - 1st subsurface layer, S-2 - 2nd subsurface layer, in bulk - perfect bulk host). For a comparison the moments of Fe in a $Cu_mFe_1Cu(001)$ overlayer system [Újfalussy et al., 1996b], denoted by subscript 2D, are also presented by using the mapping, m = 0: on top; m = 1: layer S-1; m = 2: layer S-2; m = ∞: in bulk.

position	S_z^{0D}	S_z^{1D}	L_z^{0D}	L_z^{1D}
on top	3.27	3.07	0.65	0.22
S	2.91	2.82	0.12	0.10
S-1	2.74	2.67	0.12	0.09
S-2	2.67	2.62	0.10	0.09
in bulk	2.69	2.62	0.09	0.08

Table 11.2: Calculated spin-moment (S_z) and orbital moment (L_z), in units of μ_B, of an Fe atom as a single impurity (OD) and in an infinite wire (1D) as estimated from the calculations for finite chains embedded along the $(1\bar{1}0)$ direction at different distances from a Cu(111) surface (on top - first vacuum layer, S - surface layer, S-1 - 1st subsurface layer, S-2 - 2nd subsurface layer, in bulk - perfect bulk host) .

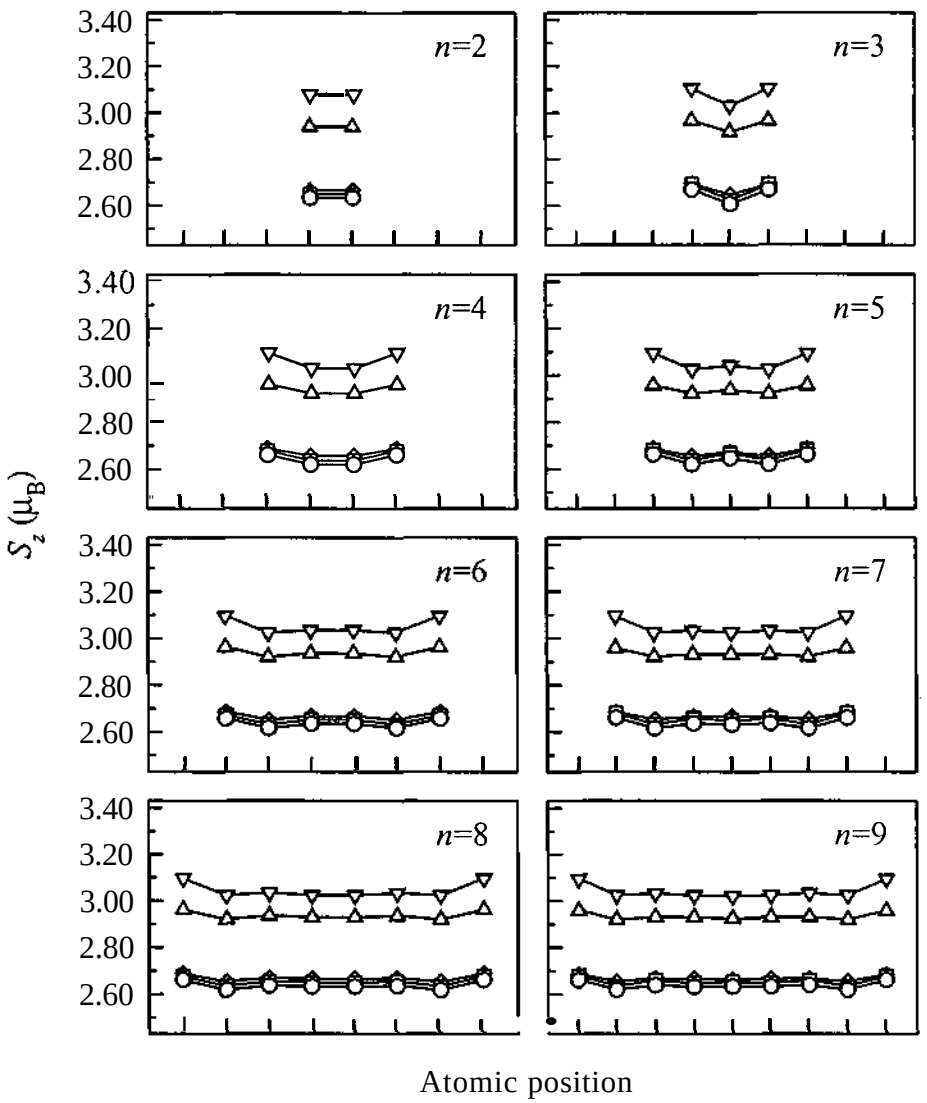

Figure 11.8: Calculated spin-moments (S_z) of the Fe atoms in Fe_n (n = 2,...,9) chains at the Cu(001) surface with a magnetization pointing normal to the surface. (∇: on top ; A: layer S; 0: layer S-1; D: layer S-2; $\circ$: in bulk, see Fig. 11.1).

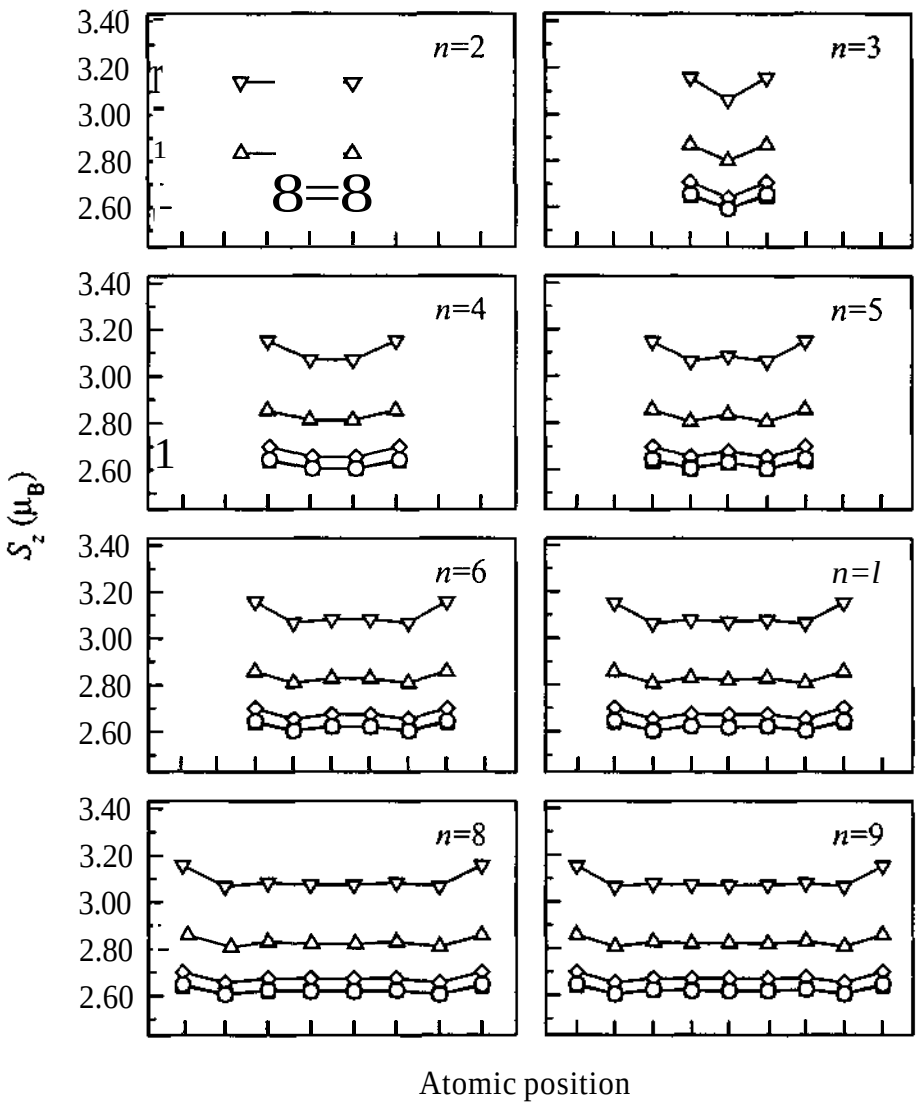

Figure 11.9: Calculated spin-moments (S_z) of the Fe atoms in Fe_n (n = 2, . . . , 9) chains at the Cu(lll) surface with a magnetization pointing normal to the surface. ($\bigtriangledown$: on top ; A: layer S; 0: layer S-1; D: layer S-2; $\circ$: in bulk, see Fig. 11.1).

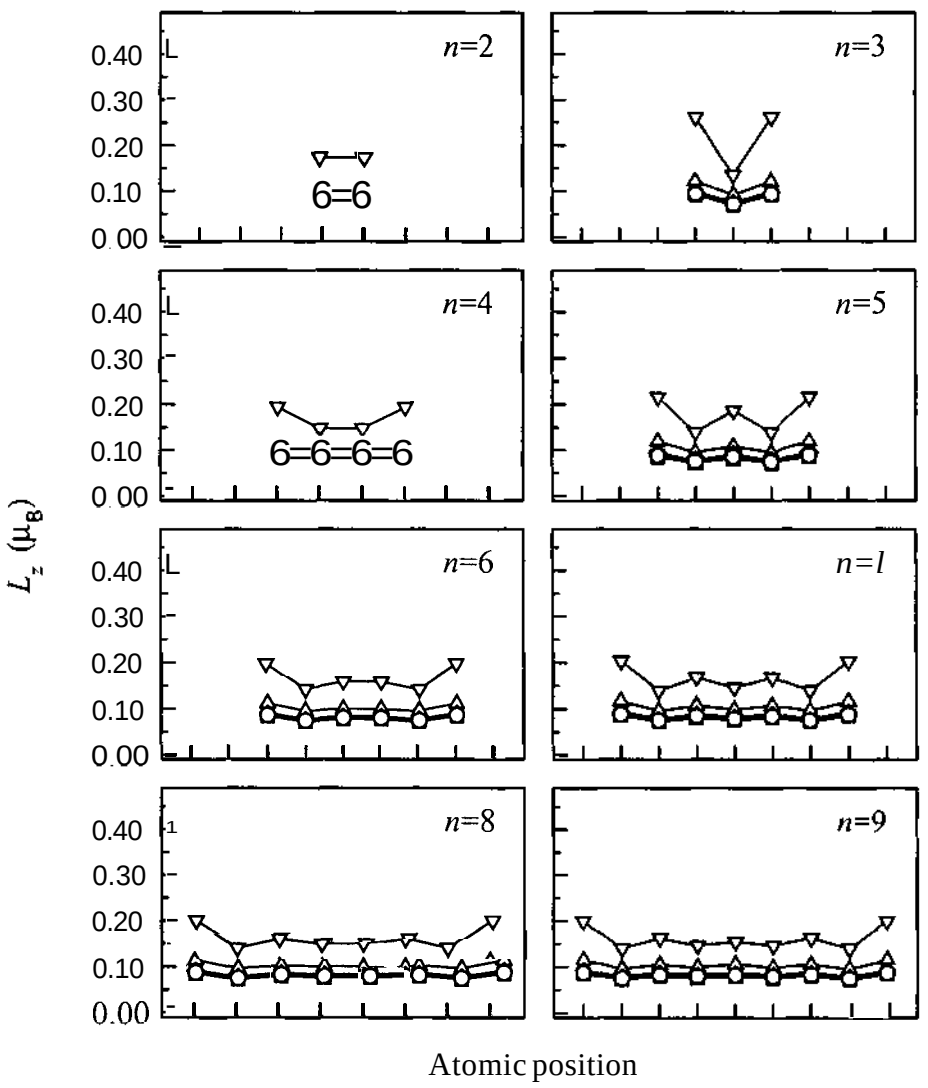

Figure 11.10: Calculated orbital moments (L_z)of the Fe atoms in Fe_n (n = 2, . . . ,9) chains at the Cu(OOl) surface with a magnetization pointing normal to the surface. (∇: on top ; A: layer S; 0: layer S-1; D: layer S-2; $\circ$: in bulk, see Fig. 11.1).

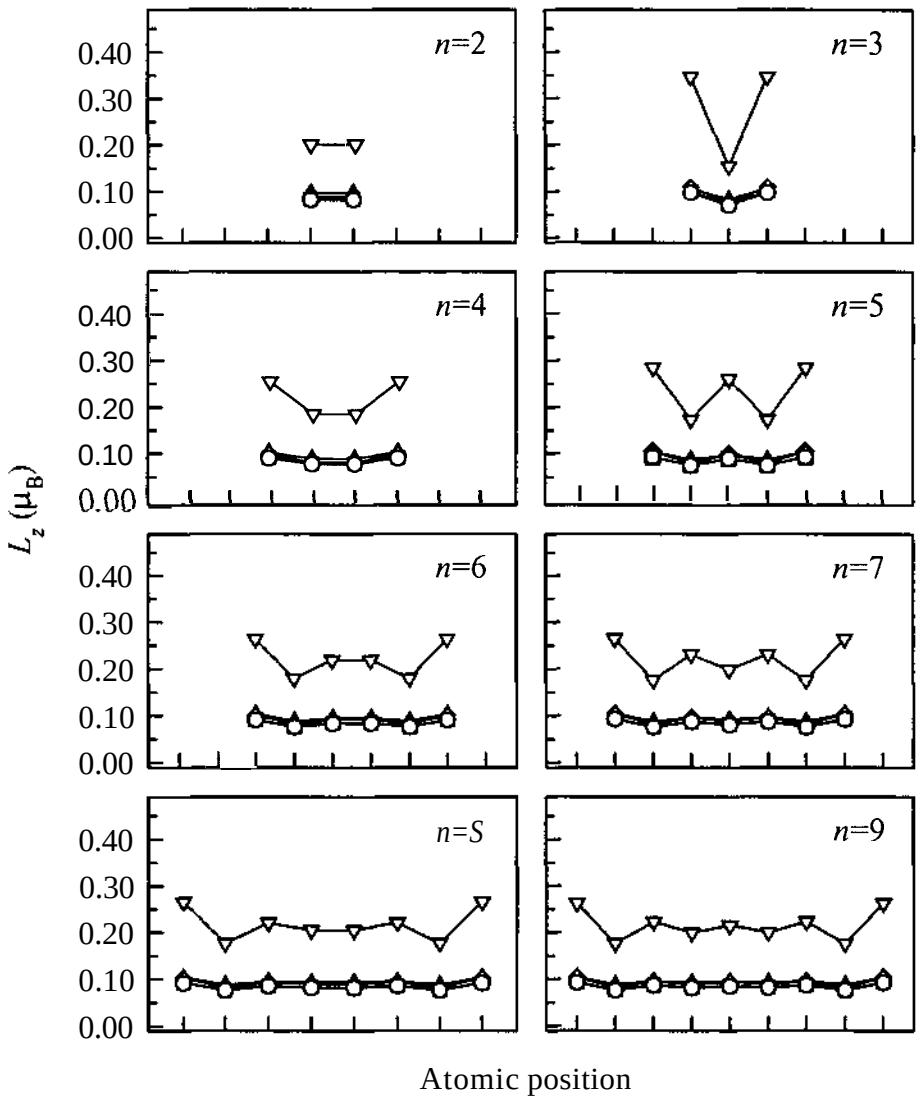

Figure 11.11: Calculated orbital moments (L_z) of the Fe atoms in Fe_n $(n — 2, \ldots, 9)$ chains at the Cu(lll) surface with a magnetization pointing normal to the surface. ($\bigtriangledown$: on top ; A: layer S; 0: layer S-1; D: layer S-2; $\circ$: in bulk, see Fig. 11.1).

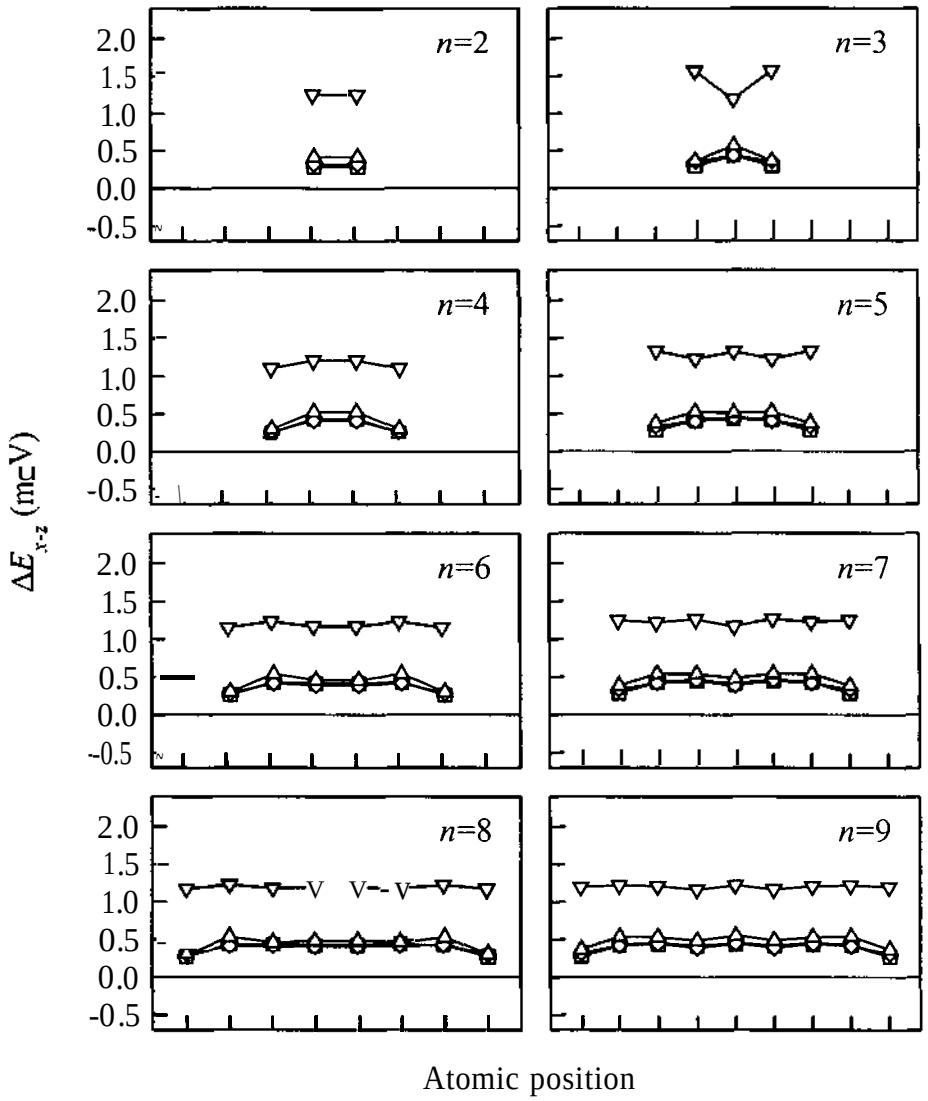

Figure 11.12: Calculated contributions of Fe atoms in chains immersed at different distances from a Cu(OOl) surface to the magnetic anisotropy energy, ΔE_{x-z}. ($\bigtriangledown$: on top ; A: layer S; 0: layer S-1; D: layer S-2; $\circ$: in bulk, see Fig. 11.1).

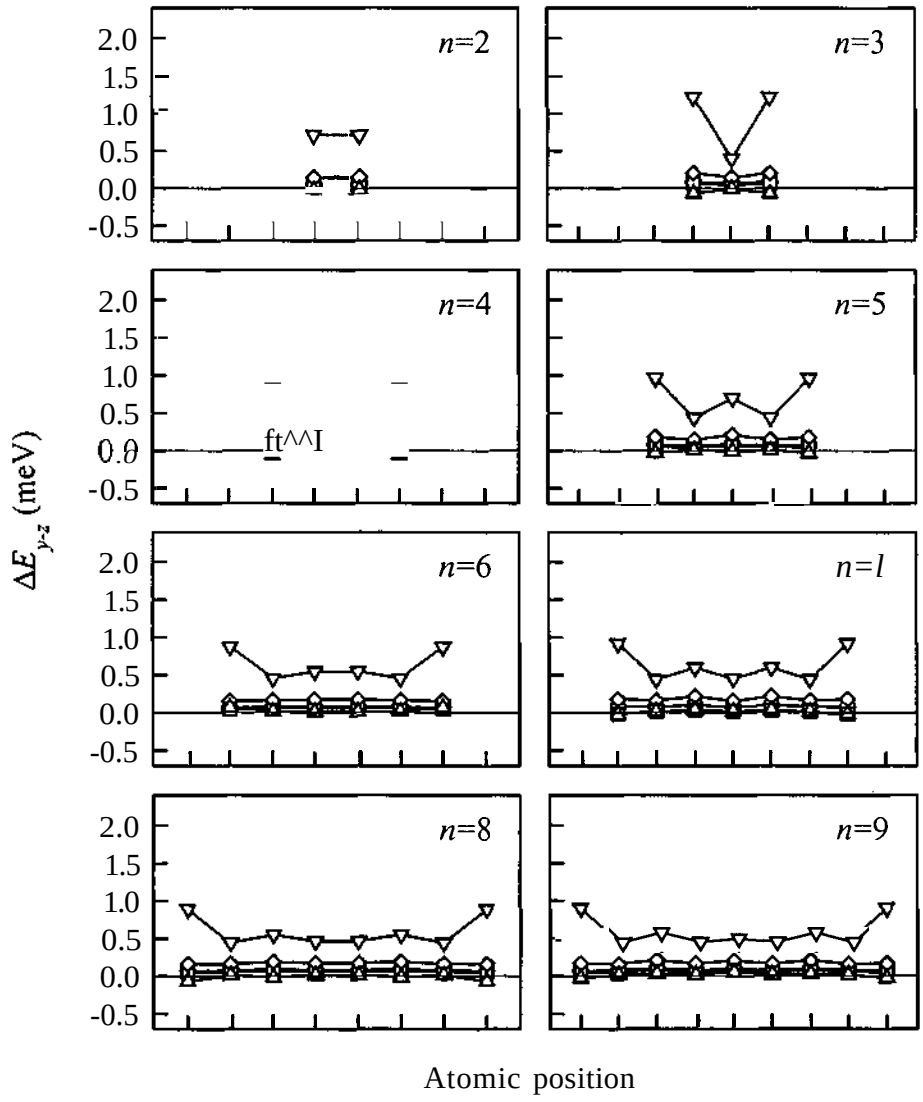

Figure 11.13: Calculated contributions of Fe atoms in chains immersed at different distances from a Cu(OOl) surface to the magnetic anisotropy energy, ΔE_{y-z}. (▽: on top ; A: layer S; 0: layer S-1; D: layer S-2;○: in bulk, see Fig. 11.1).

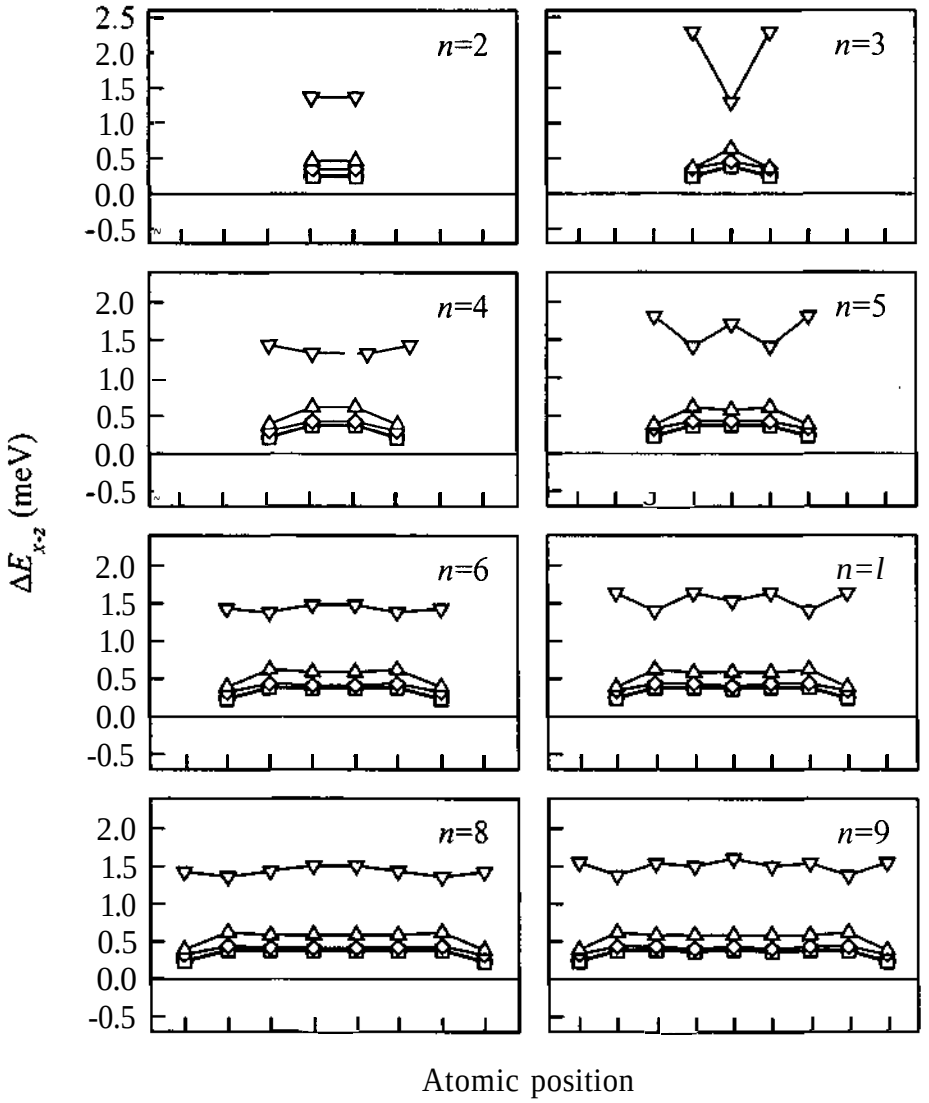

Figure 11.14: Calculated contributions of Fe atoms in chains immersed at different distances from a Cu(lll) surface to the magnetic anisotropy energy, ΔE_{x-z}. (∇: on top ; A: layer S; 0: layer S-1; D: layer S-2; $\circ$: in bulk, see Fig. 11.1).

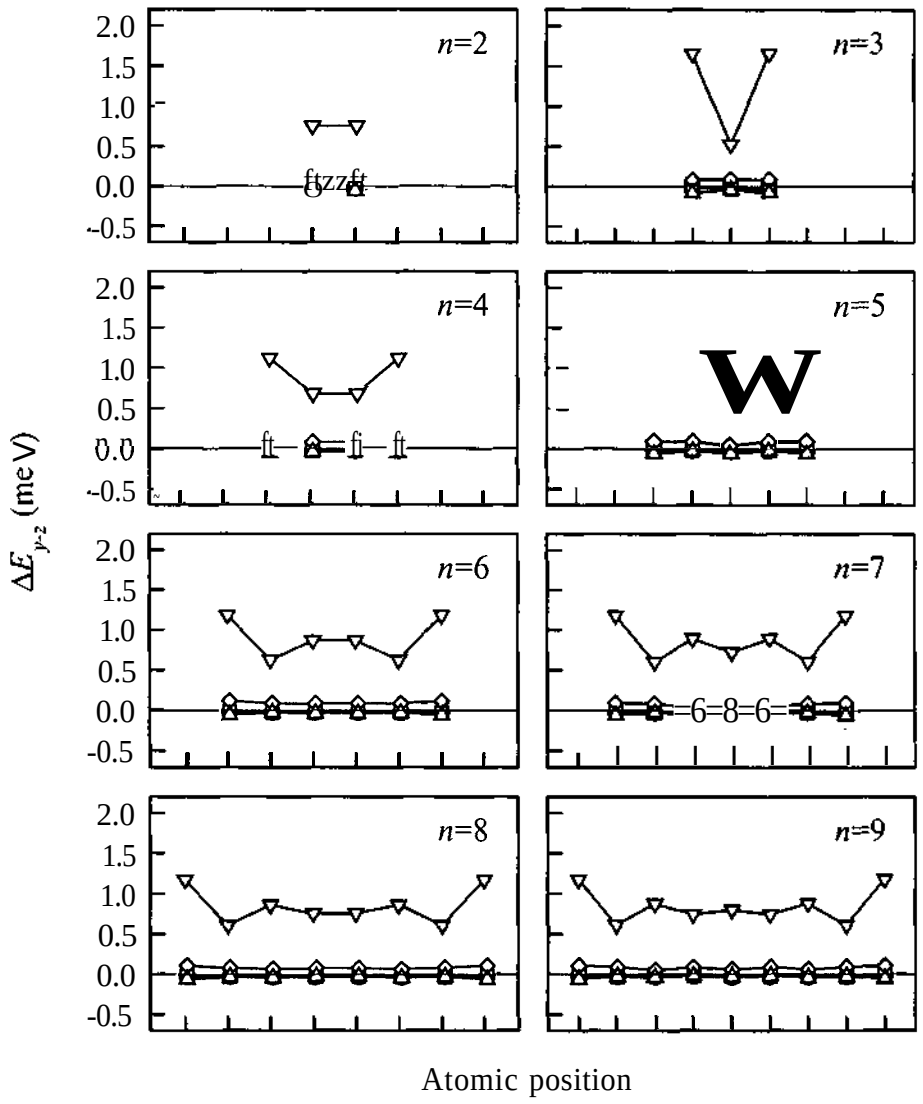

Figure 11.15: Calculated contributions of Fe atoms within the chains immersed at different distances from a Cu(lll) surface to the magnetic anisotropy energy, ΔE_{y-z}. ($\bigtriangledown$: on top ; A: layer S; 0: layer S-1; D: layer S-2; $\circ$: in bulk, see Fig. 11.1).

Chapter 12

Conclusions

By using a real-space embedding technique based on the Korringa–Kohn–Rostoker Green's function method, fully relativistic, self-consistent calculations for adatoms and small clusters of Fe, Co and Ni on Ag(OOl), finite Co chains on Pt(lll) surface and finite Fe chains at Cu(OOl) and Cu(lll) surfaces were performed. Effects of the reduced coordination number as well as the influence of the impurity-impurity and the impurity-host interactions on the spin and orbital moments and the magnetocrystalline anisotropy energy were studied. For the chains also the variation of the magnetic properties with respect to the chain length was investigated. The general conclusion is that the orbital moment of the atomic scale structures are highly increased due to the decreased coordination of the magnetic atoms as compared to the layered or bulk systems while the changes of the spin moment are less dramatic. In the most cases the value of the MAE is also enhanced and the easy-magnetization direction depends on the geometry of the clusters as well as the distance from the surface.

For adatoms and small clusters of Fe and Co on Ag(001) slightly enhanced spin moments approaching the monolayer values already for a cluster of 9 atoms was obtained. In agreement with experiments [Beckmann and Bergmann, 1996] the adatoms and dimers of Ni turned out to be nonmagnetic, while the spin moments in larger Ni clusters indicated a complex (itinerant) formation of magnetism. In connection with strongly enhanced orbital moments, for Fe and Co adatoms an unusually strong perpendicular magnetism was revealed . The perpendicular magnetism persisted also for Fe clusters of increasing size, whereby the atom-like contributions showed an oscillating behavior depending on the coordination number and

the local rotational symmetry. The preferred orientation for clusters of Co and Ni obtained was in-plane. In case of the Co clusters, from the in-plane asymmetry of the anisotropy energy it was concluded that the preferred magnetic orientation is along the Co-Co bonds. In addition, the magnetic coupling between two adatoms of Fe or Co was investigated. In terms of calculated exchange-coupling energies, the dimers show a strong ferromagnetic coupling, which immediately drops two orders of magnitude with increasing distance between the two adatoms, indicating a weak, indirect coupling between them.

For finite Co chains oriented along the $(1\bar{1}0)$ direction on top of a Pt(111) surface largely enhanced spin- and orbital moments as well as magnetic anisotropy energies as compared to the overlayer (2D) case, Co|Pt(111) were obtained, which are systematically smaller than those obtained for a single adatom (OD). For all the quantities under consideration fast convergence was found when increasing the length of the chains. Thus, from the values of the central atom the corresponding quantities for the infinite chain (1D) could easily be estimated. These extrapolated results were then successfully compared to the corresponding experimental values for long Co chains on Pt(997) [Gambardella et al., 2002].

For finite Fe chains oriented along the $(1\bar{1}0)$ direction near the Cu(001) and Cu(111) surfaces it was shown that the magnetic properties of the Fe chains strongly depend on the distance from the surface, i.e., on the local environment. As compared to the monolayer case, enhanced spin- and orbital moments as well as magnetic anisotropy energies for the chains mainly controlled by the coordination of the magnetic atoms were found. In the special case of a single Fe impurity, the changes of the spin-moment and the MAE with respect to the position of the impurity in terms of the corresponding changes in the electronic structure were illustrated. Similar for the Co chains on Pt(111), it was shown that from calculations for rather short linear chains the magnetic properties for long (ideally infinite) chains can be deduced. Although a different geometry was used in the present calculations for Co chains on Pt(111) and Fe chains on Cu(001) and Cu(111), the spin-moment of the chain atoms, the easy axis of the system, the size of the MAE and also the anisotropy of the orbital moment have been found in good agreement with experiment.

The main outcome of the present work is that by performing *first principles* calculations, not only the qualitative trends of small cluster magnetism of transition

metals, but even quantitative results can be obtained which in turn can be compared with experiments. Clearly, including structural relaxations, see also Ref. [Izquierdo et al., 2001|, e.g., by using the so-called Kambe structure constants, see Refs. [Weinberger, 1990; Kambe, 1967a,b, 1968; Uiberacker et al., 1999], would increase the ab-initio character of such calculations.

It was shown that as far as local quantities are concerned from calculations for rather short linear chains properties characteristic for long (ideally infinite) chains can be deduced without loosing the possibility to study local fluctuations (finite size effects) within the chains. Obviously, when investigating, e.g., (magneto) transport properties of such nanostructures, due to the nonlocality of the transport phenomena, a less evident trend with respect to the size of the nanoclusters has to be expected. It should be noted that by using a parallelized version of the present computer code the number of atoms treated in the cluster can be easily increased to a few hundred. This, however, is necessary to extend the present calculations to larger nanostructures (realistic wires, magnetic islands, corrals) currently being the very focus of technological applications. Recently, efforts were made to combine the present theoretical method with *ab-initio* spin-dynamics which enables one to go a step further in the understanding of the non-collinear magnetic behavior in nanostructures.

Appendix A

The Single-site Scattering with Spin Polarization

The solutions of the Dirac-equation corresponding to spherical symmetric potential and effective field pointing along the *z* direction has first been discussed by Feder *et al.* [Feder et al., 1983] and Strange *et al.* [Strange et al., 1984]. By using the ansatz, Eq. (3.52), the Dirac equation Eq. (2.29) can be written as

$$\sum_{\kappa,\mu} \begin{bmatrix} W - mc^2 - U^+(r) & -i\hbar c[\frac{d}{dr} + \frac{1}{r} - \frac{\kappa}{r}] \\ -i\hbar c[\frac{d}{dr} + \frac{1}{r} + \frac{\kappa}{r}] & W + mc^2 - U^-(r) \end{bmatrix} \begin{bmatrix} g_{\kappa\mu}(r)\chi_{\kappa\mu}(\hat{r}) \\ if_{\kappa\mu}(r)\chi_{-\kappa\mu}(\hat{r}) \end{bmatrix} = 0 \qquad (A.1)$$

where

$$U^{\pm}(r) = \begin{bmatrix} V(r) \pm B_{xc}(r) & 0 \\ 0 & V(r) \mp B_{xc}(r) \end{bmatrix} \qquad (A.2)$$

Introducing the notations $|Q\rangle = \chi_{\kappa\mu}(\hat{r})$ and $|\bar{Q}\rangle = \chi_{-\kappa\mu}(\hat{r})$ and using the orthonormality of the spinor spherical harmonics one obtains

$$\begin{bmatrix} W - mc^2 - V(r) & -i\hbar c[\frac{d}{dr} + \frac{1}{r} - \frac{\kappa}{r}] \\ -i\hbar c[\frac{d}{dr} + \frac{1}{r} + \frac{\kappa}{r}] & W + mc^2 - V(r) \end{bmatrix} \begin{bmatrix} g_{\kappa\mu}(r) \\ if_{\kappa\mu}(r) \end{bmatrix} = \sum_{\kappa'} \begin{bmatrix} \langle Q|B(r)|Q'\rangle g_{\kappa'\mu}(r) \\ -i\langle \bar{Q}|B(r)|\bar{Q}'\rangle f_{\kappa'\mu}(r) \end{bmatrix} \qquad (A.3)$$

with the matrix-elements:

$$\langle Q|B_{xc}(r)|Q'\rangle = \delta_{ll'}\delta_{\mu\mu'}B_{\kappa,\kappa',\mu}(r) = \delta_{l,l'}\delta_{\mu,\mu'}\sum_{s} C(l,\kappa,1/2|(\mu-s),s)C(l,\kappa',1/2|(\mu-s),s)2sB_{xc}(r) \qquad (A.4)$$

$$\langle \bar{Q}|B_{xc}(r)|\bar{Q}'\rangle = \delta_{\bar{l},\bar{l}'}\delta_{\mu\mu'}\bar{B}_{\kappa,\kappa',\mu}(r)= \delta_{\bar{l},\bar{l}'}\delta_{\mu,\mu'}\sum_{s} C(\bar{l},\mathrm{K},\,1/2|(\mu-s),s)C(l,\kappa',\,1/2|(\mu-\mathrm{s}),s)2sB_{xc}(r) \tag{A.5}$$

From Eq. (A.1) the following coupled radial differential equations can be obtained

$$[W - mc^2 - V(r)]g_{\kappa\mu}(r) + \hbar c\left[\frac{d}{dr} - \frac{1}{r}\right](r f_{\kappa\mu}(r)) = \sum_{\kappa'} B_{\kappa,\kappa',\mu}(r)g_{\kappa'\mu}(r) \tag{A.6}$$

and

$$-\hbar c\left[\frac{d}{dr} - \frac{\kappa}{r}\right](r g_{\kappa\mu}(r)) + (W + mc^2 - V(r)]f_{\kappa\mu}(r) = -\sum_{\kappa'} B_{\kappa,\kappa',\mu}(r)f_{\kappa'\mu}(r). \tag{A.7}$$

Instead of $g_{\kappa\mu}(r)$ and $f_{\kappa\mu}(r)$ it is practical to introduce the following functions

$$P_{\kappa\mu}(r) = r g_{\kappa\mu}(r), \qquad Q_{\kappa\mu}(r) = \hbar c r g_{\kappa\mu}(r). \tag{A.8}$$

Using the notation $E = W - mc^2$ and the atomic units ($\hbar = 1, m = \frac{1}{2}, c \sim 274$) Eqs. (A.6) and (A.7) reduce to

$$\frac{d}{dr}Q_{\kappa\mu}(r) = \frac{\kappa}{r}Q_{\kappa\mu}(r) - (E - V(r)]P_{\kappa\mu}(r) + \sum_{\kappa'} B_{\kappa\kappa',\mu}P_{\kappa'\mu}(r) \quad , \tag{A.9}$$

and

$$\frac{d}{dr}P_{\kappa\mu}(r) = -\frac{\kappa}{r}P_{\kappa\mu}(r) + \left[\frac{E - V(r)}{c^2} + 1\right]Q_{\kappa\mu}(r) + \frac{1}{c^2}\sum_{\kappa'} \bar{B}_{\kappa\kappa',\mu}Q_{\kappa'\mu}(r) \quad . \tag{A.10}$$

Because of the $\delta_{l,l'}$ in Eqs. (A.4) and (A.5) the sum over κ' contains only the values K and $-K - 1$. By using the Foldy-Wouthuysen transformation it can be shown [Feder et al., 1983] that the coupling between the channels l and $l \pm 2$ are of minor importance, therefore, it can be safely neglected. Finally one gets the following set of coupled radial equation

$$\frac{d}{dr}Q_{\kappa\mu}(r) = \frac{\kappa}{r}Q_{\kappa\mu}(r) - [E - V(r)]P_{\kappa\mu}(r) + B_{\kappa,\kappa,\mu}(r)P_{\kappa\mu}(r) + B_{\kappa,-\kappa-1,\mu}(r)P_{-\kappa-1,\mu}(r) \quad , \tag{A.11}$$

$$\frac{d}{dr}P_{\kappa\mu}(r) = -\frac{\kappa}{r}P_{\kappa\mu}(r) + \left[\frac{E - V(r)}{c^2} + 1\right] Q_{\kappa\mu}(r) + \frac{1}{c^2}\bar{B}_{\kappa,\kappa,\mu}(r)Q_{\kappa\mu}(r), \quad \text{(A.12)}$$

$$\frac{d}{dr}Q_{-\kappa-1,\mu}(r) = \frac{-\kappa - 1}{r}Q_{-\kappa-1,\mu}(r) - [E - V(r)]P_{-\kappa-1,\mu}(r) + \\ + B_{-\kappa-1,-\kappa-1,\mu}(r)P_{-\kappa-1,\mu}(r) + B_{-\kappa-1,\kappa,\mu}(r)P_{\kappa\mu}(r) \quad , \quad \text{(A.13)}$$

$$\frac{d}{dr}P_{-\kappa-1,\mu}(r) = \frac{\kappa + 1}{r}P_{-\kappa-1,\mu}(r) + \left[\frac{E - V(r)}{c^2} + 1\right] Q_{-\kappa-1,\mu}(r) + \\ + \frac{1}{c^2}\bar{B}_{-\kappa-1,-\kappa-1,\mu}(r)Q_{-\kappa-1,\mu}(r) \quad , \quad \text{(A.14)}$$

which can be solved numerically by a predictor-corrector method.

A.1 Scaling of the Spin-orbit Coupling

The relativistic treatment has the drawback that the relationship between the physical quantities and the spin-orbit coupling (SOC) cannot be studied in a direct way. In order to circumvent this problem, an approximate scheme developed by Ebert [Ebert et al., 1996] can be used. The SOC can be related to the operator ($\hbar = 1$) $\hat{K} = \vec{\sigma}\vec{L} + 1$ (see Eqs. (3.30)−(3.35)). A new operator $\hat{K}_x$ can be defined as

$$K_x = (x\vec{\sigma}\vec{L} + 1) = x(l + \vec{\sigma}\vec{L}) + (1 - x) = xK + 1 - x \quad \text{(A.15)}$$

where x is a scaling factor. The spinor spherical harmonics are eigenfunctions of $\hat{K}_x$ with eigenvalues $-\kappa_x$

$$\hat{K}_x\chi_{\kappa\mu}(\hat{r}) = -\kappa_x\chi_{\kappa\mu}(\hat{r}), \quad \text{where} \quad \kappa_x \equiv x(1 + \kappa) - 1 \quad \text{(A.16)}$$

Inserting (A.12) into (A.11) and using the identity $\kappa^2 + K = (l + 1)l$, one obtains a second-order differential equation

$$P''_{\kappa\mu}(r) = \frac{(l+1)l}{r^2}P_{\kappa\mu}(r) - S_{\kappa\mu}(r)(E - V(r))P_{\kappa\mu}(r) + S_{\kappa\mu}(r)B_{\kappa,\kappa,\mu}P_{\kappa\mu}(r) + \\ + S_{\kappa\mu}(r)B_{\kappa,-\kappa-1,\mu}P_{-\kappa-1,\mu}(r) + \frac{S'_{\kappa\mu}(r)}{S_{\kappa\mu}(r)}\left[\frac{d}{dr} - \frac{1}{r} + \frac{\kappa+1}{r}\right]P_{\kappa\mu}(r) \quad \text{(A.17)}$$

where

$$S_{\kappa\mu}(r) = \frac{E - V(r)}{c^2} + 1 + \frac{1}{c^2}\bar{B}_{\kappa,\kappa,\mu}(r) \quad . \quad \text{(A.18)}$$

In Eq. (A.17) the last term on the right hand side is the only one that explicitly depends on the SOC. Therefore, replacing K with κ_x one can scale the SOC. If $x = 0$ the SOC is switched off, if $x = 1$ the SOC is taken into account completely. In order to solve this second order differential equation for $P_{\kappa\mu}(r, E)$, an auxiliary function $Q^x_{\kappa,\mu}(r, E)$ can be defined as

$$Q^x_{\kappa\mu}(r) \equiv \frac{1}{S_{\kappa\mu}(r)} \left[P'_{\kappa\mu}(r) + \frac{\kappa_x}{r} P_{\kappa\mu} \right] \quad . \tag{A.19}$$

Note that $Q^x_{\kappa\mu}(r,E)$ is not a small component in the bispinor formalism. After some transformations one again obtains a set of coupled differential equations

$$\begin{aligned} \frac{d}{dr} Q^x_{\kappa\mu}(r) = & \frac{\kappa_x}{r} Q^x_{\kappa\mu}(r) - (E - V(r)) P_{\kappa\mu}(r) \\ & + B^{SO}_{\kappa,\kappa,\mu} P_{\kappa\mu}(r) + B^{SO}_{\kappa,-\kappa-1,\mu} P_{-\kappa-1,\mu}(r) \\ & + \frac{l(l+1) - \kappa_x(\kappa_x + 1)}{r^2} \frac{1}{S_{\kappa\mu}(r)} P_{\kappa\mu}(r) \quad , \end{aligned} \tag{A.20}$$

$$\frac{d}{dr} P_{\kappa\mu}(r) = \left[\frac{E - V(r)}{c^2} + 1 \right] Q^x_{\kappa\mu} - \frac{\kappa_x}{r} P_{\kappa\mu}(r) + \frac{1}{c^2} \bar{B}_{\kappa,\kappa,\mu} Q^x_{\kappa\mu}(r) \quad , \tag{A.21}$$

$$\begin{aligned} \frac{d}{dr} Q^x_{-\kappa-1,\mu}(r) = & \left(\kappa \quad 1 \right)_x Q^x_{-\kappa-1,\mu}(r) - (E - V(r)) P_{-\kappa-1,\mu}(r) \\ & + B^{SO}_{-\kappa-1,-\kappa-1,\mu} P_{-\kappa-1,\mu}(r) + + B^{SO}_{-\kappa-1,\kappa,\mu} P_{\kappa\mu}(r) \\ & + \frac{l(l+1) - (-\kappa-1)_x [(-\kappa-1)_x + 1]}{r^2} \frac{P_{-\kappa-1,\mu}(r)}{S_{-\kappa-1,\mu}(r)} \quad , \end{aligned} \tag{A.22}$$

$$\begin{aligned} \frac{d}{dr} P_{-\kappa-1,\mu}(r) = & \left[\frac{E - V(r)}{c^2} + 1 \right] Q^x_{-\kappa-1,\mu} - \frac{(-\kappa-1)_x}{r} P_{-\kappa-1,\mu}(r) \\ & + \frac{1}{c^2} \bar{B}_{-\kappa-1,-\kappa-1,\mu} Q^x_{-\kappa-1,\mu}(r) \quad , \end{aligned} \tag{A.23}$$

where $(-\kappa - 1)_x = x(1 - K - 1) - 1 = -\kappa_x - 1 = -x\kappa - 1$.

Appendix B

The Godfrin method

Following the method proposed by Godfrin [Godfrin, 1991] one can calculate the inverse, r, of a block tridiagonal matrix, M, by an $\mathcal{O}(N)$procedure,

$$\mathbf{M}\tau = I \quad . \tag{B.1}$$

Defining the auxiliary matrices $\mathbf{X}_i$, $\mathbf{Y}_i$, $\mathbf{C}_i$ and $\mathbf{D}_i$ $(i = 1, \ldots, N)$ with the same dimension as a block in M as

$$\begin{aligned}
\mathbf{X}_N &= 0 \\
\mathbf{X}_{N-i} &= \mathbf{M}_{N-i+1,N-i}\left[\mathbf{M}_{N-i+1,N-i+1} - \mathbf{X}_{N-i+1}\right]^{-1}\mathbf{M}_{N-i+1,N-i} \\
\mathbf{Y}_1 &= 0 \\
\mathbf{Y}_{i+1} &= \mathbf{M}_{i+1,i}\left[\mathbf{M}_{ii} - \mathbf{Y}_i\right]^{-1}\mathbf{M}_{i+1,i} \\
\mathbf{C}_i &= -\left[\mathbf{M}_{i,i} - \mathbf{X}_i\right]^{-1}\mathbf{M}_{i,i-1} \\
\mathbf{D}_i &= -\left[\mathbf{M}_{i,i} - \mathbf{Y}_i\right]^{-1}\mathbf{M}_{i+1,i} \quad ,
\end{aligned} \tag{B.2}$$

the blocks of T can be obtained as follows,

$$\begin{aligned}
\tau_{ii} &= \left[\mathbf{M}_{i,i} - \mathbf{X}_i - \mathbf{Y}_i\right]^{-1} \\
\tau_{ij} &= \mathbf{C}_i\tau_{i-1,j} \quad i > j, 1 \leq i \leq N-1 \\
\tau_{ij} &= \mathbf{D}_i\tau_{i+1,j} \quad i < j, 2 \leq i \leq N \quad ,
\end{aligned} \tag{B.3}$$

such that only $\mathcal{O}(N)$operations are needed instead of $\mathcal{O}(N^3)$operations necessary to invert a general dense matrix.

Appendix C

Rotational Properties of the Structure Constants

Using the definition of the Fourier transform of the structure constant in Eq. (5.5) one can write,

$$\underline{G}_0^{pq}(z;\hat{R}\mathbf{k}_{\|}) = \sum_{\mathbf{T}_i \in \mathcal{L}_{\|}} e^{i\mathbf{T}_i(\hat{R}\mathbf{k}_{\|})} \underline{G}_0^{pi,q0}(z) \quad , \tag{C.1}$$

where p, q are layer indices, $\hat{R}$ is element of the point-group of the 2D lattice, $\mathbf{k}_{\|}$ is in the surface Brillouin zone (SBZ) and $\{\mathbf{T}_i\, E\, \mathcal{L}_{\|}\}$ are in-plane lattice vectors. The matrix $\underline{G}_0^{pi,q0}(z)$ depends on the difference of the corresponding lattice vectors.

$$\underline{G}_0^{pi,q0}(z) = \underline{G}_0(z;\mathbf{c}_p + \mathbf{T}_i - \mathbf{c}_q) \quad , \tag{C.2}$$

where $\mathbf{c}_p$ and $\mathbf{c}_q$ are the generating vectors of the pth and the qth layers, respectively. Inserting Eq. (C.2) into Eq. (C.1) one gets

$$\underline{G}_0^{pq}(z;\hat{R}\mathbf{k}_{\|}) = \sum_{\mathbf{T}_i \in \mathcal{L}_{\|}} e^{i(\hat{R}^{-1}\mathbf{T}_i)\mathbf{k}_{\|}} \underline{G}_0(z;\mathbf{c}_p + \mathbf{T}_i - \mathbf{c}_q) \quad . \tag{C.3}$$

which, by using the notation $\hat{R}^{-1}\mathbf{T}_i = \mathbf{T}_i'$ can be written as

$$\underline{G}_0^{pq}(z;\hat{R}\mathbf{k}_{\|}) = \sum_{\mathbf{T}_i' \in \mathcal{L}_{\|}} e^{i\mathbf{T}_i'\mathbf{k}_{\|}} \underline{G}_0(z;\mathbf{c}_p + \hat{R}\mathbf{T}_i' - \mathbf{c}_q) \quad . \tag{C.4}$$

The transformation of the real-space structure constants can be derived as follows, using Eq. (3.92) one can write,

$$G_0(z;R(\mathbf{r}_i + \mathbf{R}_i), R(\mathbf{r}_j + \mathbf{R}_j)) = \overline{} \quad J_Q(R\mathbf{r}_i)G_{0,QQ'}(zR(\mathbf{R}_j - \mathbf{R}_i))J^{\dagger}_{Q'}(\hat{R}\mathbf{r}_j) \quad \text{(C.5)}$$

which by exploiting (3.64) can be written as,

$$G_0(z;\hat{R}(\mathbf{r}_i + \mathbf{R}_i), \hat{R}(\mathbf{r}_j + \mathbf{R}_j)) = \sum_{QQ'}\sum_{Q''Q'''} J_{Q''}(\mathbf{r}_i)D_{Q''Q}(\hat{R}^{-1})G_{0,QQ'}\left(z;R(\mathbf{R}_j - \mathbf{R}_i)\right)D^{*}_{Q'Q'''}(\hat{R}^{-1})J^{!}_{Q'''}(\mathbf{r}_j) \quad , \quad \text{(C.6)}$$

where $\underline{D}(\hat{R}^{-1})$ is the block-wise bispinor representation of $\hat{R}^{-1}$. Due to the invariance of the free Green function it turns out that

$$\text{GO}\,(z;(\mathbf{R}_j - \mathbf{R}_i)) = \underline{D}(\hat{R}^{-1})\underline{G}_0(z;R(\mathbf{R}_j - \mathbf{R}_i))\,\underline{D}^{\dagger}(\hat{R}^{-1}) \quad . \quad \text{(C.7)}$$

Therefore,

$$\underline{G}_0(z;\mathbf{c}_p + \hat{R}\mathbf{T}'_i - \mathbf{c}_q) = \underline{D}(\hat{R})\underline{G}_0(z;\hat{R}^{-1}(\mathbf{c}_p - \mathbf{c}_q) + \mathbf{T}'_i)\underline{D}^{\dagger}(\hat{R}) \quad , \quad \text{(C.8)}$$

and the lattice Fourier transformation (C.4) can be rewritten as,

$$\underline{G}^{pq}_0(z;\hat{R}\mathbf{k}_{\|}) = \sum_{\mathbf{T}'_i \in \mathcal{L}_{\|}} e^{i\mathbf{T}'_i\mathbf{k}_{\|}}\underline{D}(\hat{R})\underline{G}_0(z;\hat{R}^{-1}(\mathbf{c}_p - \mathbf{c}_q) + \mathbf{T}'_i)\underline{D}^{\dagger}(\hat{R}) \quad . \quad \text{(C.9)}$$

Splitting up the vector $\hat{\text{fi}}^{-1}(\text{cp} - \mathbf{c}_q)$ into components perpendicular and parallel to the layers,

$$\hat{R}^{-1}(\mathbf{c}_p - \mathbf{c}_q) = \hat{R}^{-1}(\mathbf{c}_p - \mathbf{c}_q)_{\perp} + \hat{R}^{-1}(\mathbf{c}_q - \mathbf{c}_q)_{\|} \quad \text{(C.10)}$$

one finds that

$$\hat{R}^{-1}(\mathbf{c}_p - \mathbf{c}_q)_{\perp} = (\mathbf{c}_p - \mathbf{c}_q)_{\perp} \quad , \quad \text{(C.11)}$$

because $\hat{R}$ is a symmetry operation operation of the 2D lattice. Defining

$$\Delta\mathbf{c}_{pq,\|} = \hat{\ } \quad \text{fi-}^{1}(\text{c}_p\text{-c},)\|\text{-}(\text{c}_p\text{-c},)|, \quad = \hat{R}^{-1}(\mathbf{c}_p - \mathbf{c}_q) - (\mathbf{c}_p - \mathbf{c}_q) \quad , \quad \text{(C.12)}$$

one obtains,

$$\underline{G}_0(z;\hat{R}^{-1}(\mathbf{c}_p - \mathbf{c}_q) + \mathbf{T}_i') = \underline{G}_0(z; (\mathbf{c}_p - \mathbf{c}_q)_\perp + \hat{R}^{-1}(\mathbf{c}_p - \mathbf{c}_q)_{||} + \mathbf{T}_i') = \underline{G}_0(z; (\mathbf{c}_p - \mathbf{c}_q) + \mathbf{T}_i' + \Delta\mathbf{c}_{pq,||}) \quad . \tag{C.13}$$

If $\Delta\mathbf{c}_{pq,||}$ is also an in-plane lattice vector, which is the case for fcc(lOO) and fcc(lll) surfaces, one can use the identification

$$\mathbf{T}_i' + \Delta\mathbf{c}_{pq,||} \rightarrow \mathbf{T}_i \quad , \tag{C.14}$$

which allows us to write

$$\underline{G}_0^{pq}(z;\ \hat{\text{fik}}||) = \sum_{\mathbf{T}_i \in \mathcal{L}_{||}} e^{i\mathbf{T}_i\mathbf{k}_{||}} e^{-i\Delta\mathbf{c}_{pq,||}\mathbf{k}_{||}} \underline{D}(\hat{R})\underline{G}_0^{pi,q0}(z)\underline{D}^{\dagger}(\hat{R}) \quad , \tag{C.15}$$

or

$$\underline{G}_0^{pq}(z; \hat{R}\mathbf{k}_{||}) = e^{-i\Delta\mathbf{c}_{pq,||}\mathbf{k}_{||}} \underline{D}(\hat{R})\underline{G}_0^{pq}(z; \mathbf{k}_{||})\underline{D}^{\dagger}(\hat{R}) \quad . \tag{C.16}$$

which is the desired symmetry transformation of the structure constant in 2D *k*-space.

Appendix D

Computational details

The self-consistent calculations of the surfaces were performed in terms of the fully relativistic Screened Korringa-Kohn-Rostoker method (see chapter 5) with a repulsive potential V_r = 2 Ry. 3 — 4 layers of empty sites were used in each calculation to represent the vacuum region. For the calculation of the t–matrices a cut-off of ℓ_{max} — 2 was used. The local spin-density approximation was applied as parameterized by Vosko *et ai.* [S. H. Vosko et al., 1980].

D.1 Contour integration

In order to perform the energy integrations (3.29), 16 points on a semicircular contour in the complex energy plane were sampled according to an asymmetric Gaussian quadrature.

D.2 BZ integration

For the self-consistent calculations of the surfaces as well as for the evaluation of the real-space SPO (5.44) 45 — 70 $k_{||}$-points in the irreducible wedge of the SBZ (depending on the surface) were used in order to perform self-consistent calculations for the impurities. For some restricted cases the convergence of the results was checked by increasing the number of fc||-points up to 210. For the MAE up to 1200 $k_{||}$–points in IBZ were taken into account ensuring a reliable numerical accuracy.

D.3 Multipole expansion

For the calculation of the multipole expansion of the charge densities (7.14), necessary to evaluate the Madelung potentials, a cut-off of $l'_{max} = 1$ for the unperturbed host and $l_{max} — 2$ for the cluster calculations was used (7.44). The Ewald parameter a (see Eq. (7.25)) was chosen to be 2.0.

Bibliography

S. L. Altmann and P. Herzig. *Point-Group Theory Tables.* Clarendon, Oxford, 1994.

O. K. Andersen and 0. Jepsen. Phys. Rev. Lett. 53, 2571 (1984).

H. Beckmann and G. Bergmann. Phys. Rev. B 54, 368 (1996).

S. V. Beiden, W. M. Temmerman, Z. Szotek, G. A. Gehring, G. M. Stocks, Y. Wang, D. M. C. Nicholson, W. A. Shelton, and H. Ebert. Phys. Rev. B 57, 14247 (1998).

V. Bellini, N. Papanikolaou, R. Zeller, and P. H. Dederichs. Phys. Rev. B 64, 094403 (2001).

F. Bloch and G. Gentile. Z. Physik **70**, 395 (1931).

C. Boeglin, S. Stanescu, J. P. Deville, P. Ohresser, and N. B. Brookes. Phys. Rev. B 66, 014439 (2002).

P. J. Braspenning and A. Lodder. Phys. Rev. B 49, 10222 (1994).

H. Brooks. Phys. Rev. 58, 909 (1940).

M. S. Brooks. Physica (Amsterdam) 130B, 6 (1985).

P. Bruno. Phys. Rev. B 39, 865 (1989).

P. Bruno. *in* Magnetismus von Festkörpern und Grenzflächen *(IFF-Ferienkurs, Forschungszentrum Jülich, 1993)*, page 24.1., 1993.

I. Cabria, B. Nonas, R. Zeller, and P. H. Dederichs. Phys. Rev. B 65, 054414 (2002).

S. Y. Chou, P. R. Krauss, and L. Kong. J. Appl. Phys. 79, 6101 (1996).

M. F. Crommie, C. P. Lutz, D. M. Eigler, and E. J. Heller. Physica D 83, 98 (1995).

S. L. Cunningham. Phys. Rev. B 10, 4988 (1974).

G. H. O. Daalderop, P. J. Kelly, and M. F. H. Schuurmans. Phys. Rev. B 41, 11919 (1990).

P. H. Dederichs and R. Zeller. Phys. Rev. B 28, 5462 (1983).

J. Dorantes-Dávila, H. Dreyssé, and G. M. Pastor. Phys. Rev. B 46, 10432 (1992).

J. Dorantes-Dävila and G. M. Pastor. Phys. Rev. Lett. 81, 208 (1998).

R. Družinić and W. Hübner. Phys. Rev. B 55, 347 (1997).

H. Ebert and M. Battocletti. Solid State Commun. 98, 785 (1996).

H. Ebert, H. Freyer, A. Vernes, and G. Y. Guo. Phys. Rev. B 53, 7721 (1996).

M. Eisenbach, B. L. Györffy, G. M. Stocks, and B. Újfalussy. Phys. Rev. B 65, 144424 (2002).

H. J. Eimers, J. Hauschild, H. Höche, U. Gradmann, H. Bethge, D. Heuer, and U. Köhler. Phys. Rev. Lett. 73, 898 (1994).

M. Farkas. *"Special Functions"*. Akadémia Kiadó, Budapest, 1964. in Hungarian.

J. S. Faulkner and G. M. Stocks. Phys. Rev. B 21, 3222 (1980).

R. Feder, F. Rosicky, and B. Ackermann. Z. Physik B 52, 31 (1983).

R. Felix-Medina, R. Guirado-Löpez, J. Dorantes-Dävila, and G. M. Pastor. J. Appl. Phys. 87, 4894 (2000).

R. Félix-Medina, J. Dorantes-Dävila, and G. M. Pastor. New Journal of Physics 4, 99.1 (2002).

S. Ferrer, J. Alvarez, E. Lundgren, X. Torrelles, P. Fajardo, and F. Boscherini. Phys. Rev. B 56, 9848 (1997).

G. C. Fletcher. Proc. R. Soc. London 67A, 505 (1954).

P. Gambardella, M. Blanc, L. Bürgi, K. Kuhnke, and K. Kern. Surf. Sci. 449, 93 (2000)a.

P. Gambardella, M. Blanc, H. Brune, K. Kuhnke, and K. Kern. Phys. Rev. B 61, 2254 (20QO)b.

P. Gambardella, A. Dalimeyer, K. Maiti, M. C. Malagoli, W. Eberdardtan, K. Kern, and C. Carbone. Nature 416, 301 (2002).

E. M. Godfrin. J. Phys.: Condens. Matter 3, 7843 (1991).

A. Gonis. *"Green Functions for Ordered and Disordered Systems"*. Elsevier Science Ltd, North Holland, 1992.

W. Grange, M. Märet, J.-P. Kappler, J. Vogel, A. Fontaine, F. Petroff, G. Krill, A. Rogalev, J. Goulon, M. Finazzi, and N. B. Brookes. Phys. Rev. B 58, 6298 (1998).

P. Grütter and U. T. Dürig. Phys. Rev. B 49, 2021 (1994).

R. Guirado-Löpez, M. C. Desjonquères, and D. Spanjaard. Phys. Rev. B 62, 13188 (2000).

R. Guirado-López. Phys. Rev. B 63, 174420 (2001).

O. Gunnarsson and B. I. Lundqvist. Phys. Rev. B 13, 4274 (1976).

B. L. Györffy. Phys. Rev. B 5, 2382 (1972).

B. L. Györffy and M. J. Stott. *"Band Structure Spectroscopy of metals and alloys"*. Academic Press, London-New York, 1972.

J. Hauschild, H. J. Elmers, and U. Gradmann. Phys. Rev. B 57, R677 (1998).

P. Hohenberg and W. Kohn. Phys. Rev. 136, B864 (1964).

J. Izquierdo, D. I. Bazhanov, A. Vega, V. S. Stepanyuk, and W. Hergert. Phys. Rev. B 63, 140413 (2001).

H. J. Jansen. Phys. Rev. B 38, 8022 (1988).

D. D. Johnson. Phys. Rev. B 38, 12807 (1988).

K. Kambe. Z. Naturforschung **22a,** 322 (1967)a.

K. Kambe. Z. Naturforschung **22a,** 422 (1967)b.

K. Kambe. Z. Naturforschung **23a,** 422 (1968).

W. Kohn and L. J. Sham. Phys. Rev. **140,** A1133 (1965).

M. Komelj, C. Ederer, J. W. Davenport, and M. Fähnle. Phys. Rev. B 66, 140407 (2002).

L. D. Landau and E. M. Lifshitz. *"Classical Theory of Fields".* Tankönyvkiadó, Budapest, 1979. In Hungarian

P. Lang, V. S. Stepanyuk, K. Wildberger, R. Zeller, and P. H. Dederichs. Solid State Commun. **92**, 755 (1994).

J. T. Lau, A. Föhlisch, M. Martins, R. Nietubyč, M. Reif. and W. Wurth. New Journal of Physics 4, 98.1 (2002)a.

J. T. Lau, A. Föhlisch, R. Nietubyc, M. Reif, and W. Wurth. Phys. Rev. Lett. 89, 057201 (2002)b.

B. Lazarovits. *"Effects of Orbital Polarization on the Orbital Magnetism and Magnetic Anisotropy in Thin Films".* Diploma Theses, Budapest University of Technology and Economics, 2000.

B. Lazarovits, L. Szunyogh, and P. Weinberger. Phys. Rev. B 65, 104441 (2002).

B. Lazarovits, L. Szunyogh, and P. Weinberger. Phys. Rev. B 67, 024415 (2003).

N. A. Levanov, V. S. Stepanyuk, W. Hergert, D. I. Bazhanov, P. H. Dederichs, A. A. Katsnelson, and C. Massobrio. Phys. Rev. B 61, 2230 (2000).

B. A. Lippmann and J. Schwinger. Phys. Rev. 79, 469 (1950).

A. Lodder and P. J. Braspenning. Phys. Rev. B 49, 10215 (1994).

A. Lodder and J. P. Dekker. Phys. Rev. B 49, 10206 (1994).

F. Löpez-Urias, G. M. Pastor, and K. H. Bennemann. J. Appl. Phys. 87, 4909 (2000).

E. Lundgren, B. Stanka, W. Koprolin, M. Schmid, and P. Varga. Surf. Sci. 423, 357-363 (1999).

A. H. MacDonald, J. M. Daams, S. H. Vosko, and D. D. Koelling. Phys. Rev. B 25, 713 (1982).

J. M. MacLaren, S. Crampin, D. D. Vvedensky, and J. B. Pendry. Phys. Rev. B 40, 12164 (1989).

V. Marsico, M. Blanc, K. Kuhnke, and K. Kern. Phys. Rev. Lett. 78, 94 (1997).

L. Neél. J. Phys. Radium 15, 225 (1954).

B. Nonas, K. Wildberger, R. Zeller, and P. H. Dederichs. Phys. Rev. Lett. 80, 4574 (1998).

B. Nonas, I. Cabria, R. Zeller, P. H. Dederichs, T. Huhne, and H. Ebert. Phys. Rev. Lett. 86, 2146 (2001).

R. Nötzel, N. N. Ledentsov, L. Däweritz, K. Ploog, and M. Hohenstein. Phys. Rev. B 45, 3507 (1992).

P. Ohresser, J. Shen, J. Barthel, M. Zheng, C. V. Mohan, M. Klaua, and J. Kirschner. Phys. Rev. B 59, 3696 (1999).

P. Ohresser, G. Ghiringhelli, 0. Tjernberg, N. B. Brookes, and M. Finazzi. Phys. Rev. B 62, 5803 (2000).

P. Ohresser, N. B. Brookes, S. Padovani, F. Scheurer, and H. Bulou. Phys. Rev. B 64, 104429 (2001).

G. M. Pastor, J. Dorantes-Dävila, and K. H. Bennemann. Phys. Rev. B 40, 7642 (1989).

G. M. Pastor, J. Dorantes-Dävila, S. Pick, and H. Dreyssé. Phys. Rev. Lett. 75, 326 (1995).

L. Petit, S. V. Beiden, W. M. Temmerman, Z. Szotek, G. M. Stocks, and G. A. Gehring. J. Phys.: Condens. Matter 12, 8439 (2000).

B. Piveteau, M. C. Desjonquéres, A. M. Oles, and D. Spanjaard. Phys. Rev. B 53, 9251 (1996).

R. Podloucky, R. Zeller, and P. H. Dederichs. Phys. Rev. B 22, 5777 (1980).

P. Poulopoulos and K. Baberschke. J. Phys.: Condens. Matter **11,** 9495 (1999).

R. Robles, J. Izquierdo, and A. Vega. Phys. Rev. B 61, 6848 (2000).

J. L. Rodriguez-López, F. Aguilera-Granja, A. Vega, and J. A. Alonso. European Physical Journal D 6, 235 (1999).

M. E. Rose. *"Relativistic Electron Theory".* John Wiley & Sons, New York, 1961.

M. P. L. Sancho, J. M. L. Sancho, and J. Rubio. J. Phys. F: Met. Phys. **15,** 851 (1985).

J. Schwitalla, B. L. Gyorffy, and L. Szunyogh. Phys. Rev. B 63, 104423 (2001).

J. Shen, M. Klaua, P. Ohresser, H. Jenniches. J. Barthel, C. V. Mohan, and J. Kirschner. Phys. Rev. B 56, 11134 (1997)a.

J. Shen, R. Skomski, M. Klaua, H. Jenniches, S. S. Manoharan, and J. Kirschner. Phys. Rev. B 56, 2340 (1997)b.

J. Shen, H. Jenniches, C. V. Mohan, J. Barthel, M. Klaua, P. Ohresser, and J. Kirschner. Europhys. Lett. 43, 349 (1998)a.

J. Shen, P. Ohresser, C. V. Mohan, M. Klaua, J. Barthel, and J. Kirschner. Phys. Rev. Lett. 80, 1980 (1998)b.

P. P. Singh. J. Magn. Magn. Mater **261,** 347-352 (2003).

P. Soven. Phys. Rev. **156,** 809 (1967).

D. Spišák and J. Hafner. Phys. Rev. B 65, 235405 (2002).

J. B. Staunton, B. L. Györffy, J. Poulter, and P. Strange. J. Phys. C 21, 1595 (1988).

P. Steiner, S. Hüfner, and W. Zdrojewski. Phys. Rev. B 10, 4704 (1974).

V. S. Stepanyuk, W. Hergert, P. Rennert, K. Wildberger, R. Zeller, and P. H. Dederichs. Phys. Rev. B 54, 14121 (1996)a.

V. S. Stepanyuk, W. Hergert, K. Wildberger, R. Zeller, and P. H. Dederichs. Phys. Rev. B 53, 2121 (1996)b.

V. S. Stepanyuk, W. Hergert, P. Rennert, K. Wildberger, R. Zeller, and P. H. Dederichs. Solid State Commun. **101,** 559 (1997)a.

V. S. Stepanyuk, W. Hergert, P. Rennert, K. Wildberger, R. Zeller, and P. H. Dederichs. J. Magn. Magn. Mater 165, 272 (1997)b.

V. S. Stepanyuk, W. Hergert, P. Rennert, K. Wildberger, R. Zeller, and P. H. Dederichs. Surf. Sci. **377-379,** 495 (1997)c.

V. S. Stepanyuk, W. Hergert, P. Rennert, K. Wildberger, R. Zeller, and P. H. Dederichs. Phys. Rev. B 59, 1681 (1999).

V. S. Stepanyuk and W. Hergert. Phys. Rev. B 62, 7542, (2000).

V. S. Stepanyuk, D. V. Tsivline, D. I. Bazhanov, W. Hergert, and A. A. Katsnelson. Phys. Rev. B 63, 235406 (2001).

J. Stöhr. J. Magn. Magn. Mater. **200** 470 (1999).

J. Stöhr and H. König. Phys. Rev. Lett. 75, 3748 (1995).

P. Strange, J. B. Staunton, and B. L. Györffy. J. Phys. C 17, 3355 (1984).

L. Szunyogh, B. Üjfalussy, P. Weinberger, and J. Kollär. J. Phys.: Condens. Matter 6, 3301 (1994)a.

L. Szunyogh, B. Üjfalussy, P. Weinberger, and J. Kollär. Phys. Rev. B 49, 2721 (1994)b.

L. Szunyogh, B. Ujfalussy, and P. Weinberger. Phys. Rev. B 51, 9552 (1995).

L. Szunyogh and B. L. Györffy. Phys. Rev. Lett. 78, 3765 (1997).

L. Szunyogh, B. Ujfalussy, and P. Weinberger. Phys. Rev. B 55, 14392 (1997).

L. Szunyogh, J. Zabloudil, A. Vernes, P. Weinberger, B. Ujfalussy, and C. Sommers. Phys. Rev. B 63, 184408 (2001).

C. Uiberacker, J. Zabloudil, P. Weinberger, L. Szunyogh, and C. Sommers. Phys. Rev. Lett. 82, 1289 (1999).

B. Ujfalussy, L. Szunyogh, P. Bruno, and P. Weinberger. Phys. Rev. Lett. 77, 1805 (1996)a.

B. Ujfalussy, L. Szunyogh, and P. Weinberger. Phys. Rev. B 54, 9883 (1996)b.

G. van der Laan. Phys. Rev. Lett. 59, 2360 (1987).

G. Vignale and M. Rasolt. Phys. Rev. Lett. 59, 2360 (1987).

G. Vignale and M. Rasolt. Phys. Rev. B 37, 10685 (1988).

J. H. V. Vleck. Phys. Rev. 52, 1178 (1937).

S. H. Vosko, L. Wilk and M. Nusair. Can. J. Phys. 58, 1200 (1980).

D. Wang, R. Wu, and A. J. Freeman. Phys. Rev. B 47, 14932 (1993).

D. S. Wang, R. Wu, and A. J. Freeman. J. Magn. Magn. Mater 129, 237 (1994).

P. Weinberger, R. Dirl, A. M. Boring, A. Gonis, and A. J. Freeman. Phys. Rev. B 37, 1383 (1988).

P. Weinberger. *"Electron Scattering Theory for Ordered and Disordered Matter"*. Clarendon, Oxford, 1990.

P. Weinberger and L. Szunyogh. Comp. Mat. Sci. 17, 414 (2000).

R. Wienke, G. Schütz, and H. Ebert. J. Appl. Phys. 69, 6147 (1991).

K. Wildberger, V. S. Stepanyuk, P. Lang, R. Zeller, and P. H. Dederichs. Phys. Rev. Lett. 75, 509 (1995).

F. Wilhelm, P. Poulopoulos, G. Ceballos, H. Wende, K. B. P. S. D. Benea, H. Ebert, M. Angelakeris, N. K. Flevaris, D. Niarchos, A. Rogalev, and N. B. Brookes. Phys. Rev. Lett. 85, 413 (2000).

S. M. York and F. M. Leibsle. Phys. Rev. B 64, 33411, (2001).

J. Zabloudil. *"The full-potential screened KKR method"*. PhD thesis, Vienna University of Technology, 2000.

R. Zeller, R. Podloucky, and P. H. Dederichs. Z. Phys. B 38, 165 (1980).

R. Zeller, P. H. Dederichs, B. Üjfalussy, L. Szunyogh, and P. Weinberger. Phys. Rev. B 52, 8807 (1995).

L. Zhong, M. Kim, X. Wang, and A. J. Freeman. Phys. Rev. B 53, 9770 (1996).

Publications

Personal data:

Name:	Dipl.-Ing. **Bence Lazarovits**
Address:	Institut für Allgemeine Physik, Technische Universität Wien, Getreidemarkt 9/134, A-1060 Vienna, Austria
Born:	September 16, 1976 in Budapest, Hungary
Nationality:	Hungarian
Marital status:	Unmarried, no children
Languages:	English, German

Papers:

2002:

Magnetic properties of iron adatoms and small iron clusters on Ag(lOO)
B. Lazarovits, L. Szunyogh and P. Weinberger, JMMM, **240** (2002) 331-333

Fully relativistic calculation of magnetic properties of Fe, Co, and Ni adclusters on Ag(lOO)
B. Lazarovits, L. Szunyogh, and P. Weinberger, Phys. Rev. B 57, 7804 (2002)

2003:

Magnetic properties of finite Co chains on Pt(111)
B. Lazarovits, L. Szunyogh, and P. Weinberger, Phys. Rev. B 67, 024415 (2003)

Ab-initio studies of electric transport in terms of the real space Kubo-Greenwood equation
K. Palotäs, B. Lazarovits, P. Weinberger and L. Szunyogh, Phys. Rev. B 67. 174404 (2003)

Magnetic properties of finite Fe chains at fcc Cu(OOl) and Cu(lll) surfaces
B. Lazarovits, L. Szunyogh, P. Weinberger and B. Ujfalussy, submitted to Phys. Rev. B (2003), manuscript number: BB9169

Magnetic properties of finite iron wires on Cu(lll)
B. Lazarovits, L. Szunyogh and P. Weinberger, submitted contribution to International Conference of Magnetism (ICM) (2003)

Electric transport in nanostructures: real space ab-initio investigations
K. Palotäs, B. Lazarovits, P. Weinberger and L. Szunyogh, submitted contribution to ICM (2003)

Ab initio spin-dynamic studies of small metallic particles on surfaces
B. Üjfalussy, G. M. Stocks, L. Szunyogh and B. Lazarovits, submitted contribution to ICM (2003)

Acknowledgments

I would like to acknowledge Prof. Peter Weinberger for his continuous support and guidance during the three years' course of rny work.

I would like to thank Dr. Läszlö Szunyogh for his indispensable guidance and help both in theoretical and technical questions.

I want to thank Dr. Andräs Vernes for sharing his experiences and a room with me.

Thanks to Dr. Baläzs Üjfalussy for the fruitful discussions.

Thanks to members of the CMS for the nice milieu.

I am grateful to the Center of Computational Materials Science for the opportunity to work there.

My work was financially supported by the Austrian Science Foundation (Science College, "Computational Materials Science", Contract No. W004).

Curriculum Vitae

Curriculum Vitae

Personal data

Name:	Bence Lazarovits
Address:	1040 Wien, Schlüsselgasse 11/46.
Born:	September 16, 1976 in Budapest, Hungary
Nationality:	Hungarian
Martial status:	Unmarried, no children
Languages:	Hungarian, English

Education

1983 — 1991	elementary school in Budapest, Hungary
1991 — 1995	grammar-school in Budapest, Hungary

Studies

09/1995 - 06/2000	Engineering Physics at the Faculty of Natural Sciences, Budapest University of Technology and Economics, Budapest, Hungary
12/1999 - 06/2000	diploma thesis: "Effects of Orbital Polarization on the Orbital Magnetism and Magnetic Anisotropy in Thin Films", supervisor: Assist. Prof. Läszlö Szunyogh,

	Institute of Physics, Budapest University of Technology and Economics, Budapest, Hungary
06/2000	diploma degree
09/2000-	doctoral study at Center for Computational Materials Science, FWF-Science College "Computational Materials Scinece", Vienna University of Technology, Vienna, Austria supervisor: Univ.-Prof. Dr. Peter Weinberger

Vienna, 25. Mai 2003